![University of Glasgow logo]

Angelucci, Sara (2025) *Multi-Plane Light Converter based on metasurface and Machine Learning to understand the mode sorter's applications.* PhD thesis

Multi-Plane Light Converter based on metasurface and Machine Learning to understand the mode sorter's applications

by

Sara Angelucci

SUBMITTED IN FULlFILMENT OF THE REQUIREMENTS FOR THE DEGREE
OF DOCTOR OF PHILOSOPHY

James Watt School of Engineering

College of Science and Engineering

May 2024

ABSTRACT

This scientific study delves into the realm of metasurfaces, offering an exhaustive investigation into their underlying principles, practical applications, and the fabrication methods imperative for their realisation. A focal point of this exploration is the detailed exposition of the fabrication process for the Multi-Plane Light Convertor (MPLC) device, supported by captured images validating the precision of each critical step. Initial results indicate the satisfactory functioning of the MPLC, yet further analyses and optimisations are deemed essential to unlock its full potential.

The MPLC device demonstrates versatile applications across telecommunications, energy-related fiber sensing, medical imaging, and biological tomoholography. However, at present, no physical devices based on metasurfaces are available that can fully implement these functions.

In parallel, a novel and robust fibre bend sensor has been developed, showcasing the capability to precisely locate bends through inter-modal coupling. Modal decomposition reduces sensitivity to relative phase, revealing features providing accurate information about the shape or position of bends within the fiber. The simplicity and cost-effectiveness of this approach offer potential applications in wearable technology, motion sensors and aircraft wing shape sensing.

Both experiments revolve around the concept of a mode sorter. The first experiment focuses on creating a novel device not yet available on the market, specifically the Multi-Plane Light Converter (MPLC). The second set of experiments, on the other hand, is centered around the practical application of the mode sorter as an instrumental component. The combination of mode de-multiplexing with machine learning holds promise for powerful applications, particularly in scenarios where constant variations in relative phase can be treated as noise, such as monitoring atmospheric conditions or extracting

information from environments with dense scattering.

Practical deployment considerations include the need for retraining in cases of significant system or fiber type changes. Once fully trained, retraining intervals are typically weeks to months under normal temperature fluctuations, necessitating further research into extreme temperature variations encountered in applications like aviation. The use of multi-core fibers is recommended to enhance sensitivity to multiple directions.

In summary, the study demonstrates the feasibility of utilizing machine learning for accurate millimetric-scale curvature detection by incorporating a mode sorter into the optical setup. While exhibiting robust performance, limitations exist in detecting bends or movements not introducing changes in inter-modal coupling and relative phase shifts. The consistent alignment and outcomes observed in experiments underscore the stability and reliability of the experimental setup, instilling confidence in the algorithm's performance.

DECLARATION

I declare that, except where explicit reference is made to the contribution of oth- ers, that this dissertation is the result of my own work and has not been submitted for any other degree at the University of Glasgow or any other institution.

Contents

List of Tables

List of Figures

Abbreviation

- α-Si: Amorphous Silicon

- AI: Artificial Intelligence

- APC: Automatic Pressure Control

- AR: Augmented Reality

- BIM: Bi-isotropic Metamaterials

- CCD: Charge Coupled Device

- CMOS: Complementary Metal-Oxide-Semiconductor

- CNN: Convolutional Neural Network

- CVD: Chemical Vapor Deposition

- DMD: Digital Micromirror Device

- DNG: Double Negative

- DNN: Deep Neural Networks

- DPS: Double Positive

- DRIE: Deep Reactive Ion Etching

- DWDM: Dense Wavelength-Division Multiplexing

- EBL: Electron Beam Lithography

- EBPG: Electron Beam Pattern Generator

- EBPVD: Electron Beam Physical Vapor Deposition

- EM: Electromagnetic

- ENG: Epsilon Negative

- EUV: Extreme Ultraviolet Lithography

- FBG: Fiber Bragg Grating

- FDTD: Finite-Difference Time-Domain

- FEM: Finite Element Method

- FIB: Focused Ion Beam

- FWHM: Full Width at Half Maximum

- GDSII: Graphic Data System II

- GPF: Grant Agreement Preparation Forms

- HF: Hydrofluoric Acid

- HG: Hermite-Gaussian

- HSQ: Hydrogen Silsesquioxane

- ICP: Inductively Coupled Plasma

- IIoT: Industrial Internet of Things

- IPA: Isopropyl Alcohol

- IPC: Inductively Coupled Plasma

- JWNC: James Watt Nanofabrication Centre

- LCD: Liquid Crystal Display

- LG: Laguerre-Gaussian

- LP: Laguerre-Polynomial

- LSPR: Localized Surface Plasmon Resonances

- MFC: Mass Flow Controller

- MIBK: Methyl Isobutyl Ketone

- MEMs: Micro-electro-mechanical System

- ML: Machine Learning

- MMs: Metamaterials

- MNG: Mu Negative

- MPLC: Multi-Plane Light Converter

- N_2: Nitrogen Gas

- N2: Nitrogen

- NIL: Nanoimprint Lithography

- OAM: Orbital Angular Momentum

- OASIS: Open Artwork System Interchange Standard

- OFSs: Optical Fiber Sensors

- PCA: Principal Component Analysis

- PE: Photoelectric Effect

- PECVD: Plasma-Enhanced Chemical Vapor Deposition

- PICs: Photonic Integrated Circuits

- PPE: Personal Protective Equipment

- PSSA: Polystyrene Sulfonic Acid

- PVD: Physical Vapor Deposition

- RBF: Radial Basis Function

- RCS: Radar Cross-Section

- RF: Radio Frequency

- RIE: Reactive Ion Etching

- SAM: Spin Angular Momentum

- SEM: Scanning Electron Microscope

- SERS: Surface-Enhanced Raman Scattering

- SF_6: Sulfur Hexafluoride

- SHM: Structural Health Monitoring

- SiH_2: Silane

- SLM: Spatial Light Modulator

- SU: Scanning Unit

- SVM: Support Vector Machine

- TMAH: Tetramethylammonium Hydroxide

- UV: Ultraviolet

- VR: Virtual Reality

- WSNs: Wireless Sensor Networks

0

- mTorr: Millitorr

- sccm: Standard Cubic Centimeters per Minute

Chapter 1

General introduction

This section delves into the fundamental concepts underlying metasurfaces and high-lights their potential applications. The term "metamaterial" has two derivation, one Greek "$\mu\varepsilon\tau a'$" that means "beyond" and the other from the Latin "materia" that means "matter/material" [1]. Metasurfaces have emerged as a field of study within the realm of meta-materials, offering unprecedented control over the behaviour of electromagnetic waves. A material that is structured at the subwavelength scale can enable the manipulation of wavefronts with precision, paving the way for a plethora of applications such as optics, photonics, and many more [2]. Unlike phase plates, which are traditional optical elements that control light through spatially varying phase shifts achieved by changes in material thickness or refractive index, metasurfaces offer unprecedented control over light. Phase plates are easier and cheaper to fabricate but are generally less versatile than meta-surfaces. Metasurfaces manipulate light at the nanoscale using engineered meta-atoms, making them highly versatile and capable of achieving multifunctional optical responses. However, they require advanced fabrication techniques. This chapter will provide a general overview of the characteristics and applications of metasurfaces, with detailed discussions of specific projects covered in subsequent chapters of this work.

Generally, the electromagnetic properties of a material are determined by its chemical composition [3]. However, what distinguishes metasurfaces, known as the "metamaterial paradigm," is the ability to control electromagnetic properties by altering not only the chemical composition but also the shape and geometry of the structures that compose them. These properties can be engineered to transmit, reflect, absorb, or deflect electromagnetic waves and are composed of two-dimensional arrays of subwavelength-sized nanostructures [4].

In 1968, a Russian physicist, V. Vaselago hypothesised for the first time the possibility that a material could possess both permittivity and negative permeability [5]. The first researcher to successfully create a material with negative permeability was J. Pendry [6], approximately 60 years after the concept was first proposed. However, the first true metamaterial exhibiting both negative permittivity and negative permeability was developed by D. Smith's research group. This pioneering metamaterial combined Pendry's metallic split-ring resonators with copper wire strips [7]. Considering the above, it is possible to divide the metasurfaces into four categories based on the value of permeability and permittivity. Permeability (μ) is a measure of how a material responds to a magnetic field and indicates the degree to which a material can support the formation of a magnetic field within itself. Permittivity (ϵ) is a measure of how a material responds to an electric field and indicates the ability of a material to polarise in response to an electric field, affecting the propagation of electromagnetic waves through the material. These categories will be visually represented in Fig. 1.1.

- *Double Positive (DPS) material ($\epsilon>0$, $\mu>0$)*: materials that exhibit both permittivity and permeability greater than 0; these materials can be used in standard optical and electromagnetic applications, including lenses, waveguides, and antennas, utilise conventional dielectric materials such as glass and water as examples [3]. Upper right quadrant of the graph (Fig. 1.1).

- ***Double Negative (DNG) material ($\epsilon<0$, $\mu<0$)***: materials that, unlike the double-positive ones, exhibit both permittivity and permeability less than 0; these materials exhibit negative refraction, where the direction of energy flow (Poynting vector) is opposite to the direction of wave propagation, allowing for applications such as superlenses that can overcome the diffraction limit, cloaking devices, and advanced optical components, with examples including metamaterials designed with split-ring resonators and metallic wires [7]. Lower left quadrant of the graph (Fig. 1.1).

- ***Epsilon Negative (ENG) material ($\epsilon<0$, $\mu>0$)***: materials that have permittivity less than zero and permeability greater than zero. These materials support surface plasmon polaritons and can confine electromagnetic waves to subwavelength dimensions, enabling applications in plasmonic devices, sensors, and enhancing the efficiency of solar cells, with examples including metals at optical frequencies such as silver and gold [6]. Upper left quadrant of the graph (Fig. 1.1).

- ***Mu Negative (MNG) material ($\epsilon>0$, $\mu<0$)***: material that are opposite to the ENG, they have permittivity greater than zero and permeability less than zero; these materials can support magneto-inductive waves and exhibit unique magnetic responses to electromagnetic fields, enabling applications in magnetic sensors and antennas, with examples including metamaterials with magnetic inclusions [8]. Lower right quadrant of the graph (Fig. 1.1).
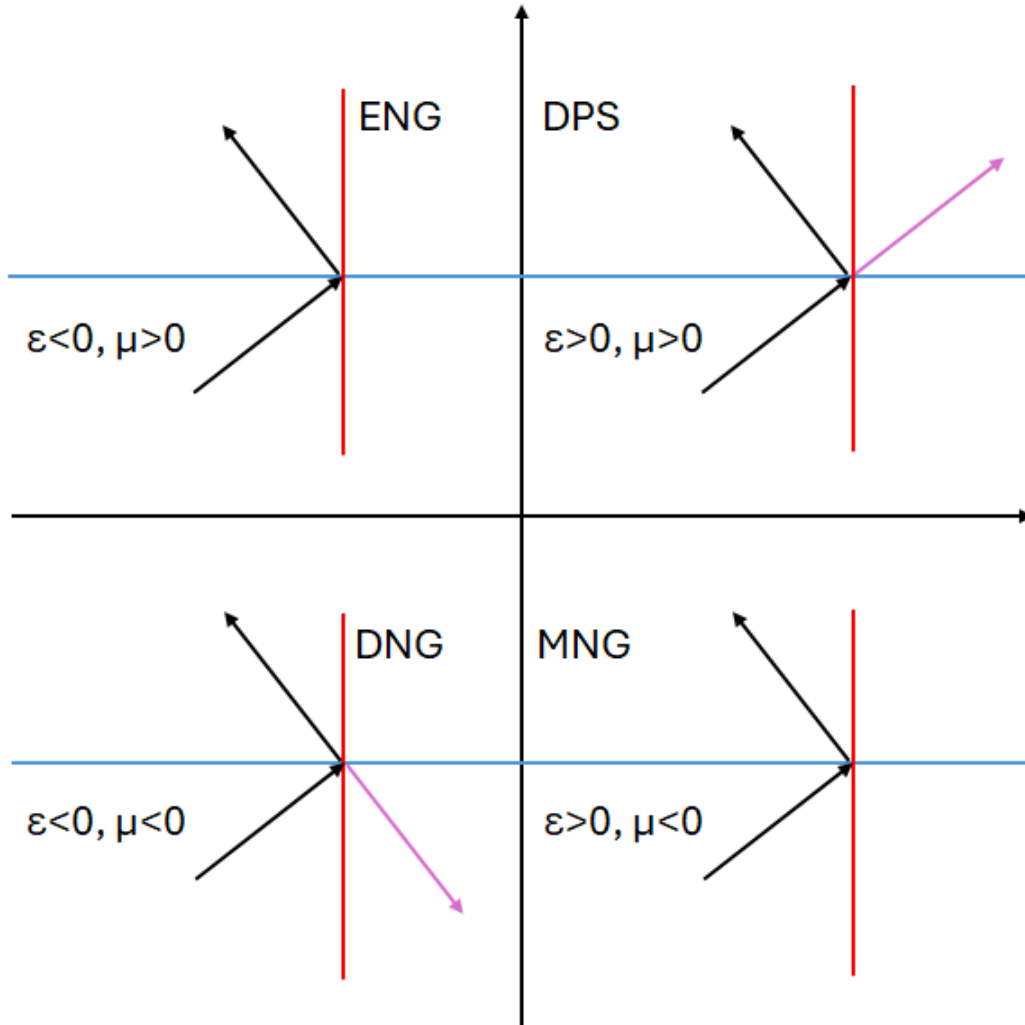
Figure 1.1: Schematic representation of the classification of metasurfaces based on the values of permeability and permittivity. The blue lines represent air while the red lines indicate the medium. Adapted from [9].

The figure presents a schematic representation of the division explained on a Cartesian basis. In the four quadrants, the horizontal blue lines represent air, while the vertical red lines represent the medium. The top-left quadrant depicts the behaviour of electromagnetic waves when the value of epsilon is negative (ENG), the bottom-left quadrant depicts the behaviour when both values are negative (DNG), the top-right quadrant illustrates the behaviour when both values are positive, while the bottom-right quadrant shows the behaviour when mu is negative.

To further elaborate on permeability and permittivity in the field of metasurfaces, we can consider their complex values. Complex-valued permittivity means that a material's response to an electric field includes both a real and an imaginary component. The real part of permittivity (ϵ') indicates the material's ability to store electrical energy, while the imaginary part (ϵ") accounts for energy loss due to polarisation effects. This concept was notably demonstrated by Landy et al. in their pioneering work on metamaterial perfect absorbers in the microwave region [10]. Similarly, complex-valued permeability implies that a material's reaction to a magnetic field also has both a real and an imaginary component. The real part of permeability (μ') shows the material's capacity to support magnetic fields, whereas the imaginary part (μ") represents energy dissipation due to magnetic effects.

Understanding complex-valued permittivity and permeability is essential for comprehending how materials behave with varying frequencies of electromagnetic waves. These properties are vital in designing and engineering materials for various applications, including perfect absorbers. Recent research has focused on precisely tuning these parameters to achieve desired electromagnetic characteristics. For instance, Ye et al. demonstrated a metamaterial perfect absorber with frequency-independent dispersion regions of permittivity and permeability, achieving ultrawideband absorption [11]. Similarly, Long et al. theoretically deduced the critical coupling conditions for perfect absorption in thin-film absorbers by analysing these complex-valued constitutive parameters [12]. Classifying metamaterials as double negative, single negative, or double positive suggests that these materials have distinct electric and magnetic responses characterised by their permittivity (ϵ) and permeability (μ). Nonetheless, often the electric field can induce magnetic polarisation and the magnetic field can induce electric polarisation. This phenomenon is referred to as magnetoelectric coupling. Metamaterials exhibiting these properties are called bi-isotropic [13]. Beyond this initial classification system, metasurfaces can also

be categorised based on their structure, functionality, and the physical phenomena they exhibit. These classifications will be explained in the following subsections, providing a more comprehensive overview of the world of metasurfaces.

1.1   Metasurfaces classification

As mentioned before the metasurfaces can be classified based on their structural design, functionality, and the physical phenomena they exploit.

1.1.1   Structural

In this first group, the classification is based on the arrangement of structures within the metasurface; the image in Fig. 1.2 supports the visualisation of how metasurfaces are divided according to this classification.

- **Periodic metasurfaces**: these metasurfaces are characterised by their regularly arranged meta-atoms in a repeating pattern, exert an influence on the interaction with electromagnetic (EM) waves, resulting in predictable and tunable EM responses; these structures have been extensively explored for various applications, including the development of high-efficiency diffractive optical elements [14]. At the heart of periodic metasurfaces are the meta-atoms, serving as the fundamental building blocks. These units can be metallic or dielectric structures meticulously designed to interact with electromagnetic waves. Their subwavelength scale enables precise control over the wavefront, facilitating functionalities such as beam steering and focusing. Meta-atoms exhibit geometric variability, allowing for diverse shapes and configurations, such as split-ring resonators, nanorods, or dielectric nanoparticles, tailored to specific functionalities. The periodicity of these metasurfaces is

characterised by the regular arrangement of meta-atoms, crucial for achieving desired electromagnetic responses. The spatial period, defined by the distance between neighbouring meta-atoms, governs the interaction of the metasurface with incident waves. In terms of electromagnetic response, periodic metasurfaces excel in wave manipulation. Through phase control, achieved by adjusting the size, shape, and orientation of meta-atoms, these surfaces can steer beams, focus waves, and shape wavefronts [15]. Additionally, they allow for amplitude modulation, enabling functionalities like polarisation conversion and absorptive behaviour. The periodic arrangement of meta-atoms induces diffraction phenomena and interference patterns, shaping the overall electromagnetic response [16]. These effects, coupled with the predictable response due to periodicity, offer precise control over the electromagnetic behaviour of the metasurface. Applications of periodic metasurfaces span across beam steering devices, focusing and imaging systems, and polarisation control elements. Their predictable diffraction and interference effects, combined with subwavelength control over the wavefront, make them indispensable in optics and photonics [17] (Fig. 1.2 a).

- ***Aperiodic metasurfaces***: represent a departure from traditional periodic metasurfaces, featuring irregular distributions of meta-atoms that enable intricate and versatile manipulation of electromagnetic waves [18]. Unlike their periodic counterparts, aperiodic metasurfaces lack repetitive arrangements, allowing for nuanced control over light-matter interactions [19]. One notable advantage of aperiodic metasurfaces lies in their ability to scatter incident waves diffusely, a phenomenon of significance in various applications such as disordered photonics, random lasers, and diffuse imaging. Yoon demonstrated this diffuse scattering behaviour through the use of disordered metasurfaces, showcasing the efficacy of aperiodic designs in disordered photonics contexts [20]. Moreover, aperiodic metasurfaces inherently possess

broadband characteristics, operating effectively across a wide frequency spectrum without requiring precise tuning for specific resonance frequencies. This broadband capability renders them versatile and suitable for applications requiring broad frequency coverage, including broadband optical devices. In contrast to periodic structures, which often exhibit resonance behaviour limited to specific frequencies, aperiodic designs offer extended functionality across diverse frequency bands. The irregular spatial distribution of meta-atoms in aperiodic metasurfaces also confers multifunctionality, enabling the realisation of diverse functionalities beyond wave scattering. By strategically manipulating the spatial arrangement of meta-atoms, aperiodic structures can achieve a multitude of functionalities, paving the way for the development of innovative optical devices with enhanced performance and capabilities [21] (Fig. 1.2 b).

- ***Graded metasurfaces***: this represent a class of engineered electromagnetic structures characterised by spatially varying properties that afford precise control over the propagation of electromagnetic waves. Unlike their periodic and aperiodic counterparts, graded metasurfaces exhibit continuous changes in their electromagnetic parameters across their surfaces, facilitating tailored functionalities across diverse applications. By introducing gradients in parameters such as phase, amplitude, and polarisation, these metasurfaces enable sophisticated wavefront engineering, leading to versatile functionalities across different frequency bands and applications. One of the fundamental characteristics of graded metasurfaces is their continuous variation in electromagnetic parameters, achieved through the design of meta-atoms or meta-structures. This gradual variation permits seamless integration of functionalities across the metasurface, allowing for smooth transitions in wavefront manipulation. Graded metasurfaces have garnered considerable attention in various fields, including imaging, sensing, communication, and beam shaping, owing to their unique

capabilities. For instance, Yu et al. demonstrated the application of graded metasurfaces for aberration correction in imaging systems, showcasing their potential in enhancing imaging resolution and quality [15]. Moreover, graded metasurfaces offer avenues for novel functionalities such as anomalous refraction, metasurface lenses, and holography. Through judicious design of spatial gradients in the metasurface structure, researchers have attained unprecedented control over the propagation of light, enabling the realisation of advanced optical devices and systems. The versatility and precision afforded by graded metasurfaces hold promise for revolutionising various technological domains, from optical communications to biomedical imaging. With ongoing advancements in design methodologies and fabrication techniques, graded metasurfaces are poised to play an increasingly significant role in shaping the future of electromagnetic wave manipulation and optical device engineering (Fig. 1.2 c).
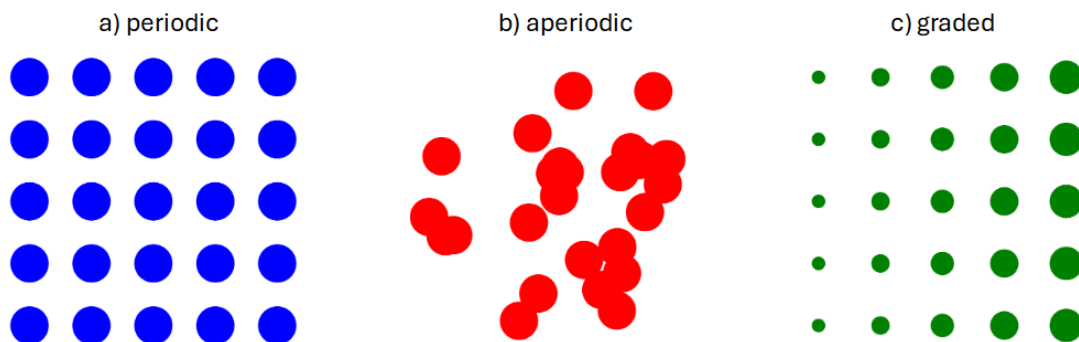
Figure 1.2: Schematic representation of different types of metasurfaces based on structural classification: a) Periodic metasurface: regularly arranged structures (blue circles) in a repeating pattern with consistent intervals. b) Aperiodic metasurface: irregular or random arrangement of structures (red circles) without a repeating pattern. c) Graded metasurface: structures that gradually change in size (green circles) across the surface, creating a gradient effect.

In summary, periodic metasurfaces provide predictable and tunable electromagnetic responses, while aperiodic metasurfaces embrace complexity and randomness, offering

opportunities for diffuse light scattering and broadband functionalities. Graded metasurfaces introduce spatially varying properties, enabling sophisticated wavefront engineering across diverse frequency bands. Each type has its pros and cons: periodic metasurfaces are easier to design but may be limited in functionality; aperiodic metasurfaces offer design flexibility but can be challenging to control precisely; graded metasurfaces provide seamless integration of functionalities but require complex design and fabrication processes.

For the work carried out in this thesis, the fabricated metasurface falls into the last category as it presents different patterns (nanopillars) that have different diameters within the metasurface (for further details on the fabrication of the device refer to chapters 3 and 4).

1.1.2   Functional

Metasurfaces can also be categorised based on their function, which includes reflective, transmissive, or absorptive types. Their shared characteristic lies in their capacity to manipulate the phase, amplitude, and polarisation of electromagnetic waves based on how the electromagnetic wave interacts with the surface.

- *Reflective metasurfaces*: are engineered to control the reflection properties of electromagnetic waves incident upon them. They allow for functionalities such as beam steering, focusing, and wavefront shaping. Reflective metasurfaces find applications in various fields, including phased array antennas for beamforming, holography for spatial light modulation, and imaging systems for aberration correction [22].

- *Transmissive metasurfaces*: are designed to control the transmission properties of electromagnetic waves passing through them. They enable functionalities such as anomalous refraction, lensing, spectral filtering, and polarisation control

in transmitted light. Transmissive metasurfaces are used in imaging systems for creating compact lenses, in communication systems for polarisation control, and in spectroscopy for spectral filtering [23].

- ***Absorptive metasurfaces***: are designed to efficiently absorb electromagnetic waves within specific frequency ranges. They minimise reflection and transmission by selectively absorbing certain frequencies while reflecting or transmitting others. Absorptive metasurfaces find applications in stealth technology for reducing radar cross-sections, in energy harvesting for capturing and converting electromagnetic energy, in thermal management for controlling heat transfer, and in sensing for detecting specific frequencies or wavelengths [24].

1.1.3 Physical phenomena

- ***Phase gradient metasurface***: is an advanced optical device designed to manipulate the phase of electromagnetic waves across its surface in a spatially varying manner. This spatial modulation of the phase enables the control of wavefronts with precision, leading to a variety of novel optical phenomena and applications. The basic building blocks of a phase gradient metasurface are sub-wavelength-sized elements known as meta-atoms. These meta-atoms can be fabricated from various materials, such as metals, dielectrics, or semiconductors, and are often arranged in a periodic or quasi-periodic fashion. Each meta-atom is designed to impart a specific phase shift to the incident light. By carefully designing the arrangement and properties of these meta-atoms, a continuous phase gradient can be achieved across the metasurface. The phase modulation in phase gradient metasurfaces is typically achieved through resonant scattering, where the dimensions and material properties of the meta-atoms are engineered to produce a desired phase shift.

For instance, Arbabi et al. [24] demonstrated that by using arrays of nanoantennas with varying geometrical parameters, one can achieve precise control over the phase of transmitted or reflected light. One of the primary applications of phase gradient metasurfaces is in beam steering, where the direction of the incident light beam is altered without mechanical movement. This is particularly useful in optical communications and LIDAR systems. For example, Liu et al. [25] showed how a metasurface could deflect an incident beam at a specified angle by imparting a linear phase gradient across the surface . Another significant application is in holography, where phase gradient metasurfaces can create complex wavefronts to reconstruct three-dimensional images. Ni et al. demonstrated holograms with high efficiency and resolution using metasurfaces that provided continuous phase modulation [26]. Additionally, these metasurfaces can function as ultra-thin lenses (metalenses) by focusing light through spatially varying phase delays. Aieta et al. developed a flat lens that could focus light with high efficiency, offering a compact alternative to conventional bulky lenses [27]. Designing phase gradient metasurfaces involves numerical simulations and optimisation techniques to tailor the phase response of each meta-atom. Electromagnetic simulation software, such as finite-difference time-domain (FDTD) or finite element method (FEM) tools, are commonly used to model the interaction of light with the meta-atoms. These simulations help in predicting the phase and amplitude of the transmitted or reflected light. Moreover, advanced fabrication techniques, such as electron beam lithography, focused ion beam milling, and nanoimprint lithography, are employed to create the intricate patterns required for the meta-atoms with the desired phase responses. One of the critical challenges in the development of phase gradient metasurfaces is maintaining high efficiency and broad operational bandwidth. Inefficiencies can arise from material absorption, scattering losses, and imperfect phase modulation. Researchers like Khorasaninejad

et al. have worked on optimising the meta-atom designs and using low-loss materials to enhance the efficiency of these metasurfaces across a wide spectral range [14]. Recent advances in the field have focused on dynamic control of phase gradients, enabling tunable and reconfigurable metasurfaces. For instance, incorporating materials with tunable refractive indices, such as liquid crystals or phase-change materials, allows for real-time control over the phase gradient, paving the way for applications in adaptive optics and dynamic beam shaping.

- ***Huygen's metasurfaces***: is a type of engineered surface designed to control electromagnetic waves with high precision by utilising the principles of Huygens' principle. This principle states that every point on a wavefront can be considered a source of secondary spherical wavelets, and the secondary wavelets emanating from these points can constructively and destructively interfere to form a new wavefront. By carefully engineering the response of each point on the metasurface, Huygens' metasurfaces can manipulate the amplitude, phase, and polarisation of electromagnetic waves to achieve desired wavefronts. The fundamental elements of Huygens' metasurfaces are sub-wavelength-sized scatterers that are arranged in a precise manner to create the required electromagnetic response. These scatterers typically consist of dielectric or metallic resonators that are designed to have specific electric and magnetic dipole responses. By balancing these dipole responses, the metasurface can achieve nearly arbitrary control over the wavefront of transmitted or reflected light. A key feature of Huygens' metasurfaces is their ability to achieve full 2π phase control while maintaining high efficiency. This is typically accomplished by designing the scatterers to exhibit both electric and magnetic dipole resonances at the same frequency. For instance, Decker demonstrated that using dielectric scatterers with high refractive indices allows for strong electric and magnetic resonances,

enabling complete phase control with minimal losses. Their study showed that Huygens' metasurfaces could be fabricated using silicon nanoresonators, which provide the necessary dual-resonance behaviour for efficient phase modulation [28]. One of the notable applications of Huygens' metasurfaces is in the design of ultra-thin lenses, known as metalenses, which can focus light similarly to traditional lenses but with a significantly reduced thickness. Khorasaninejad developed metalenses using titanium dioxide (TiO2) nanofins arranged on a glass substrate, achieving high numerical apertures and efficient focusing across visible wavelengths. These metalenses leverage the full phase control offered by Huygens' metasurfaces to correct aberrations and achieve diffraction-limited focusing [14]. Another important application is in the creation of beam shaping devices, which can tailor the shape of an optical beam for various purposes, such as improving the performance of optical communication systems or enhancing the precision of laser machining. Arbabi et al. designed Huygens' metasurfaces that could convert Gaussian beams into arbitrary shapes, such as vortex beams with orbital angular momentum. Their work demonstrated that these metasurfaces could achieve high conversion efficiency and precise control over the beam profile [24]. Huygens' metasurfaces also find applications in holography, where they can generate complex holographic images with high resolution and efficiency. Ni et al. (2013) created metasurface holograms using arrays of plasmonic nanoantennas, which provided the necessary phase shifts to reconstruct three-dimensional images. This approach allows for compact and versatile holographic devices that can be integrated into various optical systems [26]. The design and optimisation of Huygens' metasurfaces involve sophisticated electromagnetic simulations to predict the behaviour of individual scatterers and their collective response. Tools like finite-difference time-domain (FDTD) and finite element method (FEM) simulations are commonly used to model the interactions

between light and the metasurface. These simulations help in determining the optimal geometry and material properties of the scatterers to achieve the desired phase and amplitude control. Fabrication techniques for Huygens' metasurfaces include electron beam lithography, which allows for the precise patterning of nanoscale features, and atomic layer deposition, which can be used to coat the scatterers with high-refractive-index materials. These advanced fabrication methods are crucial for achieving the fine structural details required for effective metasurface performance.

- ***Plasmonic metasurfaces***: are able to to manipulate electromagnetic waves at subwavelength scales by exploiting surface plasmon resonances. These resonances occur when free electrons in a metal oscillate in response to an incident electromagnetic field, leading to strong light confinement and enhancement at the metal-dielectric interface. By carefully designing the arrangement and properties of nanostructured metallic elements, plasmonic metasurfaces can achieve precise control over the amplitude, phase, and polarisation of light. The fundamental elements of a plasmonic metasurface are metallic nanostructures, such as nanorods, nanodisks, or nanoantennas, which can support localised surface plasmon resonances. The resonant frequency and the electromagnetic response of these nanostructures are highly sensitive to their geometry, size, and the surrounding dielectric environment. This sensitivity allows for the design of metasurfaces with tailored optical properties. For instance, Yu demonstrated that by arranging V-shaped plasmonic nanoantennas in specific patterns, they could create a metasurface capable of imposing spatially varying phase shifts on the transmitted light, achieving beam steering and anomalous reflection [23]. One of the key applications of plasmonic metasurfaces is in the creation of ultrathin lenses, or metalenses, which use subwavelength plasmonic elements to focus light. Aieta showed that by designing plasmonic metasurfaces

with concentric rings of nanoantennas, they could achieve diffraction-limited focusing. These metalenses offer a significant reduction in thickness compared to traditional lenses while maintaining high focusing efficiency [27]. Additionally, plasmonic metasurfaces can be used for imaging systems that require compact and lightweight components, making them suitable for integration into portable and wearable devices. Plasmonic metasurfaces also find applications in holography, where they can generate complex wavefronts to reconstruct three-dimensional images. Ni created holograms using metasurfaces composed of plasmonic nanoantennas, achieving high-resolution and high-efficiency holographic projections. The ability to encode phase information at the nanoscale enables the creation of detailed and dynamic holographic images, which can be applied in display technologies and data storage [26]. Another important application of plasmonic metasurfaces is in the manipulation of light polarisation. By designing asymmetrical nanostructures, such as split-ring resonators or chiral nanoantennas, plasmonic metasurfaces can convert linearly polarised light into circularly polarised light or vice versa. This capability is crucial for advanced imaging techniques and communication systems that rely on specific polarisation states. For example, Poulikakos demonstrated a plasmonic metasurface that could convert incident linearly polarised light into circularly polarised light with high efficiency, highlighting its potential for polarisation control in optical devices [29]. Fabrication techniques for plasmonic metasurfaces include electron beam lithography and focused ion beam milling, which allow for the precise patterning of metallic nanostructures with subwavelength resolution. These techniques are crucial for achieving the intricate designs required for effective plasmonic resonances and the overall performance of the metasurface.

1.2 Metasurface's application

When discussing the various existing types of MMs, they can be divided into six main groups by application, as represented in Fig. 1.3:
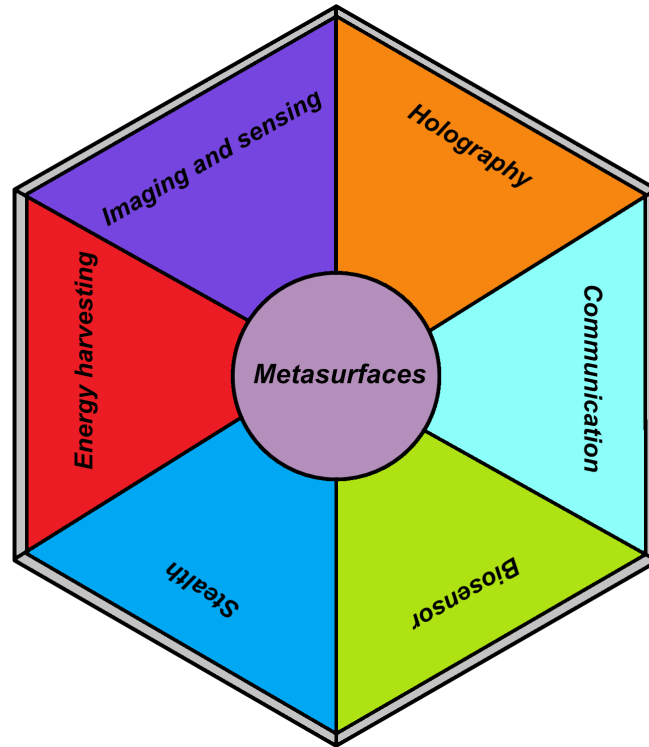
Figure 1.3: Major application of metasurfaces currently under development

Metasurfaces for ***stealth applications*** represent a cutting-edge approach in the field of electromagnetic wave manipulation, specifically designed to reduce the radar cross-section (RCS) of objects, rendering them less detectable by radar systems. These metasurfaces are engineered to manipulate electromagnetic waves to control the phase, amplitude, and polarisation of incident electromagnetic waves effectively cloaking an object from detection. The primary approach to achieving stealth through metasurfaces involves designing these structures to manipulate the surface impedance, matching it to that of free space. This minimises reflections and scattering from the surface. By employing resonant elements like split-ring resonators, patches, or other subwavelength scatterers arranged

in precise patterns, metasurfaces can create destructive interference with incident radar waves. This destructive interference significantly reduces the RCS, as shown by Cui, who demonstrated broadband metasurface absorbers that effectively suppress radar signals [30]. One of the key mechanisms by which metasurfaces enhance stealth is through the absorption of incident radar waves. By designing the metasurface to exhibit high electromagnetic absorption across a wide range of frequencies, it can significantly reduce the reflected signal. For instance, Landy demonstrated a perfect metamaterial absorber that could achieve near-unity absorption by utilising electric and magnetic resonators that matched the impedance of free space, thereby minimising reflection and maximising absorption. This principle has been extended to metasurfaces, where thin layers of engineered materials can absorb incident waves effectively [10]. Phase manipulation is another critical technique for stealth metasurfaces, wherein the reflected waves are engineered to destructively interfere, thereby cancelling out the reflected signal. For example, Cui developed a tunable metasurface absorber using graphene, which could adjust its absorption characteristics in response to external stimuli like electrical or optical signals. This allows the metasurface to adapt to different frequencies and polarisation states of incident radar waves, enabling dynamic control over its stealth properties [30]. Scattering suppression is also a vital method utilised by metasurfaces to reduce RCS. This involves designing the surface to scatter incident waves in multiple directions rather than reflecting them back towards the radar source. A study by Wan demonstrated a metasurface that achieved broadband RCS reduction by using a combination of resonant and non-resonant scatterers. These scatterers were arranged to create multiple scattering pathways, diffusing the reflected signal and reducing its strength in any single direction [31]. Fabrication of metasurfaces for stealth applications requires advanced lithography techniques to achieve the necessary subwavelength precision. Electron beam lithography, nanoimprint lithography,

and photolithography are commonly used to pattern the resonant elements on the meta-surface. These techniques allow for precise control over the size, shape, and placement of each resonant element. Additionally, materials such as metal-dielectric composites are often deposited using chemical vapour deposition (CVD) or physical vapour deposition (PVD), ensuring the high fidelity and uniformity of the metasurface structures over large areas [32]. The physics behind the functioning of metasurfaces for stealth applications is grounded in the principles of electromagnetic wave manipulation. When designed with the appropriate surface impedance, metasurfaces can absorb incoming radar waves rather than reflecting them, converting the electromagnetic energy into heat or reradiating it in non-detectable directions. This absorption is facilitated by the excitation of localised sur-face plasmons or other resonant modes within the metasurface elements. These resonant modes enhance the interaction between the incident waves and the metasurface, leading to efficient energy dissipation and reduced RCS. For instance, a typical metasurface for stealth applications might consist of a periodic array of metallic patches or split-ring res-onators on a dielectric substrate. These elements are engineered to resonate at specific frequencies, creating a tailored electromagnetic response that spans a wide range of in-cident angles. Such designs can be optimised to achieve broadband stealth capabilities, effectively reducing RCS over multiple frequency bands. Advanced metasurface designs often incorporate reconfigurability and tunability, providing dynamic control over the electromagnetic response. This capability is essential for adaptive stealth technologies, where stealth properties can be modified in real-time to counter various radar systems. A notable example of such technology is found in the work of Yu, who demonstrated a meta-surface that could dynamically alter its phase gradient properties to steer reflected radar waves away from the radar source, effectively reducing detectability [15]. The benefits of using metasurfaces for stealth applications include their ability to achieve significant RCS reduction over a broad range of frequencies and incident angles, their compatibility

with various platforms due to their thin and lightweight nature, and the potential for integration with existing materials and structures. However, challenges remain, such as the complexity of fabricating large-area metasurfaces with consistent performance, the need for high-precision manufacturing techniques, and the potential for reduced effectiveness under varying environmental conditions.
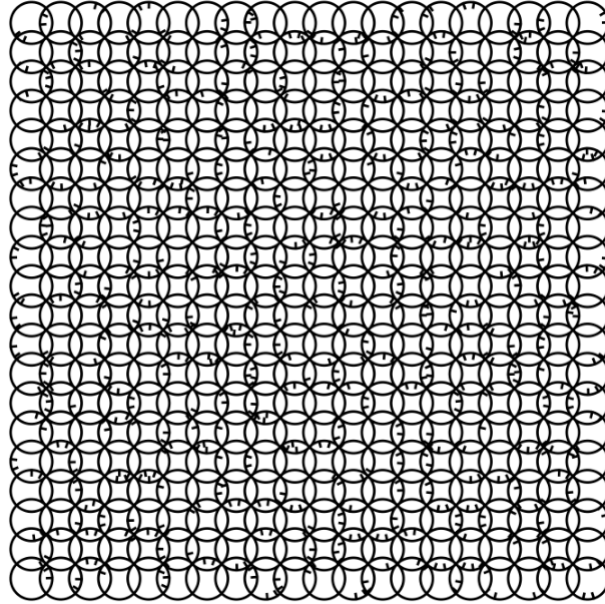
Figure 1.4: Conceptual design of a metasurface for stealth applications, composed of an array of subwavelength resonant elements, specifically split-ring resonators, arranged in a periodic pattern; adapted from [32].

Metasurfaces for ***energy harvesting*** have garnered significant attention due to their ability to efficiently capture and convert various forms of ambient energy into usable electrical power. These advanced materials are particularly effective in electromagnetic wave harvesting, where they interact with radio frequency (RF) signals, microwaves [33], and infrared radiation to optimise energy absorption and conversion [34]. In electromagnetic wave harvesting, metasurfaces are designed to resonate with incident electromagnetic fields. These resonant elements are typically composed of structures like split-ring resonators or metallic patches, which are meticulously engineered to absorb energy at specific

frequencies. When electromagnetic waves encounter these metasurfaces, the resonant elements oscillate, capturing the energy. This energy is then converted into electrical power through rectifying circuits [34][9]. A rectifying antenna, or rectenna, is a crucial component in this process. It combines an antenna, which captures electromagnetic waves, with a rectifier that converts alternating current (AC) signals into direct current (DC). This conversion is essential because most electronic devices and storage systems require DC power. The rectenna operates by using the antenna to receive electromagnetic waves, which are then fed into the rectifier. The rectifier, typically comprising diodes, converts the high-frequency AC signal into a low-frequency DC signal. This setup enables the efficient transfer of captured energy into a usable form. For instance, Huang et al. demonstrated an efficient rectenna system that leverages a metasurface to enhance microwave energy harvesting, achieving significant improvements in power conversion efficiency [35]. For solar energy harvesting, metasurfaces are designed to improve the absorption of sunlight across a broad spectrum, thus enhancing the efficiency of photovoltaic (PV) cells. These metasurfaces often incorporate plasmonic nanostructures that interact strongly with light, increasing absorption. When sunlight hits the metasurface, it generates electron-hole pairs in the photovoltaic material. These pairs are then separated and collected as electrical current. Atwater and Polman highlighted the use of plasmonic metasurfaces integrated with thin-film solar cells, demonstrating substantial improvements in light absorption and photocurrent generation [36]. An example of an advanced energy harvesting metasurface involves capturing infrared radiation and converting it into electrical energy. This metasurface consists of resonant metallic nanostructures designed to absorb infrared light, converting it into heat. The heat is then transferred to a thermoelectric material, which generates electricity. In 2018 a research group showcased a high-efficiency metasurface capable of absorbing mid-infrared radiation and converting it to electrical power using a thermoelectric generator, presenting a novel method to harvest energy from low-light

environments [37].
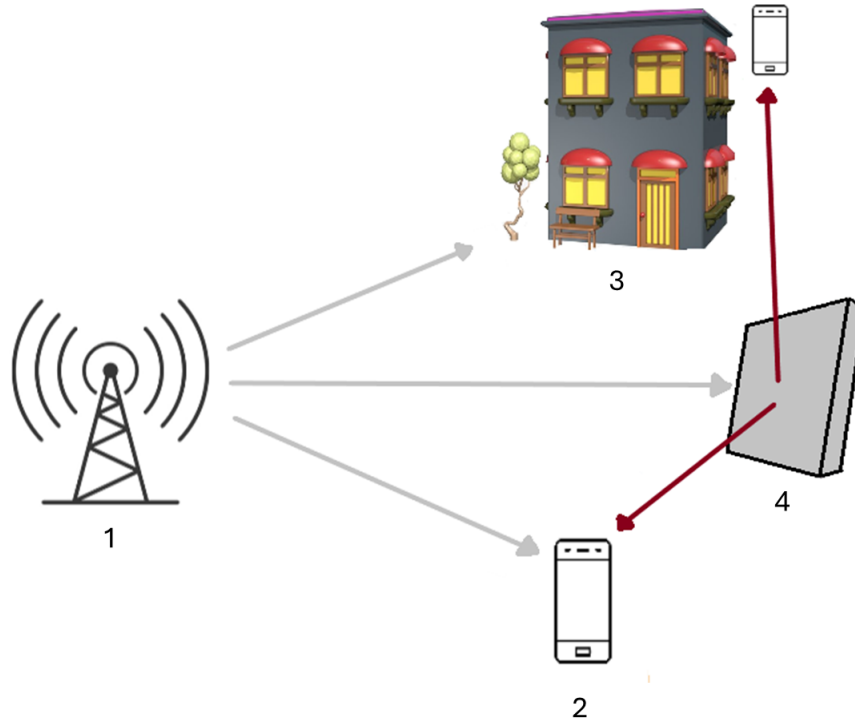
Figure 1.5: Illustration of a metasurface designed for energy harvesting in present of an obstacle. 1) source that transmits electromagnetic energy; 2) high path loss link, an alternative path with high energy loss due to distance or obstacles; 3) a physical barrier blocking the direct energy path; 4) metasurface; the red lines represent how the intelligent metasurface is used to reflect and direct energy around the obstacle. Adapt from [38]

Regarding the **holography application** the metasurfaces can be used to create intricate interference patterns capable of encoding multiple images or information layers. For example, silicon nitride metasurface holograms can produce high-efficiency holograms that display different images based on the viewing angle, as demonstrated by Zheng's research group [39]. Such capabilities are pivotal for applications in data storage, security features, and advanced display technologies. In the domain of data storage, a single holographic element engineered with metasurfaces can store substantial amounts of information. This information can be accessed or decoded by varying the angle of illumination or observation, thereby significantly increasing data density and enhancing security. For instance,

optical discs utilising metasurface technology can reveal different data layers depending on the angle of incident light, leading to a multifold increase in storage capacity compared to traditional methods.

In ***sensing applications***, metasurfaces substantially enhance sensor performance by improving sensitivity and specificity through nanoscale light manipulation. Particularly in the infrared and terahertz spectral regions, metasurfaces considerably boost sensor capabilities. By meticulously designing the resonant properties of these surfaces, sensors achieve superior spectral selectivity and higher signal-to-noise ratios, which are critical for applications such as security screening and non-destructive testing.

A prominent example is the use of graphene-based metasurfaces to augment terahertz wave detection. Terahertz waves, situated between the microwave and infrared regions of the electromagnetic spectrum, are especially beneficial for imaging and sensing applications due to their ability to penetrate numerous non-metallic materials and provide high-resolution images. The enhancement of terahertz detection via metasurfaces is crucial for developing advanced sensors with heightened detection capabilities, as explored in 2013 [40]. These sensors are capable of detecting minute variations in material properties, which is invaluable in security applications, such as identifying concealed weapons or explosives. For example, in an airport security context, a terahertz metasurface sensor could swiftly and accurately identify hidden threats on passengers, thereby improving both safety and efficiency. Additionally, in industrial applications such as quality control in manufacturing, these sensors can inspect materials for defects or inconsistencies, ensuring higher product standards and minimising waste.

The application of metasurfaces in ***wireless communication*** has significantly enhanced various aspects of the technology, including antenna performance, signal propagation, and system efficiency.

These advanced structures enable the design of highly efficient, compact, and reconfigurable antennas. Unlike traditional designs constrained by physical size and shape, metasurfaces can create antennas with enhanced properties. They dynamically adapt their radiation patterns, frequencies, and polarisations to suit different communication needs. Beam steering is achieved electronically without mechanical movement, which is particularly advantageous in mobile communication and satellite systems. In 5G networks, for example, metasurfaces can direct signals to users more efficiently, reducing interference and improving bandwidth utilisation [15]. Utilising subwavelength elements, metasurfaces allow for the miniaturisation of antennas while maintaining or even improving performance. This is particularly beneficial for portable and wearable devices where space and weight are critical considerations [41]. These structures can manipulate electromagnetic waves in ways traditional materials cannot, such as altering the phase, amplitude, and polarisation of waves. This capability is used to enhance signal propagation in complex environments. By imparting specific phase shifts to incoming waves, it is possible to control the direction and focus of the outgoing waves, creating highly directive antennas essential for high-frequency radar and communication systems [41]. Additionally, metasurfaces can be engineered to act as frequency selective surfaces (FSS), allowing certain frequencies to pass while reflecting others. This property creates filters that improve signal quality and reduce noise in communication systems. An example includes integrating an FSS into a system to block unwanted signals and prevent interference [24]. The overall efficiency of communication systems is improved by optimising signal paths and reducing losses. Wireless power transfer systems benefit from focusing and directing electromagnetic energy to specific locations, which is useful for powering remote sensors and IoT devices where traditional power delivery methods are impractical [42]. The reconfigurability of these surfaces, achieved through tunable materials or integrating active

components like varactors and diodes, allows for real-time adjustment of their electromagnetic properties. This adaptability is crucial for modern communication systems that require flexibility to handle varying operational conditions and user demands [30].

Metasurfaces can be designed to support localised surface plasmon resonances (LSPR) which occur when conduction electrons on the surface of metallic nanostructures oscillate in response to an incident electromagnetic field; LSPR leads to strong electromagnetic field enhancements near the surface significantly increasing the sensitivity of biosensors This heightened sensitivity allows for the detection of low concentrations of biomolecules through changes in the refractive index or spectral shifts of the resonance peaks [43]. By engineering metasurfaces to support plasmonic hotspots, where the electromagnetic field is intensely localised, surface-enhanced Raman scattering (SERS) can be enhanced. These hotspots amplify the Raman signals of molecules adsorbed on the surface, enabling the detection of single molecules and providing rich molecular fingerprint information crucial for biosensing applications [39]. Metasurface-based biosensors have shown great potential in the early detection of diseases by identifying biomarkers at very low concentrations. For example, the detection of cancer biomarkers, pathogens, and proteins associated with neurodegenerative diseases can be achieved with high sensitivity and specificity [44]. These sensors are also employed in detecting contaminants and pathogens in environmental samples, offering real-time monitoring capabilities that are critical for public health and safety. The portability and high sensitivity of metasurface-based biosensors make them suitable for point-of-care diagnostics, where rapid and accurate detection of diseases at the patient's location is essential. These sensors can be integrated into compact devices, providing immediate results without the need for complex laboratory equipment [45].
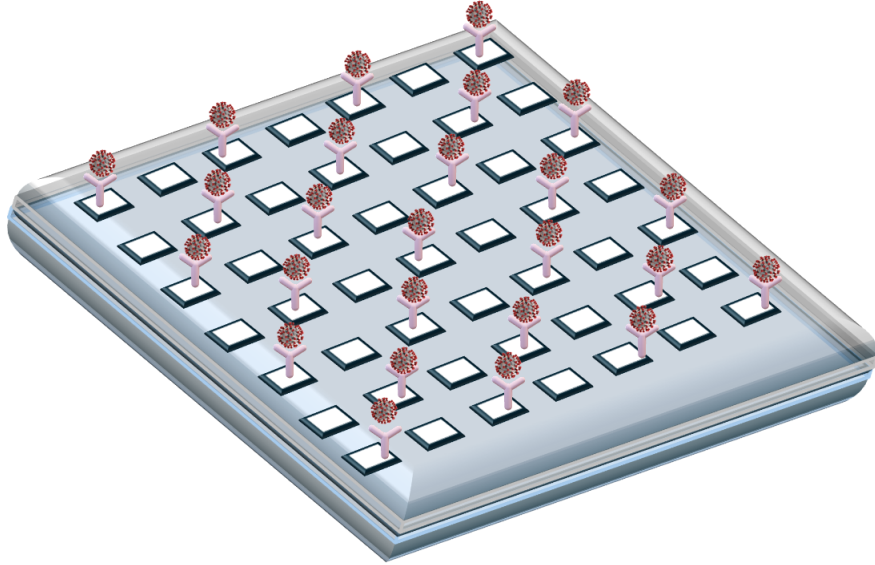
Figure 1.6: Illustration of a metasurface designed as biosensor. The pink "Y"s represent antigens while the grey balls with red bumps represent the corona virus; image adapted from [46].

Despite all the pros and the research suggesting that metasurfaces can be extremely useful, it is necessary to be realistic and also identify the cons of this still-developing technology. Metasurfaces, despite their significant potential in biosensing and other optical applications, face several challenges and limitations that must be addressed to fully realise their promise. One of the primary issues is the complexity of fabrication. Producing metasurfaces requires advanced nanofabrication techniques such as electron beam lithography, focused ion beam milling, and nanoimprint lithography. These processes are intricate, costly, and time-consuming, which limits scalability and the potential for large-scale commercialization. The high precision needed for these techniques makes mass production difficult and expensive, presenting a significant barrier to widespread adoption. Another challenge is the material limitations. Metasurfaces often rely on noble metals like gold and silver due to their plasmonic properties. However, these materials are not only expensive but also suffer from significant losses at optical frequencies, which can reduce the efficiency and sensitivity of the devices. Alternative materials such as dielectrics can

reduce losses but may not provide the same level of field enhancement, leading to a trade-off between performance and practicality. The environmental stability of metasurfaces is another concern. These structures can be sensitive to changes in environmental conditions such as temperature, humidity, and chemical exposure. Such sensitivity can affect their optical properties and, consequently, their performance in practical applications. Ensuring long-term stability and reliability under various operating conditions is crucial for the development of robust metasurface-based sensors. Integration with existing technologies poses further difficulties. For metasurfaces to be useful in real-world applications, they need to be integrated with other components and systems, such as microfluidics for lab-on-a-chip devices or electronic circuits for signal processing. Achieving seamless integration while maintaining performance and functionality is technically challenging and requires innovative engineering solutions. Finally, the theoretical and computational challenges should not be overlooked. Designing metasurfaces with desired properties involves complex simulations and optimisations, which demand significant computational resources. Accurate modelling of electromagnetic interactions at the nanoscale is critical, and small deviations in fabrication can lead to large discrepancies between the designed and actual performance. Thus, ongoing research in computational methods and design algorithms is essential to enhance the predictive accuracy and efficiency of metasurface design.

Metasurfaces are a rapidly evolving field with exciting possibilities for wave manipulation. The precise control of wavefronts and their properties enabled by metasurfaces has opened up new avenues for research and applications. The design strategies and applications discussed in this introduction are just a few examples of the potential of this technology. As researchers continue to innovate and refine metasurfaces, is possible to expect to see even more achievements in the future. For many years, the field of optical metasurfaces has been closely associated with plasmonic nanostructures, which, however, pose a significant challenge due to their high absorption losses. To overcome this issue,

this particular study has focused on designing and fabricating metasurfaces using amorphous silicon. This choice is motivated by the remarkable ability of amorphous silicon to minimise absorption losses at near-infrared and visible frequencies. The primary distinguishing feature of these metasurfaces is their ability to mitigate absorption losses while simultaneously ensuring precise control over light manipulation. This makes amorphous silicon metasurfaces particularly suitable for a range of applications, including advanced optics, optical communications, electronics, and experiments in solar energy conversion. Furthermore, the specific design of these metasurfaces addresses the challenges associated with high absorption losses, paving the way for new developments in key areas of optical technology and advanced materials.

1.3   Amorphous silicon (α-Si) metasurfaces

Amorphous silicon (α-Si) metasurfaces represent a significant advancement in nanophotonics due to their unique properties and versatility in manipulating light at specific wavelengths, particularly around the telecommunications wavelength of 1550 nm. The use of amorphous silicon, as opposed to crystalline silicon, offers several advantages, including ease of fabrication, cost-effectiveness, and compatibility with existing silicon-based technologies [47][48] (Fig. 1.7). α-Si is a non-crystalline form of silicon that can be deposited at lower temperatures compared to crystalline silicon, making it suitable for a variety of substrates, including flexible and transparent ones [49]. This flexibility in deposition conditions allows for the creation of high-quality, large-area metasurfaces with precise control over nanostructure dimensions and arrangements [24].

The key behaviour of amorphous silicon metasurfaces lies in their ability to manipulate light through subwavelength-scale features. These metasurfaces can control the phase, amplitude, and polarisation of light waves with high precision [17]. The optical properties
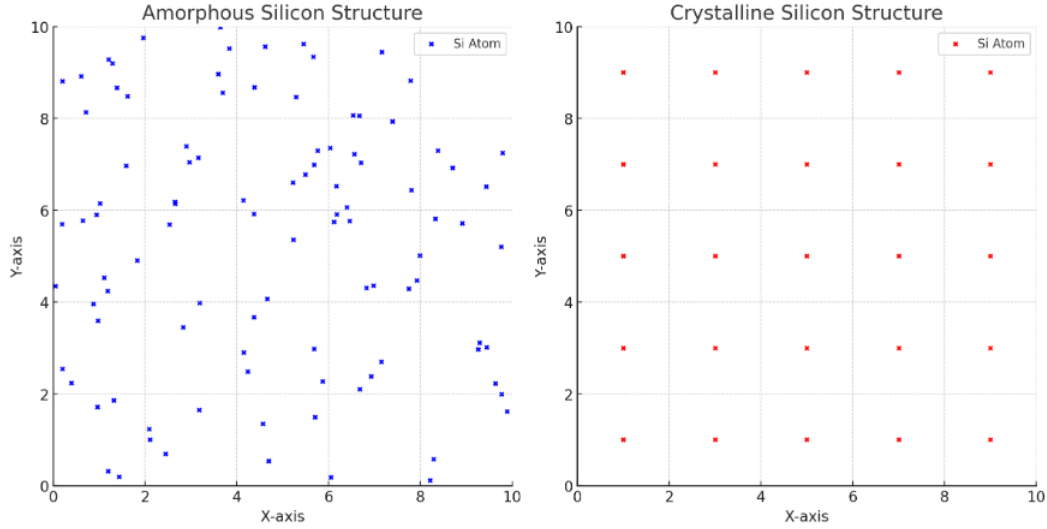
Figure 1.7: Chemical structures of α-Si and crystalline silicon. On the left side, the α-Si structure is depicted. In this model, silicon atoms (blue circles) are randomly distributed, reflecting the lack of long-range order. The random bonds between atoms are illustrated by the connecting lines, showing how the atoms are bonded in a non-crystalline, disordered fashion. On the right side, the crystalline silicon structure is shown. Here, silicon atoms (red circles) are arranged in a regular, repeating pattern, forming a well-defined crystal lattice. The bonds between atoms are depicted by the straight lines connecting adjacent atoms, illustrating the regular tetrahedral bonding configuration.

of α-Si, such as its high refractive index and low absorption in the near-infrared region, make it particularly effective for applications at 1550 nm, a critical wavelength for optical communication systems due to its low loss in optical fibres and minimal dispersion [50]. For instance, Arbabi demonstrated that amorphous silicon metasurfaces could be engineered to function as high-efficiency optical elements, such as lenses and beam deflectors, operating efficiently at 1550 nm [24]. By designing the metasurface with nanostructures that provide the desired phase shifts, they achieved near-diffraction-limited focusing and high transmission efficiency, essential for integrated photonic circuits and advanced imaging systems.

α-Si metasurfaces can also achieve high reflectivity and transmission control, which are crucial for creating reflective and transmissive optical devices. For example, Javed

designed an amorphous silicon metasurface mirror that achieved over 99% reflectivity at 1550 nm by optimising the size, shape, and arrangement of the silicon nanostructures to constructively interfere and reflect incident light effectively [51]. Additionally, α-Si metasurfaces can be tailored to exhibit various optical resonances, such as Mie resonances, which enhance light-matter interactions at specific wavelengths. This capability is particularly useful in applications like sensing, where the metasurface can be designed to enhance the sensitivity to changes in the surrounding environment by maximising the interaction between light and analytes at 1550 nm. As shown by Shalaev et al,, amorphous silicon metasurfaces with carefully engineered Mie resonators demonstrated enhanced sensitivity for detecting chemical and biological substances, leveraging the strong field confinement and high Q-factors achievable with α-Si structures [52].

One of the significant advantages of using amorphous silicon for metasurfaces is its compatibility with CMOS fabrication processes. This compatibility allows for the seamless integration of metasurfaces with existing silicon photonics infrastructure, facilitating the development of complex photonic integrated circuits [53]. Amorphous silicon can be deposited using plasma-enhanced chemical vapour deposition (PECVD, see chapter 3.4), a standard process in semiconductor manufacturing, ensuring scalability and reproducibility of the metasurface designs [7].

However, there are also challenges associated with amorphous silicon metasurfaces. The material can exhibit higher optical losses compared to crystalline silicon, particularly in the visible spectrum, due to the presence of defects and dangling bonds [7]. Nonetheless, these losses are significantly lower in the near-infrared region, making α-Si an excellent candidate for applications at 1550 nm. Furthermore, ongoing research aims to improve the material quality and reduce optical losses through advanced deposition techniques and post-deposition treatments.

The advantages of amorphous silicon for metasurfaces include its high refractive index,

which allows for significant phase manipulation with thin structures, its low absorption in the near-infrared region, which makes it efficient for applications at 1550 nm, its compatibility with standard CMOS fabrication processes, facilitating integration with silicon photonics, its cost-effectiveness due to lower fabrication temperatures and simpler processes compared to crystalline silicon, and its flexibility in design, allowing for deposition on various substrates, including flexible and transparent ones [53][7]. The challenges associated with amorphous silicon metasurfaces include higher optical losses in the visible spectrum due to defects and dangling bonds, fabrication complexity requiring high-resolution patterning techniques such as electron beam lithography or nanoimprint lithography, material stability issues over time, particularly under high-intensity illumination or harsh environmental conditions, and the challenge of achieving uniform performance across large-area metasurfaces, requiring precise control over the deposition and patterning processes [54].

Amorphous silicon metasurfaces are highly effective for manipulating light at 1550 nm due to their high refractive index, low absorption in the near-infrared region, and compatibility with standard silicon photonics fabrication processes. They enable a wide range of optical functionalities, including high-efficiency focusing, beam steering, and enhanced sensing, making them invaluable for telecommunications, imaging, and sensing applications. However, addressing challenges such as higher optical losses, fabrication complexity, and material stability is crucial for realising the full potential of amorphous silicon metasurfaces in practical applications [17].

Amorphous silicon metasurfaces are effective at the 1550 nm wavelength due to several critical factors that make this wavelength particularly important for telecommunications. The 1550 nm wavelength corresponds to the third telecommunications window, where optical fibres exhibit their lowest attenuation, typically around 0.2 dB/km, allowing signals to travel long distances with minimal loss. This wavelength also falls within the low dispersion region of silica optical fibres, minimising signal broadening and maintaining data

integrity over extended distances [14]. The 1550 nm wavelength also avoids the high water absorption peak around 1400 nm, ensuring clearer signal transmission. The combination of these factors makes the 1550 nm wavelength ideal for high-capacity, long-distance optical communication systems, as it supports dense wavelength-division multiplexing (DWDM), allowing multiple channels to be transmitted simultaneously, significantly increasing the data-carrying capacity of optical fibres [54].

1.4   Flat optics

Flat optics or metalens, an innovative branch of photonics, leverages planar surfaces with nanostructured patterns to manipulate light in ways traditionally achieved using curved lenses and bulky optical components. Flat optics operates by exploiting the interactions between light and nanostructures on the surface. When light encounters these structures, it experiences localised phase shifts that can be tailored by adjusting the geometry and arrangement of the nanostructures. This capability allows for precise control over the direction and properties of light, making flat optics highly versatile. For instance, by engineering the phase response of each element on a surface, one can create a flat lens, also known as a metalens, capable of focusing light similarly to a traditional curved lens but with a significantly reduced thickness and weight [15]. Flat optics also benefits from advancements in material science, particularly the development of high-refractive-index materials that enhance the interaction between light and the nanostructures. These materials, such as silicon, titanium dioxide, and gallium nitride, offer improved optical performance and broaden the operational bandwidth of flat optical devices [47]. Traditional optics relies on bulky and curved lenses or mirrors to focus and manipulate light. These components are typically made from materials like glass or plastic, which are shaped into precise curves to direct light beams. Flat optics, in contrast, utilises thin, planar

surfaces with nanostructured patterns to achieve similar or even superior optical effects. The key difference is that flat optics relies on engineered phase shifts at the nanoscale rather than relying on the macroscopic curvature of optical elements [15]. In conventional optics, light is manipulated through gradual changes in optical path length introduced by the curvature of lenses or mirrors. These changes cause the light waves to converge or diverge, forming focused images or directing beams. Flat optics, however, uses abrupt phase discontinuities introduced by nanostructured surfaces (Fig. 1.8). Each nanostructure on a surface can impart a specific phase shift to the incident light, allowing for precise control over the wavefront and enabling functions such as focusing, beam steering, and holography [14]. Traditional optical elements are typically designed for a single function, such as focusing or collimating light. Each function requires a separate optical component, leading to larger and more complex optical systems. Flat optics, on the other hand, offers unparalleled design flexibility. Flat optical surfaces can be engineered to perform multiple optical functions simultaneously within a single, compact layer. For example, a single surface can be designed to focus light while simultaneously correcting for chromatic aberrations [17].
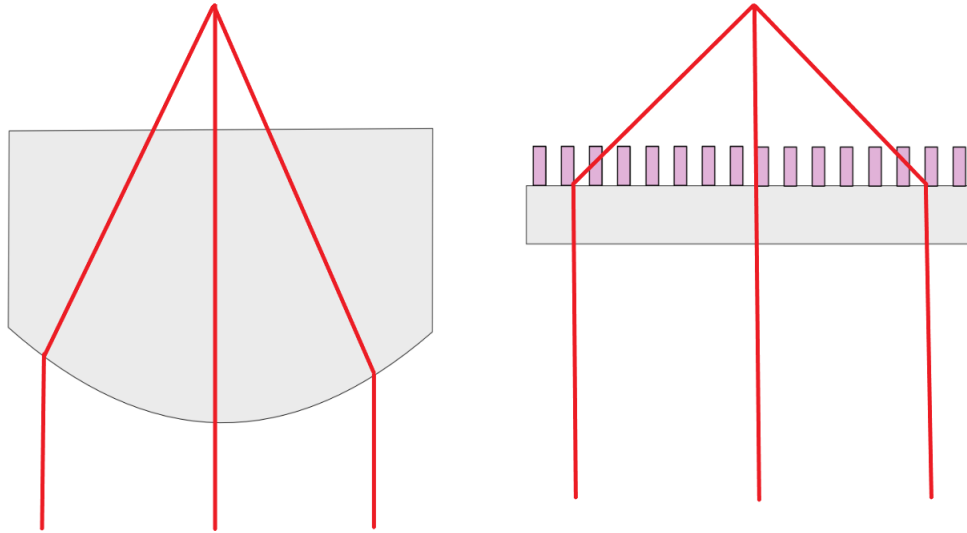
Figure 1.8: Principle of a) current in use lens and b) flat lens based on reconfigurable metasurface. The phase in b can be controlled by the modulation of the subwavelength metamolecules.

One of the most significant advantages of flat optics is the potential for miniaturisation. Traditional optical systems, with their bulky lenses and mirrors, are often limited in how compact they can be made. Flat optics, by using planar surfaces, drastically reduces the size and weight of optical components. This is particularly beneficial for portable and wearable devices, where space and weight are critical considerations [14]. While flat optics offers numerous advantages, it also faces challenges related to efficiency. Conventional optics, with its well-established materials and manufacturing processes, can achieve high efficiency with minimal losses. Flat optics, however, can suffer from scattering and absorption losses at the nanoscale, which can reduce the overall efficiency of optical components. Researchers are actively working to address these issues by optimising nanostructure designs and exploring new materials with better optical properties [55]. Flat optics offers several distinct advantages over traditional optical systems. One of the primary benefits is the significant reduction in size and weight, which is particularly important for portable and wearable devices. The planar nature of nanostructured surfaces allows for the integration of complex optical functions into a single, thin layer, leading to

more compact and lightweight designs. Additionally, flat optics provides unprecedented design flexibility. Flat optical surfaces can be engineered to perform multiple optical functions simultaneously, such as focusing and beam steering, which would typically require multiple conventional optical elements. This multifunctionality opens up new possibilities for optical system design and integration.

Flat optics also enhances the functionality of optical devices by enabling the manipulation of light in ways that are challenging or impossible with conventional optics. For example, flat optical surfaces can achieve extreme-angle beam steering and polarisation control, which are essential for advanced applications in imaging and telecommunications.

However, flat optics also faces several challenges. The fabrication of nanostructured surfaces with the required nanoscale precision is complex and often costly. Advanced nanofabrication techniques, such as electron beam lithography and nanoimprint lithography, are required to create the intricate patterns needed for effective light manipulation. These processes can be time-consuming and are currently more suitable for small-scale production and research purposes.

Another significant challenge is the efficiency of flat optical components. While flat optical surfaces offer remarkable control over light, they can suffer from efficiency losses due to scattering and absorption. These losses can reduce the overall performance of the optical device, particularly in applications requiring high light throughput or precise light manipulation. Researchers are actively working to improve the efficiency of flat optical surfaces by optimising their design and exploring new materials with better optical properties.

Material limitations also pose a challenge for flat optics. The performance of nanostructured surfaces is highly dependent on the materials used, which can have inherent limitations in terms of bandwidth and response times. For example, some materials may not perform well across a wide range of wavelengths or may exhibit slower response times,

limiting their applicability in certain scenarios [14][17][23][9][47].

1.4.1   Aberration in flat optics

One of the critical aspects in evaluating the performance of optical systems is the handling of various aberrations. These aberrations, which are imperfections that cause light to be improperly focused, lead to a range of image distortions. Below, the specifics of how flat optics addresses several key types of aberrations are discussed, highlighting the advantages this technology brings to various optical applications. ***Spherical Aberration***: occurs when light rays passing through the edges of a spherical lens focus at different points compared to those passing through the centre, resulting in a blurred image. Traditional optics often require complex multi-element lens systems to correct for spherical aberration. In contrast, flat optics can address this issue at the design stage [14]; the image below shows how the spherical aberration looks like (Fig. 1.9):
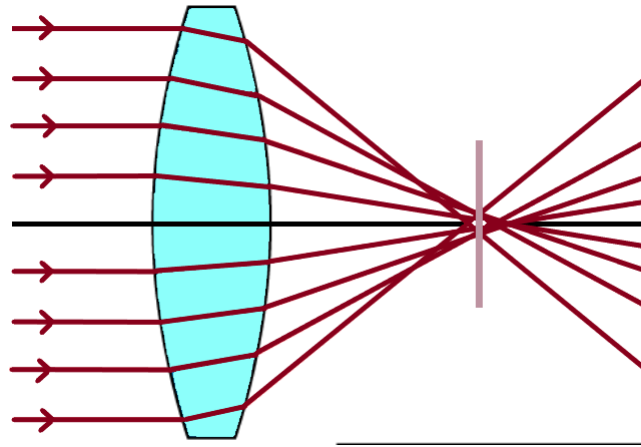
Figure 1.9: Lens with spherical aberration. It happens when the light's rays are focusing at different points after passing through a spherical lens or surface. The red lines represent the light, the black one is the optical axis while the pink is the focal point.

Comatic aberration, or coma (Fig. 1.10), causes off-axis points of light to appear

comet-shaped in images, with tails pointing away from the optical axis. This is particularly problematic in astrophotography and other applications requiring high precision. Traditional optics often combat coma with aspherical lens elements and intricate alignment. Flat optics can directly correct for coma by tailoring the phase profile of the surface to ensure uniform focusing across the entire field of view. This eliminates the need for multiple corrective elements and simplifies the optical design [56].
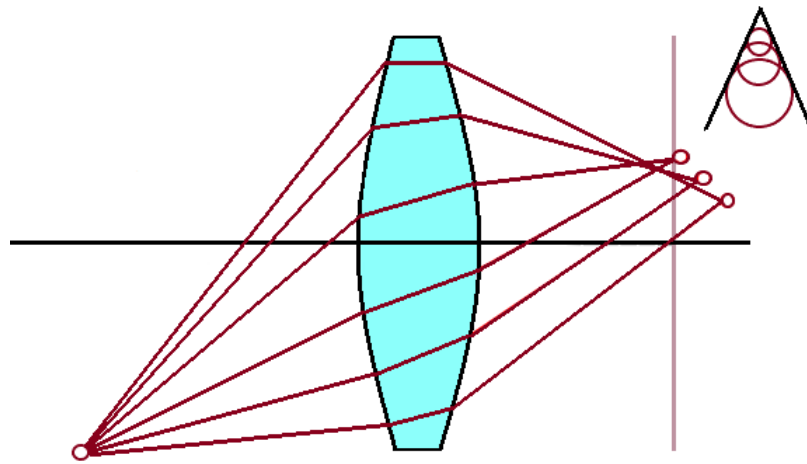
Figure 1.10: Lens with coma aberration. It happens as light rays from the edges of the frame pass through various parts of a spherical surface, creating a series of asymmetrical circular shapes of increasing sizes. The red lines represent the light, the black one is the optical axis while the pink is the focal point.

Chromatic aberration is a significant challenge in optical design, arising because different wavelengths of light are refracted by different amounts, leading to colour fringing in images (Fig. 1.11). Traditional optics address chromatic aberration with compound lenses made of different materials to compensate for the varying dispersion. In flat optics, chromatic aberration can be corrected by engineering nanostructures that provide wavelength-dependent phase shifts, allowing all colours to focus at the same point [57].
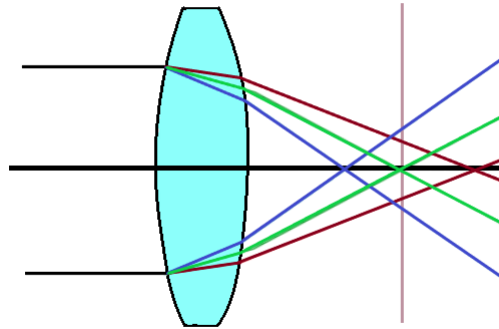
Figure 1.11: Lens with chromatic aberration. Focus difference results in colour fringes. The grey lines represent the light, the black one is the optical axis while the pink is the focal point.

Astigmatism in optical systems occurs when light rays in different planes are focused at different points, causing images to be blurred in certain directions (Fig. 1.12). Traditional lenses require cylindrical elements or additional corrective lenses to address astigmatism. Flat optics can mitigate astigmatism through the precise control of phase shifts at each point on the surface, allowing for the correction of these aberrations without the need for additional components [58].
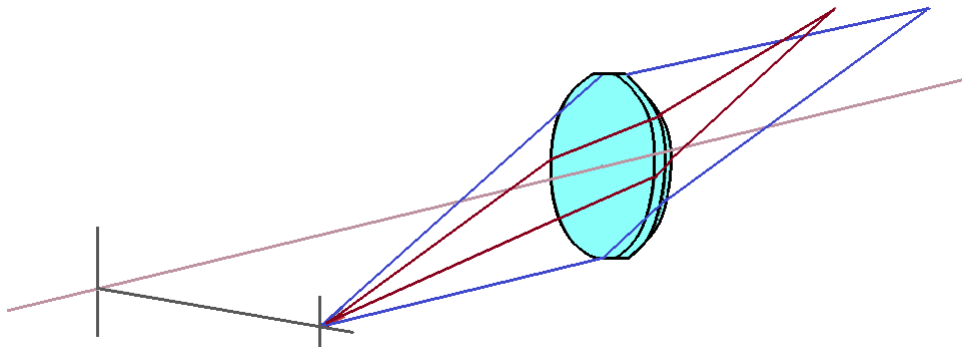
Figure 1.12: Lens with astigmatism. It occurs when rays that propagate in two perpendicular planes have different focal points. The gray lines represent the light, the black one is the optical axis while the pink is the focal point.

1.4.2 Application of flat optics

The key feature of flat optics is its ability to manipulate light in ways that traditional optical elements cannot. For this reason, this technology holds the potential for applications across various fields.

Metalenses can revolutionise the field of ***imaging***, in particular tomography, enabling non-destructive inspection, particularly in endoscopy. They can replace traditional catheters with a metalens to achieve subdiffraction-limited imaging and extended depth of focus with negligible astigmatism [59]. In 2019, an aplanatic metalens-based spectral tomographic imaging system was proposed, offering high transverse and longitudinal resolution [60]. In microscopic imaging systems, where the distance between the objective lens and the sample is quite short, the visual field approximates a spherical wave rather than a plane wave. Hyperbolic metalenses, designed to process plane waves, can cause significant spherical aberration in such scenarios. However, an aplanatic metalens designed for spherical wave incidence can focus the objective field without spherical aberration, achieving high resolution in both transverse and longitudinal directions. Metalenses can also detect depth information in addition to imaging objects in the focal plane. Light-field imaging, which measures both the intensity of the scene and the direction of light rays, has been widely used to reconstruct out-of-focus images and obtain depth information of objects [61][62].

Metalenses can revolutionise ***optical communication*** systems by replacing traditional lenses in photonic integrated circuits (PICs), resulting in more compact designs without compromising performance. This is particularly beneficial for data centres and telecommunication hubs where space is limited, and efficient light management is crucial [15]. In telecommunications, metalenses enhance signal processing and antenna systems. They achieve high-precision light manipulation and extended bandwidth capabilities with

minimal losses [63]. A metalens-based spectral multiplexing system proposed in 2019 offers high efficiency and minimal crosstalk in optical communication channels [64]. In fibre optic communications, traditional lenses designed for plane wave processing can degrade signals. Hyperbolic metalenses can cause spherical aberrations, but aplanatic metalenses, designed for spherical wavefronts, can focus optical signals without these aberrations, achieving high data transmission rates and reduced signal loss. Metalenses also enhance photonic circuits by detecting and processing depth information alongside the main signal. Light-field processing in telecommunications, which measures both the intensity and direction of light waves, is widely used to optimise signal routing and manage data traffic effectively [65][15]. Furthermore, metalenses enable advanced optical functions, such as creating compact beam steering devices essential for LiDAR systems and other applications requiring dynamic light direction control. Their unique properties also allow for novel optical components like non-reciprocal devices and enhanced optical filters, expanding the capabilities of telecommunication networks [25].

Flat optics can revolutionise ***optical computing systems*** by replacing traditional optical elements in photonic integrated circuits (PICs), resulting in more compact designs without compromising performance. This is particularly beneficial for data-intensive applications where space is limited, and efficient light manipulation is crucial [66]. In optical computing, flat optics enhance signal processing and computing systems by achieving high-precision light manipulation and extended bandwidth capabilities with minimal losses [67]. For instance, flat optics can be used to design more efficient and compact optical interconnects, which are essential for high-speed data transfer in computing systems [66]. A nonlocal flat optics-based system proposed in recent research offers high efficiency and minimal crosstalk in optical computing channels. These systems utilise the principles of nonlocality to achieve better control over light propagation and interaction, leading to improved performance in optical computing applications [66]. In optical computing,

traditional lenses designed for plane wave processing can degrade signals due to aberrations. Flat optics, especially those designed for spherical wavefronts, can focus optical signals without these aberrations, achieving high data transmission rates and reduced signal loss. This precise light manipulation is crucial for the effective functioning of optical computing systems [66]. Furthermore, flat optics enable advanced optical functions, such as creating compact beam steering devices essential for dynamic light direction control in computing applications. Their unique properties also allow for novel optical components like non-reciprocal devices and enhanced optical filters, expanding the capabilities of optical computing systems [66][67]. Another important application is ***Augmented reality and virtual reality*** where this technology can replace traditional optical components in headsets, leading to more compact and efficient designs without sacrificing performance. This is particularly advantageous for wearable augmented reality (AR) and virtual reality (VR) devices, where space and weight are critical considerations. In AR and VR, flat optics significantly improve display systems by enabling high-precision light manipulation and extended bandwidth capabilities with minimal losses. This ensures that virtual images are rendered with high clarity and low latency, which is crucial for creating immersive and responsive user experiences [68]. Traditional lenses in AR and VR headsets can introduce aberrations that degrade image quality. Flat optics, such as metalenses, especially those designed for spherical wavefronts, can focus optical signals without these aberrations. This capability results in clearer and more accurate virtual images, essential for maintaining the illusion of reality in VR and the seamless integration of digital elements in AR. Metalenses, for example, have been shown to focus RGB colours without chromatic aberration, providing high-quality imaging for AR and VR applications [69]. Furthermore, flat optics enable advanced optical functions, such as creating compact beam steering devices essential for dynamic light direction control in AR and VR headsets. These devices are crucial for tracking and responding to user movements in

real-time. The unique properties of flat optics also allow for the development of novel optical components like non-reciprocal devices and enhanced optical filters, expanding the functional capabilities of AR and VR systems [69]. The implementation of flat optics in AR and VR devices is also driven by their ability to minimise the overall weight and bulk of headsets, making them more comfortable for extended use. This improvement is vital for consumer acceptance and the practical usability of AR and VR technologies in various applications, from gaming and entertainment to professional and educational settings [68].

1.5   Fibre sensing technology

Fibre sensing technology encompasses a diverse range of techniques that leverage optical fibres to measure various physical parameters.

The evolution of global communication technology has been significantly shaped by the advancement of optical fibre technology. In the 1970s, the introduction of low-attenuation optical fibres paved the way for high-bandwidth, long-distance communications. This breakthrough led to a substantial increase in the production volume of optical fibres, with global deployment reaching a rapid pace by the year 2000 [70][71].

One of the key contributions to the widespread adoption of optical fibre technology was the discovery of photosensitive optical fibres in 1978 by Hill [72], which laid the foundation for the optical fibre Bragg Grating (FBG). Bragg gratings, integrated into optical fibre sensors, gained prominence due to their versatility in sensing applications across various industries, including aeronautics, aerospace, civil engineering, and biomedical monitoring [73].

Optical fibres, beyond their role in communication channels, serve as versatile sensing solutions for diverse applications. They leverage various optical parameters of guided

light, such as intensity, phase, polarisation, and wavelength, allowing the measurement of several parameters by detecting changes in light properties within the fibre[28]. These fibres exhibit electromagnetic passivity, making them suitable for environments with high electric fields and explosion risks. Additionally, their resistance to most chemical and biological agents, small size, and lightweight nature contribute to their suitability for challenging environments [73].

The low optical attenuation of optical fibres facilitates long-distance propagation, making them ideal for multiplexed measurements. Large arrays of distributed sensors can operate without active optoelectronic components in the measurement area, maintaining electromagnetic passiveness and environmental resistance [74][70]. Recent attention has turned to integrating optical fibre sensors into Wireless Sensor Networks (WSNs) for the design of advanced hybrid-sensing systems [75].

Optical fibres, functioning as cylindrical dielectric waveguides, find applications in sensing based on their expansion or contraction in response to strains or temperature variations. They offer advantages such as small size, no requirement for electrical power at remote locations, and the ability to multiplex many sensors along the fibre's length. Additionally, optical fibre sensors are immune to electromagnetic interference, do not conduct electricity, and can withstand high temperatures, enabling usage in diverse environments [73].
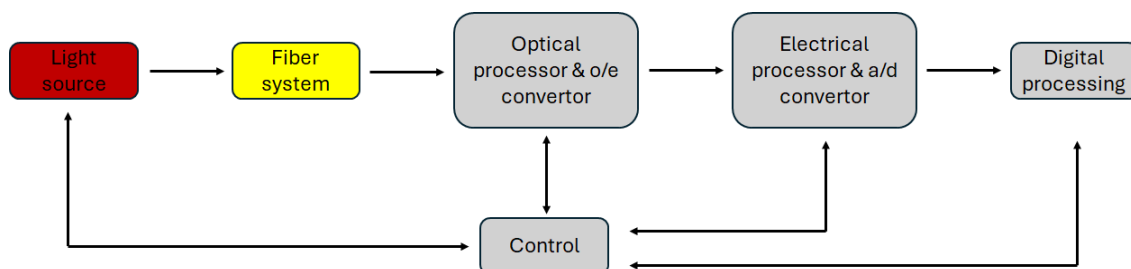
Figure 1.13: Diagram of the fibre optic sensing system operation, showing signal flow and control components; adapter from [76]

The Fig. 1.13 illustrates the fibre sensing system's operation and explains each component and the flow of the process. The light source, usually a laser, generates the light used in the fibre system. This light is directed into the fibre system, which may include optical splitters, couplers, isolators, circulators, and other necessary optical devices. The light signal then moves to the optical processor, which may include signal amplification, filtering, and coherent detection elements. This block also contains the optical-to-electrical (O/E) converter, transforming the optical signal into an electrical signal (current and/or voltage). Optical detectors convert the stream of photons into an electrical signal processed by conventional electronics. Next, the electrical signal is sent to the electrical processor for further processing, such as amplification or filtering. This block includes an analog-to-digital (A/D) converter that converts the analog signal into a digital form for further processing. The digitised signal undergoes digital processing, where the data can be analyzed, interpreted, and used for various applications. A control system manages and adjusts the operation of the light source, optical processor, and electrical processor, ensuring the entire sensing system operates efficiently. The arrows in the diagram indicate the signal flow through the system and the control pathways that maintain optimal performance [76].

The classification of optical fibre sensors can be based on aspects like their location, operating principle, or application. In terms of application types, these sensors can measure physical, chemical, or biomedical parameters. Considering location, sensors can be intrinsic or extrinsic. Intrinsic sensors use the optical fibre both as the sensitive material and to transport the optical signal, while extrinsic sensors guide the light to/from an external sensor head. Intrinsic optical fibre sensors find applications in diverse fields, including seismic and sonar applications, oil wells, healthcare, airplanes, and cars. Extrinsic sensors measure parameters like vibration, rotation, displacement, velocity, acceleration, torque, and temperature, offering resistance to noise and signal corruption [73].

Amidst the global COVID-19 pandemic, there has been an intensified focus on personal health and life safety. Wearable sensors have emerged as groundbreaking technology for real-time human health monitoring, witnessing substantial development with billions of dollars in global investments. These sensors enable users to access personal health data without leaving their homes, contribute to healthcare cost reduction through early prevention, and generate substantial medical data, driving advancements in the medical and health industries [77].

Wearable devices, imposing higher demands on sensors, require superior sensing capabilities and optimal wearing comfort. Currently, flexible electronic sensors dominate the market, incorporating conductive nanomaterials and polymers for excellent mechanical flexibility and electrical sensing performance. However, these sensors have drawbacks, such as poor biocompatibility and susceptibility to electromagnetic interference and electrical safety issues [75].

The emergence of photonic sensors, particularly optical fibre sensors (OFSs), presents a compelling alternative. OFSs offer unique advantages like broadband, long-distance transmission, multi-parameter measurement, corrosion resistance, and resistance to electromagnetic interference. Suited for hazardous environments, they have found applications in various domains, including factory processing, aerospace, marine vessels, bridges and tunnels, healthcare, and the military. OFSs boast high sensitivity, fast response speed, low production costs, reliability, flexibility, convenience, safety, reliability, and excellent biocompatibility, making them a novel solution for wearable sensors.

OFSs technologies offer sensing solutions in challenging environments where traditional electronic sensors may fail. Various OFSs technologies have been developed to measure mechanical, chemical, and thermal parameters for point, quasi-distributed, and distributed sensing applications. Distributed fibre sensors, particularly Brillouin-based

and Rayleigh-based, have gained significant attention over the last decade. Brillouin-based fibre sensors operate based on the principle of Brillouin scattering, a phenomenon where an incident light wave interacts with density variations or acoustic phonons within the optical fibre, resulting in the scattering of light at a different frequency. This frequency shift, known as the Brillouin frequency shift, is sensitive to changes in temperature and strain along the fibre. The key characteristics of Brillouin scattering include its sensitivity to temperature and strain, which allows for the precise measurement of these parameters over long distances with high spatial resolution, typically in the range of centimetres to metres [78][79].Brillouin-based sensors are particularly effective for structural health monitoring (SHM) of large civil structures like bridges, dams, and buildings, where they can detect changes in strain and temperature that may indicate structural integrity issues. They are also used in the energy sector for monitoring pipelines and power cables, where thermal or mechanical stresses can lead to potential failures. In geotechnical engineering, Brillouin-based sensors measure strain and temperature in applications like tunnels and embankments, providing valuable data for assessing structural stability and safety [80][81]. Rayleigh-based fibre sensors, on the other hand, utilise Rayleigh scattering, which occurs when light interacts with microscopic variations in the refractive index of the fibre. This scattering is elastic, meaning the scattered light has the same frequency as the incident light. Changes in the intensity of the backscattered light are analyzed to detect variations in strain and temperature. Rayleigh-based sensors are known for their high spatial resolution, often in the range of millimetres, which allows for detailed monitoring of strain and temperature changes along the length of the fibre[82][83]. Rayleigh-based sensors are widely used in infrastructure monitoring, where they provide continuous, distributed measurements of critical infrastructure such as railways, roads,

and bridges. These sensors help in the early detection of strain and temperature anomalies that could indicate potential structural issues. In security and surveillance applications, Rayleigh-based sensors are used to detect intrusions or tampering by monitoring strain along fences or borders. Additionally, these sensors are employed in environmental monitoring to measure temperature variations in applications like monitoring glaciers and ice sheets [84][80]. While both Brillouin-based and Rayleigh-based fibre sensors offer significant advantages for distributed sensing applications, they differ in their sensitivity and resolution. Brillouin-based sensors are known for their high sensitivity to strain and temperature with moderate spatial resolution, making them suitable for applications requiring precise measurements over longer distances. Rayleigh-based sensors, with their higher spatial resolution, are ideal for applications requiring detailed mapping of strain and temperature changes over shorter distances [84].

In parallel with these advancements, the digital revolution has witnessed the rise of smart devices, incorporating sensor hardware and AI software for intelligent task execution. Smart sensors, ranging from voice-enabled home devices to applications in the Industrial Internet of Things (IIoT), have become integral to daily life. This revolution is fueled by the miniaturisation of sensing hardware, easy access to cloud and high-performance computing, advancements in big data storage and analytics, and breakthroughs in ML and AI technologies [85].

The significant breakthroughs in AI, particularly since 2012, are attributed to deep learning, a subset of ML utilising biologically inspired neural networks. Deep neural networks (DNN) automatically generate features during the learning process, distinguishing them from conventional ML algorithms. AI-powered sensors play a foundational role in the IIoT, often referred to as the fourth industrial revolution. They are integral to industrial infrastructure, enabling intelligent functions like automated asset monitoring, fault detection, and predictive maintenance [86]. It is precisely in this last scenario that a good

part of the doctoral path was concentrated as machine learning algorithms were used (see chapter 2. for the theory and chapters 5 and 6 for the practical application) and deep learning in fibre sensing which led to the publication of an article [87].

1.6   Walkthrough

In the upcoming chapters, the experiments conducted and the results obtained during this PhD journey will be thoroughly explained.

In Chapter 2, the theoretical concepts will be presented, which are essential for a comprehensive understanding of the research's purpose and the primary techniques/tools used for the proper execution of the experiments.

Chapters 3 and 4 detail all the instruments utilised for the fabrication and characterisationof the device (Chapter 3), the analyses conducted in the optics laboratory after preparing the optical setup, and the obtained results (Chapter 4).

Chapter 5 covers the experiments and results that led to the publication of a paper regarding the bending of two different types of fibres under various conditions, analyzed using Machine Learning (ML) algorithms.

Chapter 6 is served as a natural progression from the preceding chapter, where the outcomes achieved with longer fibres, namely 100 m and 1 km, are delved into. Additionally, further experiments are encompassed in this chapter, which were conducted to validate the efficacy of the algorithm introduced in Chapter 5.

Meanwhile, Chapter 7, being the concluding chapter, provides a comprehensive recap of all the work undertaken, the conducted experiments, the achieved outcomes, and potential future developments.

Chapter 2

Background theory

2.1 Introduction

The focus of this chapter is to give a general overview of the basic notions necessary to understand the concept of this work. Concepts such as wave theory, structured light, OAM, the functioning of the tools used and other necessary knowledge will be introduced.

2.2 One of the greatest debate in physics

One of the most famous debates in physics revolves around the question of whether light is a wave or a particle. In the early 17th century, René Descartes proposed that light is a wave, a theory that explained phenomena like reflection and refraction. However, Isaac Newton challenged this view 40 years later, arguing that light is made up of particles. Around the same time, Robert Hooke and Christian Huygens [88] provided mathematical models supporting the wave theory.

This debate persisted until 1803, when Thomas Young's double-slit experiment showed that light behaves like a wave, creating an interference pattern. Interestingly, Young also found that electrons, known to be particles, produced similar interference patterns, raising

further questions about light's nature [89].

In the 19th century, Augustin Fresnel's experiment confirmed light's wave behavior by demonstrating diffraction patterns, known as Poisson's or Arago's dot [90]. James Clerk Maxwell later developed equations describing light as an electromagnetic wave [91]. However, in the early 20th century, Max Planck and Albert Einstein provided evidence supporting light's particle nature, introducing the concept of quantized energy and the photon [92] [93].

By 1927, the idea of wave-particle duality was introduced at the fifth Solvay Conference by Niels Bohr. He suggested that light and electrons exhibit both wave and particle characteristics, depending on how they are observed, resolving the longstanding debate [94].

2.3   Snell's law and generalised Snell's Law

Snell's Law is a fundamental principle in optics that describes the relationship between the angles of incidence and refraction when a light ray passes through the boundary between two different media. This law is crucial for understanding how light behaves in various materials [95]. Recent advancements in engineered materials, such as metasurfaces, have necessitated a generalised version of Snell's Law to account for additional phase shifts introduced by these materials [96]. Classical Snell's Law defines the behaviourof an incident light ray at the boundary between two materials, describing both reflection and refraction. When a high-frequency electromagnetic wave, represented as a straight ray, hits the boundary between two mediums at an angle of incidence (α_1) relative to the normal, two phenomena occur:

- **Reflection**: Part of the incident energy remains in the original medium.
- **Refraction (Transmission)**: The rest of the energy passes into the second

medium.

The angle of reflection equals the angle of incidence. The angle of refraction (α_2) follows Snell's Law:

$$\eta_1 sin\alpha_1 = \eta_2 sin\alpha_2 \tag{2.1}$$

where η_1 and η_2 are the refractive indices of the two media. For angles of incidence greater than the critical angle (α_C), total internal reflection occurs:

$$\alpha_C = sin^2(\eta_2/\eta_1) \tag{2.2}$$

This results in all the incident energy being reflected, confining it within the originating medium without propagation into the second medium.

generalised Snell's Law applies to metasurfaces, which are artificially structured materials designed to control electromagnetic waves. Metasurfaces introduce an additional phase shift gradient across their surface, modifying the traditional behaviourof light refraction and reflection. The generalised Snell's Law is expressed as:

$$\eta_1 sin\alpha_1 - \eta_2 sin\alpha_2 = (\lambda/2\pi)(d\phi/dx) \tag{2.3}$$

where:λ is the wavelength of the incident light, $\phi(x)$ is the position-dependent phase shift imparted by the metasurface and ($d\phi$/dx) is the gradient of the phase shift along the metasurface.

The key difference between the classical and generalised Snell's Law lies in the phase shift gradient introduced by metasurfaces. While classical Snell's Law only considers the refractive indices of the two media, the generalised version incorporates an additional term to account for the phase shift gradient imparted by the metasurface. This allows for more precise control over the direction of the refracted light, enabling advanced applications

such as beam steering and flat lenses. The Fig. 2.1 represent an illustration of these two concepts:

Classical Snell's law

η_1

α_2

α_1

η_2

Generalised Snell's law

η_1

α_2 with phase shift

α_1

η_2
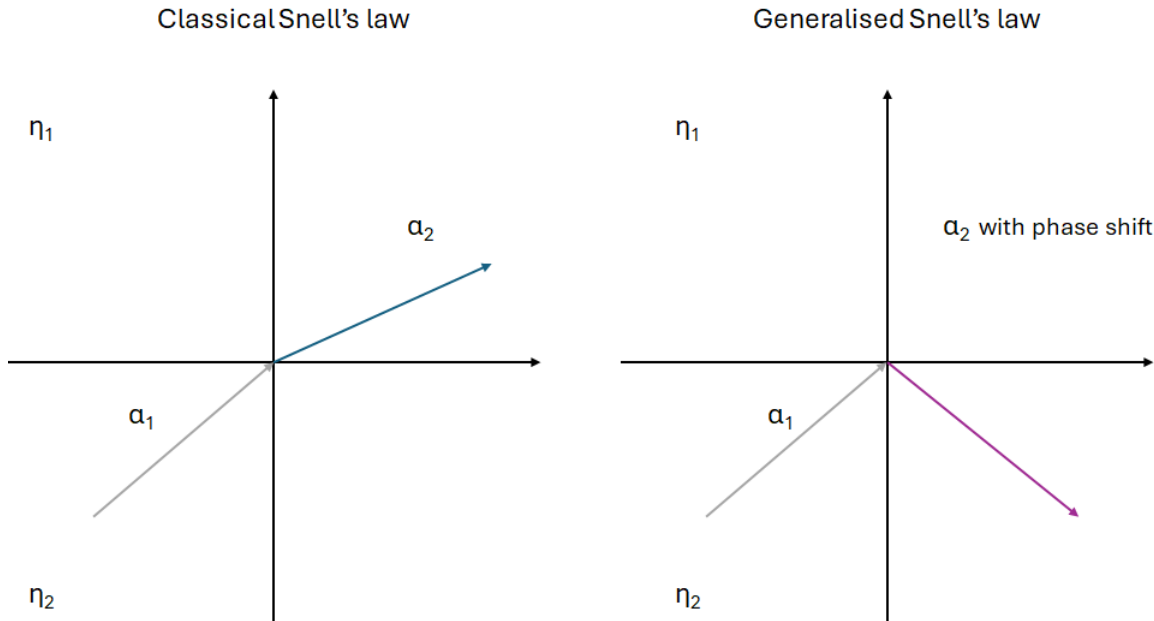
Figure 2.1: Diagrams representing Snell's Law and generalised Snell's Law with a phase shift

These diagrams demonstrate the additional control over light propagation offered by metasurfaces, allowing for precise manipulation of the refracted rays. In the graph for classical Snell's Law, the incident ray strikes the interface between two media (η_1 and η_2). The refracted ray follows the traditional Snell's Law without any additional phase shifts, and the angles of incidence (α_1) and refraction (α_2) are marked; in the graph for generalised Snell's Law with Phase Shift, the incident ray strikes the metasurface. The metasurface introduces an additional phase gradient, altering the refraction angle (α_2 with phase shift) compared to the classical scenario. The angles of incidence (α_1) and the modified refraction angle (α_2 with phase shift) are marked [39][97].

2.4 Modes of Light

Optics is a branch of physics that investigates the behaviourof light and its interactions with matter. Within this expansive domain, one of the most intriguing aspects is the versatility of light in adopting various spatial configurations, referred to as "modes of light." Two prominent and distinct families of light modes are Laguerre-Polynomial (LP) and Hermite-Gaussian (HG) modes. These modes exhibit unique characteristics, precise mathematical descriptions, and diverse applications spanning from advanced microscopy to quantum optics.

Laguerre-Polynomial (LP) modes, although less commonly discussed, also play a significant role in the study of light modes. Each of these families of light modes has its own generation mechanisms and specific applications, making them invaluable tools in both theoretical and applied optics. In the following subparagraphs, the differences between the HG, LG, and LP modes, their generation mechanisms, and applications will be explained in detail [98].

2.4.1 Hermite-Gaussian (HG) modes

Hermite-Gaussian (HG) beams are solutions to the paraxial wave equation and are characterised by their linearly polarised nature and degenerate edge dislocations in their wavefronts. These dislocations appear as dark lines positioned between mode spots with phase shifts, giving HG beams a distinct spatial structure [99]. HG modes are renowned for their bell-shaped intensity distribution in light, often described as a Gaussian profile. These modes are governed by Hermite-Gaussian equations and are determined by two integer quantum numbers, n and m, which correspond to the number of nodes along the x and y axes, respectively [98]. For example, the mode with $n=2$ and $m=1$ is denoted as HG(2, 1); as shown in the Fig. 2.2.

HG modes exhibit symmetry about x and y axes and have their peak intensity at the centre of the beam. The symmetry and node structure are determined by the Hermite polynomials $H_{(n)}$ and $H_{(m)}$, which introduce nodes (zeros) along the x and y axes, respectively; additionally, these modes exhibit rectangular symmetry along the Cartesian axes.
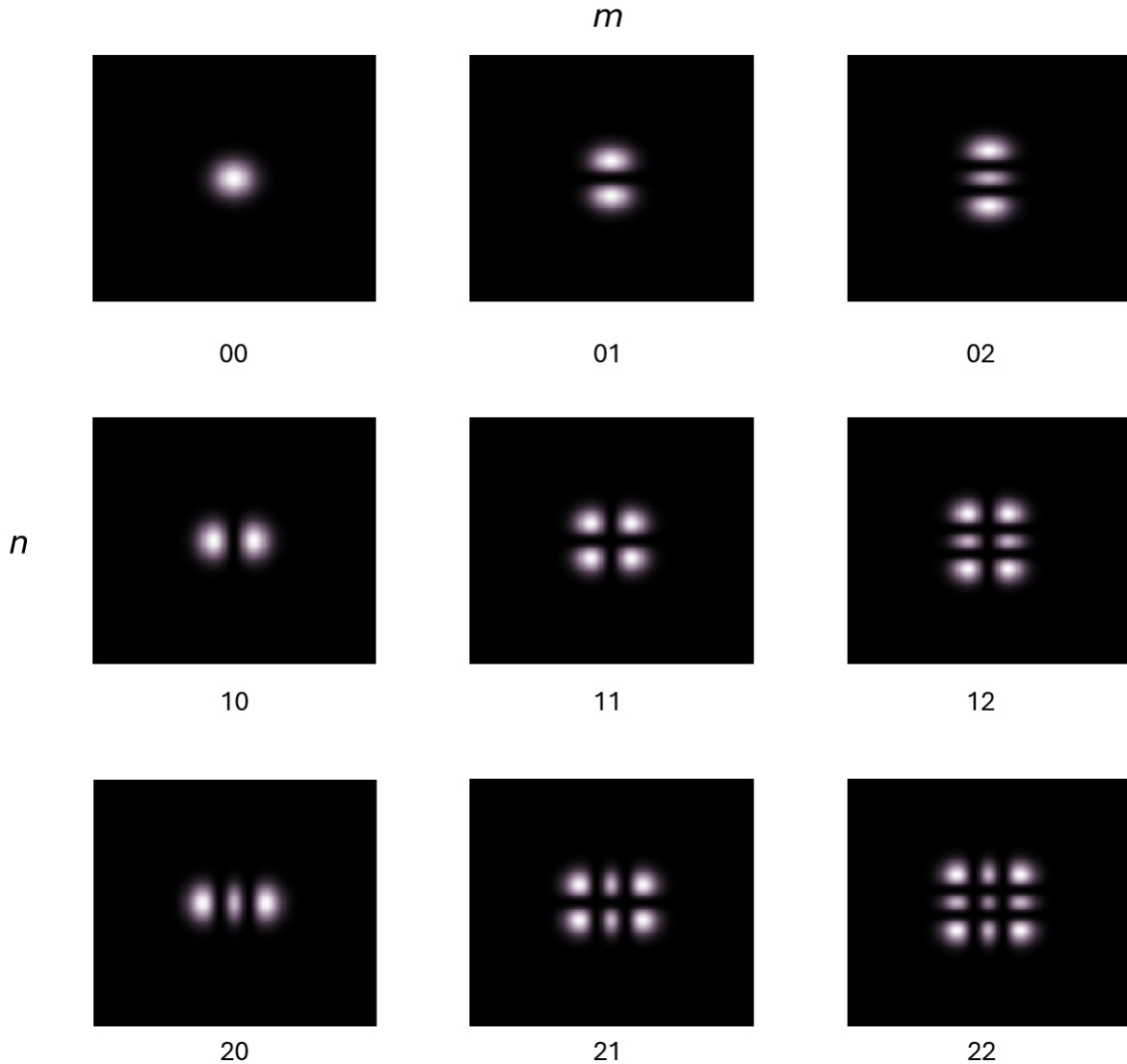
Figure 2.2: Intensity distribution of HG modes from 00 (top left side) to 23 (bottom right side); adapted from [100].

The mathematical expression for HG modes is as follows:

$$HG_{nm}(x, y, z) = \frac{1}{w(z)} C_{nm} H_n \left(\sqrt{2} \frac{x}{w(z)} \right) H_m \left(\sqrt{2} \frac{y}{w(z)} \right) \exp \left(-\frac{x^2 + y^2}{w(z)^2} \right)$$
$$\exp \left(-ikz - i(m + n + 1)\zeta(z) \right) \tag{2.4}$$

where $C_{(nm)}$ represent a normalisation constant, $H_{(n)}$ and $H_{(m)}$ are the Hermite poly-nomials of degree of respectively n and m, while the w(z) is the beam size [100], k, equal to $\frac{2\pi}{\lambda}$ is the wave number and $\zeta(z)$ is the Gouy phase shift, given by arctan $\frac{z}{zR}$.

The phase of a Hermite-Gaussian mode includes the plane wave phase, -kz, representing the propagation along the z-axis and the Gouy phase shift, -$(m+n+1)\zeta(z)$, representing an additional phase shift that depends on the transverse mode indices m and n. This phase shift accumulates as the beam propagates and is more significant near the focus (around $z=0$). The phase profile can be visualized as the angle of the complex electric field distribution; the Fig. 2.3 represent the phase profile of the HG modes:
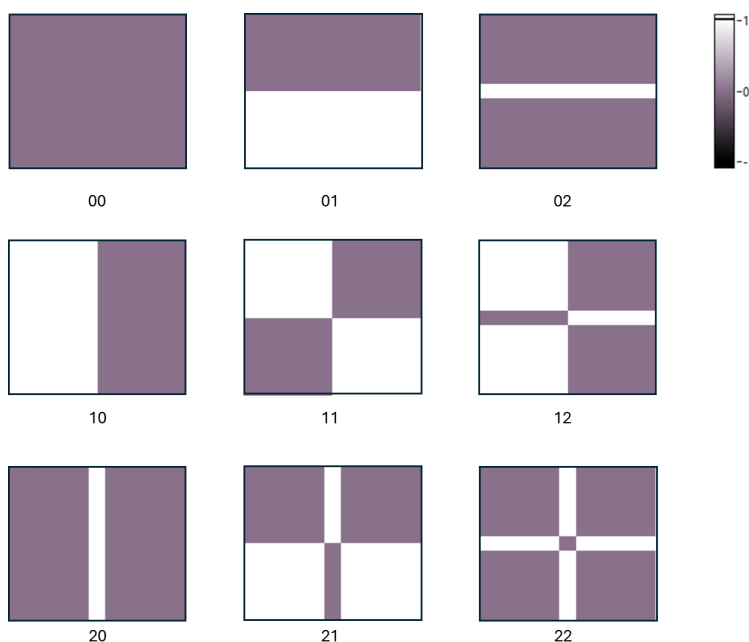
Figure 2.3: Phase distribution of HG modes from 00 (top left side) to 23 (bottom right side); adapted from [100] made with Labview.

The Amplitude distribution of the Hermite-Gaussian mode is described by the product of Hermite polynomials and a Gaussian envelope. The Gaussian envelope defines the overall shape of the beam, while the Hermite polynomials introduce nodes (zeros) in the intensity distribution [101].

The intensity $I_{(nm)}(x,\ y,\ z)$ of the beam is given by the square of the absolute value of the electric field:

$$I_{nm}(x, y, z) = |E_{nm}(x, y, z)|^2 \tag{2.5}$$

for the fundamental mode, TEM$_{00}$ (transverse electro-magnetic), the intensity distribution is purely Gaussian:

$$I_{00}(x, y, z) = |E_0|^2 \frac{1}{w(z)^2} exp(-\frac{2(x^2 + y^2)}{w(z)^2}) \tag{2.6}$$

for higher-order modes, the intensity distribution will include the Hermite polynomials, which introduce additional structure such as nodes and lobes in the transverse plane [101].

These modes can be generated employing various optical devices, including phase masks, cylindrical lenses, and prisms [102]. These devices facilitate the modulation of the phase and amplitude of light in a precise manner to attain the desired HG mode shape. Additionally, HG lasers can be engineered using specially designed laser cavities that promote the generation of coherent HG modes [103].

2.4.2 Laguerre-Gaussian (LG) modes

Laguerre-Gaussian (LG) modes are another family of solutions to the paraxial wave equation in optics, characterised by their doughnut-shaped intensity distribution and helical phase structure. Unlike Hermite-Gaussian (HG) modes, which are defined by Cartesian coordinates, LG modes are more naturally described in cylindrical coordinates.

These modes are determined by two integers, p and q, where p represents the radial index (number of concentric rings) and q denotes the azimuthal index, corresponding to the number of intensity rings and the number of 2π phase windings around the beam axis, respectively. For example, the mode with $p=0$ and $q=1$ is denoted as LG_{01} [98]; as shown in the Fig. 2.4 below:
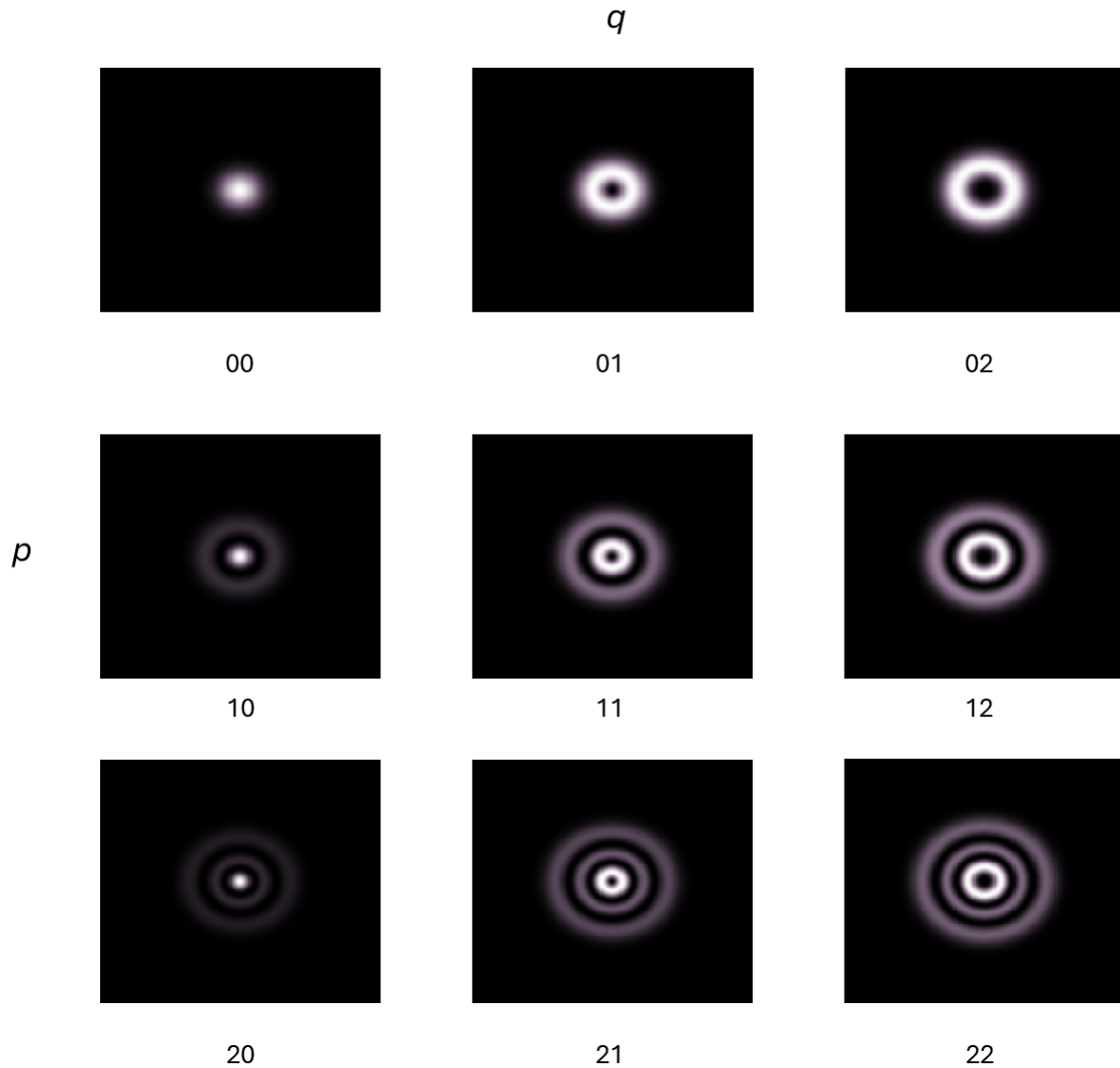
Figure 2.4: Intensity distribution of LG modes from 00 (top left side) to 23 (bottom right side); adapted from [100].

The mathematical expression for LG modes is as follows:

$$LG_{p,q}(r, \phi, z) = \sqrt{\frac{2p!}{\pi(p+|q|)!}} \frac{1}{w(z)} \left(\frac{\sqrt{2}r}{w(z)}\right)^{|q|} L_p^{|q|} \left(\frac{2r^2}{w(z)^2}\right)$$
$$\times \exp\left(-\frac{r^2}{w(z)^2}\right) \exp\left(-i\left(kz + \frac{kr^2}{2R(z)} - q\phi - (2p+|q|+1)\zeta(z)\right)\right)$$
$$(2.7)$$

where $L^{|q|}{}_p$ are the generalised Laguerre polynomials, $w(z)$ is the beam radius at position z, $R(z)$ is the radius of curvature of the beam's wavefronts, and $\zeta(z)$ is the Gouy phase shift z [101]; here $k = \frac{2\pi}{\lambda}$ is the wave number, with λ being the wavelength of the light.

LG modes are characterised by their circular symmetry and their intensity distribution, which features a central dark core surrounded by concentric rings. The phase structure of these modes includes a helical phase term that gives rise to an orbital angular momentum. The phase of a Laguerre-Gaussian mode includes several components: the plane wave phase $-kz$, representing propagation along the z-axis, a quadratic phase term $\frac{kr^2}{2R(z)}$, the azimuthal phase term $-q\phi$, and the Gouy phase shift $-(2p+|q|+1)\zeta(z)$. The azimuthal term $-q\phi$ is responsible for the helical phase structure and the associated orbital angular momentum of the LG modes. The Fig 2.5 represent the phase of these modes:
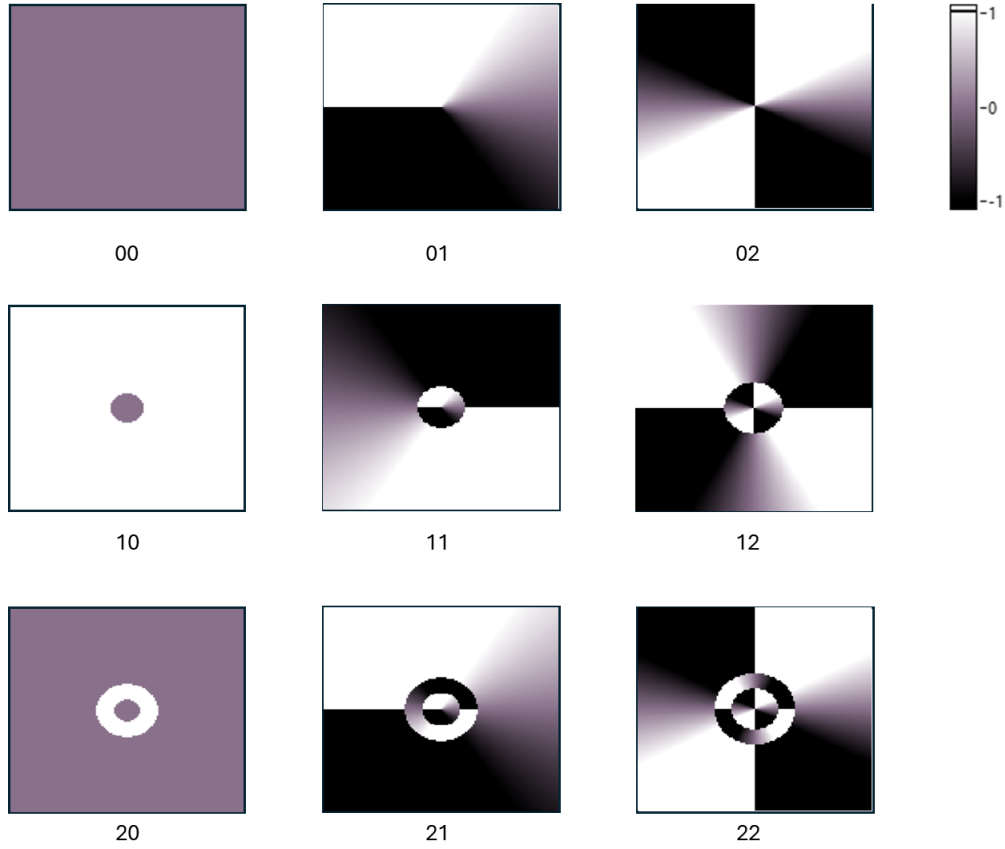
Figure 2.5: Phase distribution of LG modes from 00 (top left side) to 23 (bottom right side); adapted from [100].

The amplitude distribution of the LG mode is described by the product of a Gaussian envelope and the generalised Laguerre polynomials. The Gaussian envelope defines the overall shape of the beam, while the Laguerre polynomials introduce radial nodes in the intensity distribution. The intensity $I_{(pq)}(r, \phi, z)$ of the beam is given by the square of the absolute value of the electric field as for the HG modes:

$$I_{pq}(r, \phi, z) = |E_{pq}(r, \phi, z)|^2 \tag{2.8}$$

for the fundamental mode, LG_{00} the intensity distribution is purely Gaussian:

$$I_{00}(r, \phi, z) = |E_0|^2 \frac{1}{w(z)^2} exp(-\frac{2r^2}{w(z)^2}) \qquad (2.9)$$

For higher-order modes, the intensity distribution will include the Laguerre polynomials, which introduce additional structure such as rings and azimuthal phase variations in the transverse plane [102]. These modes can be generated using various optical devices, including spatial light modulators, spiral phase plates, and cylindrical lenses. These devices facilitate precise control over the phase and amplitude of light to achieve the desired LG mode shape. Additionally, LG lasers can be designed with specially constructed laser cavities to promote the generation of coherent LG modes [104].

2.4.3   Laguerre-polynomial (LP) modes

The LP modes are a fundamental component of Laguerre-Gaussian modes and are essential for their description. These modes are described by associated Laguerre polynomials, denoted as $L_p^{|p|}$ where p represents an integer. These polynomials determine the radial profile of LG modes and play a crucial role in shaping the intensity distribution of these modes[105].

2.4.4   Key differences between LP, HG and LG modes

The major differences between these modes can be classified in 4 groups:

- Shape of Intensity Distribution: The most conspicuous dissimilarity lies in the shape of the intensity distribution. HG modes exhibit a Gaussian bell-shaped intensity profile, while LG modes display concentric rings of varying intensity. LP modes, represented by associated Laguerre polynomials, determine the radial intensity profile of LG modes.

- Quantum Numbers: HG modes are described by two integer quantum numbers, n

and m corresponding to the number of nodes along the x and y axes, respectively. LG modes are described by two integer quantum numbers, p and q corresponding to the number of concentric rings and the number of nodes along the z-axis, respectively. LP modes, represented by associated Laguerre polynomials, contribute to the radial profile of LG modes. There is an equation able to bind n, m with p and q [106]:

$$q = m - n \tag{2.10}$$

$$p = min(m, n) \tag{2.11}$$

- Symmetry: HG modes possess symmetry about both the x and y axes, while LG modes exhibit annular symmetry, with no specific axis of symmetry. LP modes, through associated Laguerre polynomials, contribute to the azimuthal symmetry of LG modes.

- Orbital Angular Momentum (OAM): A pivotal distinction lies in the OAM associated with LG modes, quantized as p. This OAM arises from the phase spiral in LG modes and is absent in HG modes. LP modes, represented by associated Laguerre polynomials, contribute to the OAM and azimuthal characteristics of LG modes [107]. The OAM mode will be explained in detail in the following paragraph.

2.4.5   Orbital angular momentum of light

Starting from the XVI century with Kepler's studies on comets, the mechanical properties of light began to be studied. Initially it was thought that light carried linear momentum. With the studies of Poyinting and Einstein at the beginning of the last century, the quantum nature of light was understood with a substantial change in the method of describing and understanding light, from ray theory to the theory of electromagnetic waves. An important breakthrough in understanding the behaviourof the photons that

make up light came in 1992 with Allen's study, which, for the first time, combined the concept of OAM with the idea of optical vortex [108]. In this work the authors recognized that a light ray having an azimuthal phase dependence of exp(-i$q\phi$) can carry an orbital angular momentum that is totally independent with respect to polarisation and can have a value of L=$q\hbar$. An electromagnetic wave can carry both a spin and an orbital momentum, the spin angular momentum (SAM) is associated with the circular polarisation of light, representing the intrinsic angular momentum due to the circular polarisation state. SAM is quantized in units of $\hbar$ (Planck's constant divided by 2π), corresponding to right-hand (clockwise) and left-hand (counterclockwise) circular polarisations. The wavefront of light with SAM is typically flat or spherical without helical structures. SAM affects only the polarisation state of the light without changing the spatial distribution of the beam [109][110]. Orbital Angular Momentum (OAM) is associated with the helical wavefront of a light beam and refers to the angular momentum carried by the beam due to its spatially structured wavefront. Unlike spin angular momentum OAM can have a discrete range of values and is proportional to the winding number of the helical wavefront. Each OAM mode is characterised by a unique value of the topological charge, which represents the number of twists the light does in a single wavefront; as the number of twists increases, the speed at which the light rotates around the axis also increases. The wavefront of light with OAM is helical, creating a corkscrew-like structure [111]. The image below (Fig. 2.6) shows a representation of SAM and OAM:
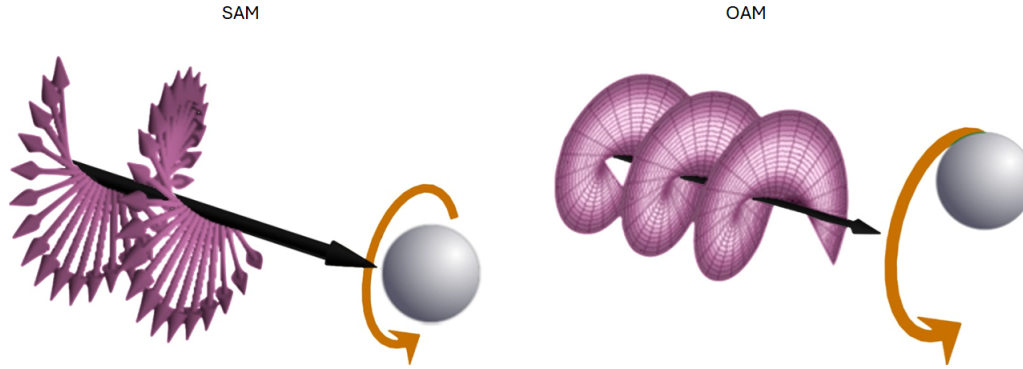
Figure 2.6: SAM: a beam of light with circular polarisation showing the rotation of the electric field vector; OAM: a beam of light with a helical phase front, showing the twisted wavefront and characteristic doughnut-shaped intensity profile.

The mathematical framework of Orbital Angular Momentum (OAM) starts with the general expression for the orbital angular momentum vector **L** , which is given by:

$$L = rxp \tag{2.12}$$

where **L** is the orbital angular momentum vector, **r** is the position vector and **p** is the linear momentum vector [108]. For a light beam described by a complex field E(**r**), if the beam has an azimuthal phase dependence, it can be represented by a phase factor exp(iqϕ). Here, ϕ is the azimuthal angle, and q is an integer known as the topological charge or winding number, which is directly related to the OAM. The z-component of the orbital angular momentum, which corresponds to the rotational symmetry around the propagation axis, can be derived as:

$$L_z = -i\hbar \frac{\vartheta}{\vartheta \phi} \tag{2.13}$$

When this operator acts on a mode with azimuthal dependence exp($iq\phi$), it yields:

$$L_z exp(iq\phi) = q\hbar exp(iq\phi) \tag{2.14}$$

This indicates that the beam carries an OAM of $q\hbar$ per photon along the z-axis. This quantization of OAM means that each photon in the beam possesses an orbital angular momentum proportional to the topological charge q.

The twist in the fibre introduces an additional phase term, modifying the effective propagation constant:

$$\beta_q = \beta_0 + \frac{q}{R_{twist}} \tag{2.15}$$

where β_0 is the propagation constant of the untwisted fibre and R_{twist} is the radius of the twist [112].

The intensity profile of an OAM mode is derived from the square of the absolute value of the electric field. For an OAM mode, the intensity distribution typically exhibits a doughnut-shaped profile with a central dark spot. This dark spot is due to the phase singularity at the centre of the beam where the intensity is zero. Mathematically, the intensity $I_{(pq)}(r, \phi, z)$ of the OAM mode is given by:

$$I_{pq}(r, \phi, z) = |E_{pq}(r, \phi, z)|^2 \tag{2.16}$$

For higher-order modes (q=0), the intensity profile becomes more complex, displaying a series of concentric rings. The number and size of these rings depend on the topological charge q and the radial index p. Key characteristics of the intensity profile include a central dark spot caused by the phase singularity where the phase is undefined and the intensity is zero, and a doughnut shape where the intensity peaks away from the centre, forming a ring-like structure. The phase profile of an OAM modes is characterised by an azimuthal phase term $\exp(iq\phi)$, where q is the topological charge or winding number; this term introduces a helical phase structure to the beam, which means the phase changes continuously around the beam's circumference. The helical nature of the phase front

results in the beam possessing OAM. The figure below (2.7) shows phase and intensity profile of different OAM mode:
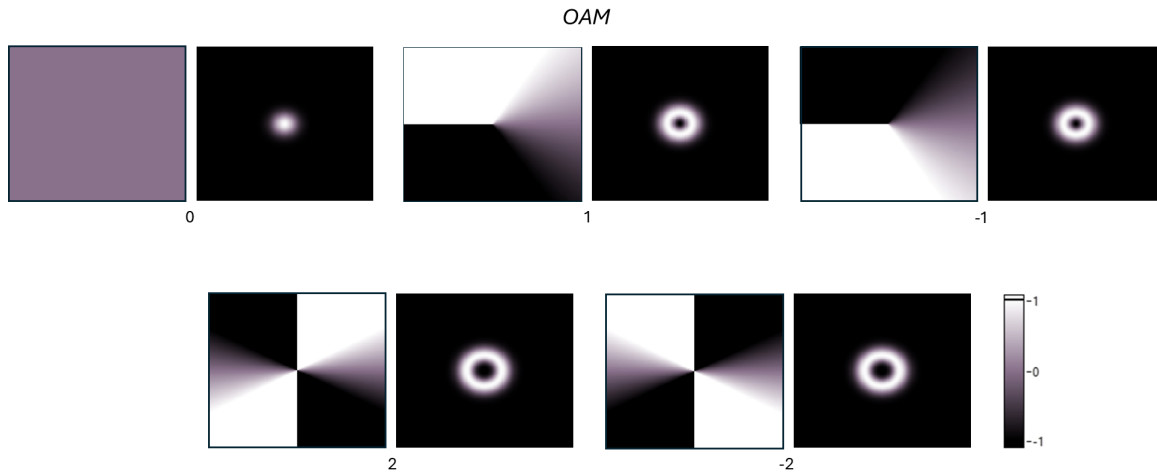
Figure 2.7: Representation created with LabVIEW of the phase and intensity of different OAM modes, from -2 to +2.

The visual representation of the phase profile shows the phase distribution for OAM modes with different topological charges; the helical nature of the phase front is evident in the twisted phase structure for non-zero q; while the intensity profile shows the distribution for OAM modes and the doughnut-shaped is clear for non-zero q.

To better understand how the wavefront behaves during propagation, one can refer to image 2.8, which depicts OAM 0, 1, and 2. The arrows indicate the direction of the rays, which are perpendicular to the wavefront. In the case of OAM different from 0, there is an azimuthal component of the Poynting vector, while for OAM $\neq 0$ the vectors are parallel [113].

OAM=0   OAM=1   OAM=2
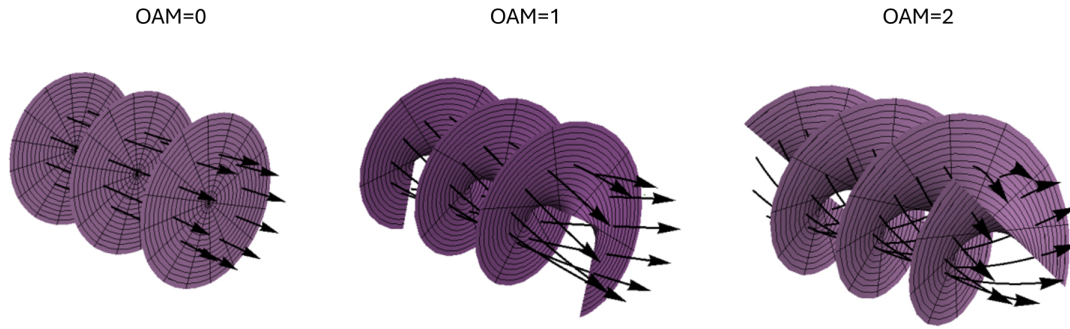
Figure 2.8: Representation of the phase and intensity of different OAM modes, from 0 to +2; the arrows indicate the direction of the rays, which are perpendicular to the wavefront.

Optical fibres can support the propagation of OAM modes even though they are rotationally symmetric. This is achieved through the design and fabrication of twisted optical fibres. The twist in the fibre can introduce a helical structure to the refractive index profile, which supports the propagation of modes with helical wavefronts. These twisted fibres can be designed to maintain the OAM modes over long distances, enabling applications in communication and quantum information [112].

Over the years various methods have been developed to create and analyse the OAM. In this work two types were used, the first more classic, the SLM and explained above (see section 2.5.1) while the latter involves the development of metasurfaces (see chapter 4 for a complete overview). The OAM is applied in various fileds such as optical communication where can be used to increase transmission capacity through OAM mode multiplexing, allowing the simultaneous transmission of multiple channels of information over a single optical fibre (the concept of multiplexing will be explain in the following section of this chapter) [112]. In quantum information is possible to entangle the OAM modes to transmit information securely and with high dimensionality [114]. In microscopy, OAM modes are used to enhance the resolution and contrast of images. The helical wavefronts of OAM modes can interact with microscopic structures in unique ways, providing advanced imaging capabilities [115].

2.5 Mode sorter

Mode sorters play a crucial role in optical systems as they are designed to analyse and break down any optical field into a comprehensive set of orthogonal modes. Currently, there is a notable gap in commercially available mode sorters capable of reliably transforming HG modes into LG modes, and addressing this gap is the primary focus of the ongoing research [64][116].

To illustrate the concept of a mode sorter, a classic and straightforward example is that of a converging lens. In this scenario, the converging lens serves as a practical "separator" by distributing the different components of light passing through an optical fibre across distinct positions in the lens's focal plane [117]. In essence, the converging lens organises the various elements of light into specific spatial positions.

The design of a mode sorter involves a series of optical elements that manipulate the phase and amplitude of incoming light to separate different spatial modes. One of the advanced methods for creating a mode sorter is the Multi-Plane Light Conversion (MPLC) technique. This technique uses multiple phase masks or diffractive optical elements arranged in a sequence to achieve the desired mode sorting. This is the core of this work and will be explained in detail in Chapter 4, but different kinds of mode sorters will be explained in the following subsection.

2.5.1 Kind of mode sorters

There are different kinds of mode sorters, each with unique methods of operation and application. Here are some examples to provide a general overview of how they work, can be used, and are created.

- ***Converging lens***: these lenses can spatially separate different components of an optical field into distinct positions within the lens's focal plane. Light from an

optical fibre, containing multiple spatial modes, passes through the lens, which then focuses each mode to a unique point based on its specific phase and amplitude profile. This process enables the spatial separation of modes, providing a practical and straightforward method for organizing optical fields [118] An example of how these lenses work is shown in Fig.2.9.
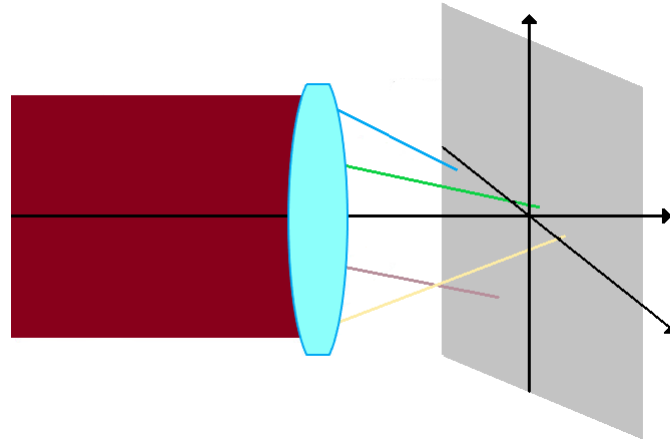
Figure 2.9: Illustration demonstrating how a converging lens sorts different spatial modes; each line corresponds to a different mode of light that is sorted in a different place on the cartesian axes.

- **OAM mode sorter**: the mode sorter can convert the OAM modes into a set of spatially separated spots on a detection plane, facilitating the identification and analysis of each mode. This technique leverages the unique phase characteristics of OAM modes to achieve high-dimensional multiplexing in optical systems [118].
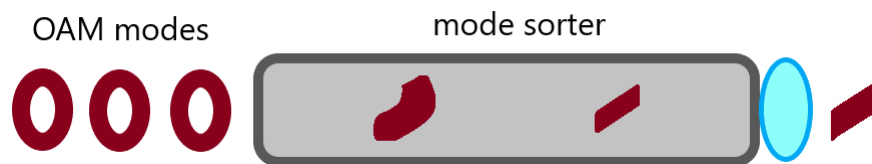
Figure 2.10: Illustration demonstrating how an OAM mode sorter can sort different spatial modes.

- **Spatial light modulator (SLM)**: is an optoelectronic device that dynamically

manipulates light waves by modifying the phase, amplitude, or polarisation of light across a two-dimensional surface. It functions as a reconfigurable "mask" that shapes and controls light in real-time (2.11).
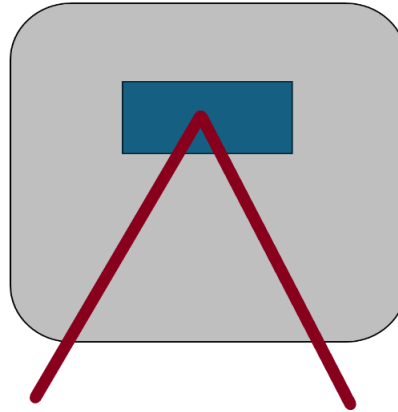
Figure 2.11: Illustration of a liquid crystal SLM; the blue part represents the liquid crystal, the red lines are the light beam that hit the SLM.

It is a planar optical element with controllable intensity transmittance τ(x,y), where the transmitted light intensity (I0) is related to the incident light intensity (I_1) by:

$$I_0 = I_1(x, y)\tau(x, y) \tag{2.17}$$

The image τ(x,y) is imparted to the transmitted light, similar to how a slide projector reads an image on a transparency. If the incident light is uniform, the transmitted light intensity is proportional to τ(x,y). The basic operation of an SLM involves applying an electric field or voltage, altering its optical properties. There are several types of SLMs, including liquid crystal displays (LCD) and micro-electromechanical systems (MEMS) based devices, for example the digital micromirror devices (DMD). SLMs are valuable tools in various fields of optics and photonics, enabling the generation of complex optical wavefronts, adaptive optics correction, holographic displays, optical trapping, and spatial light modulation for applications ranging from imaging

and microscopy to optical communications and optical data processing. Notably, $\tau(x,y)$ can modulate both intensity and phase, providing comprehensive control over light fields [119].

- ***Fibre bragg grating (FBG)***: is an advanced optical device composed of a microstructure (Fig. 2.12), typically a few millimetres in length, embedded within the core of a standard single-mode fibre. One way to create this microstructure is by photo-inscribing the fibre using a UV laser beam in conjunction with a phase mask to generate an interference pattern; this process induces a permanent change in the physical properties of the silica matrix of the fibre core. The Bragg wavelength is dictated by the periodicity of the grating's microstructure and the refractive index of the fibre's core. Due to its symmetrical nature, the FBG consistently reflects light at the Bragg wavelength, irrespective of the light's direction of incidence.
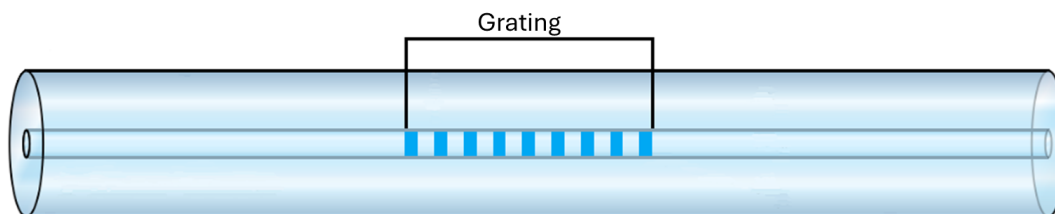
Figure 2.12: Illustration of the microstructures comprising the FBG.

This technology effectively functions as a wavelength-specific mirror, serving as a narrowband filter. When light containing a broad spectrum of wavelengths enters the optical fibre, only the light within a narrow range centered around the Bragg wavelength is reflected by the grating. The rest of the light passes through unaffected [120]. The Bragg wavelength (λ_B) is mathematically defined by the equation:

$$\lambda_B = 2n_{eff}\Lambda \tag{2.18}$$

when n_{eff} is the effective refractive index of the core and Λ is the grating period

[121]. These gratings offer several advantages, including low attenuation over long distances, immunity to electromagnetic and radiofrequency interference, compact size, low weight, and safe operation in explosive environments due to their intrinsic safety. Additionally, they exhibit high sensitivity and long-term reliability. However, there are also drawbacks, such as high manufacturing costs, significant sensitivity to temperature and strain, and a limited operational wavelength range [122].

2.6 $4f$ system

The name "$4f$" refers to the two lenses placed in a back-to-back configuration, with a focal length equal to f, hence forming a doublet.

In the $4f$ optical system, light from the input plane is focused by the first lens onto the Fourier plane, where the Fourier transform of the input signal is obtained. The Fourier plane acts as a frequency domain representation of the input signal. After the Fourier plane, the light passes through a processing element, which can be a filter, a SLM, or other optical components used for specific applications. The processing element modifies the Fourier transform of the input signal according to the desired operation [123].

In the $4f$ system, the input image is placed at the input plane. The first lens performs a Fourier transform on the image, transforming it from the spatial domain into the frequency domain and projecting it onto the Fourier plane. This separates the image's details into a pattern of light and dark spots, categorasing them by big smooth areas (low frequencies) and tiny sharp details (high frequencies) (Fig. 2.13) [117].
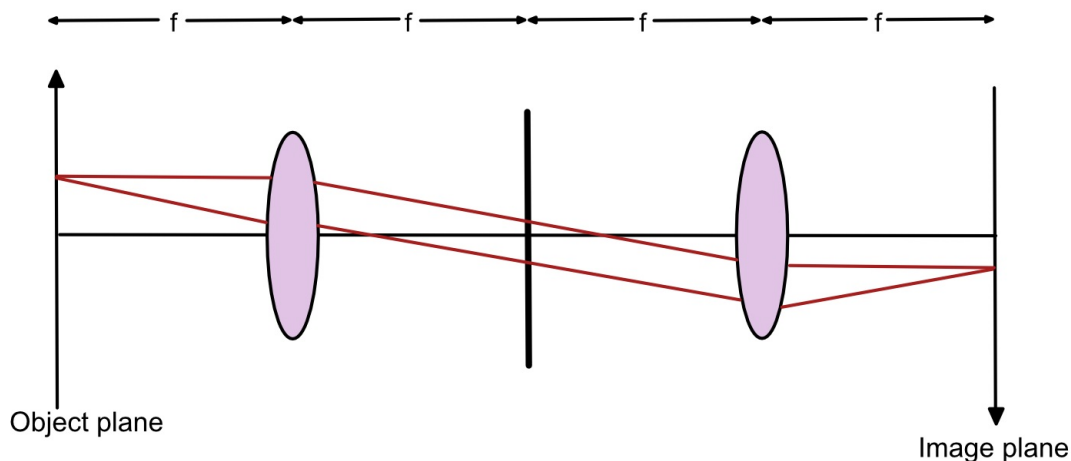
Figure 2.13: Schematic representation of a $4f$ system.

At the Fourier plane, different types of filters can be applied. A low-pass filter allows low-frequency components (big, smooth areas) to pass through while blocking high-frequency components (tiny, sharp details), resulting in a smoothed image that reduces noise and fine details. Conversely, a high-pass filter allows high-frequency components (tiny, sharp details) to pass through while blocking low-frequency components (big, smooth areas), enhancing edges and fine details. A band-pass filter allows a specific range of frequencies to pass through while blocking others, isolating specific features of the image.

The second lens then performs an inverse Fourier transform on the filtered frequency components, converting the modified frequency domain back into the spatial domain and reassembling the sorted details into a cleaned-up version of the original image. The final result, seen at the output plane, is a new image where unwanted details (like noise) are removed, or certain features (like edges) are enhanced, depending on the filter used.

The 4f optical system offers several advantages. It enables the separation of spatial and spectral information, making it useful for various imaging and spectral analysis applications. Additionally, it provides a stable and flexible platform for performing different optical operations and transformations.

Overall, the 4f optical system provides a versatile platform for optical processing and manipulation of signals, making it a valuable tool in many areas of optics and photonics. In this work all the optical set up present this system as a fundamental part.

2.7 How to approach the fabrication of a metasurface

Two primary approaches have been employed thus far in the field of metasurface engineering: the top-down and bottom-up methods. Both of these approaches lead to the creation of the desired metasurface but follow distinct initial procedures.

These approaches are depicted in the figure 2.14:
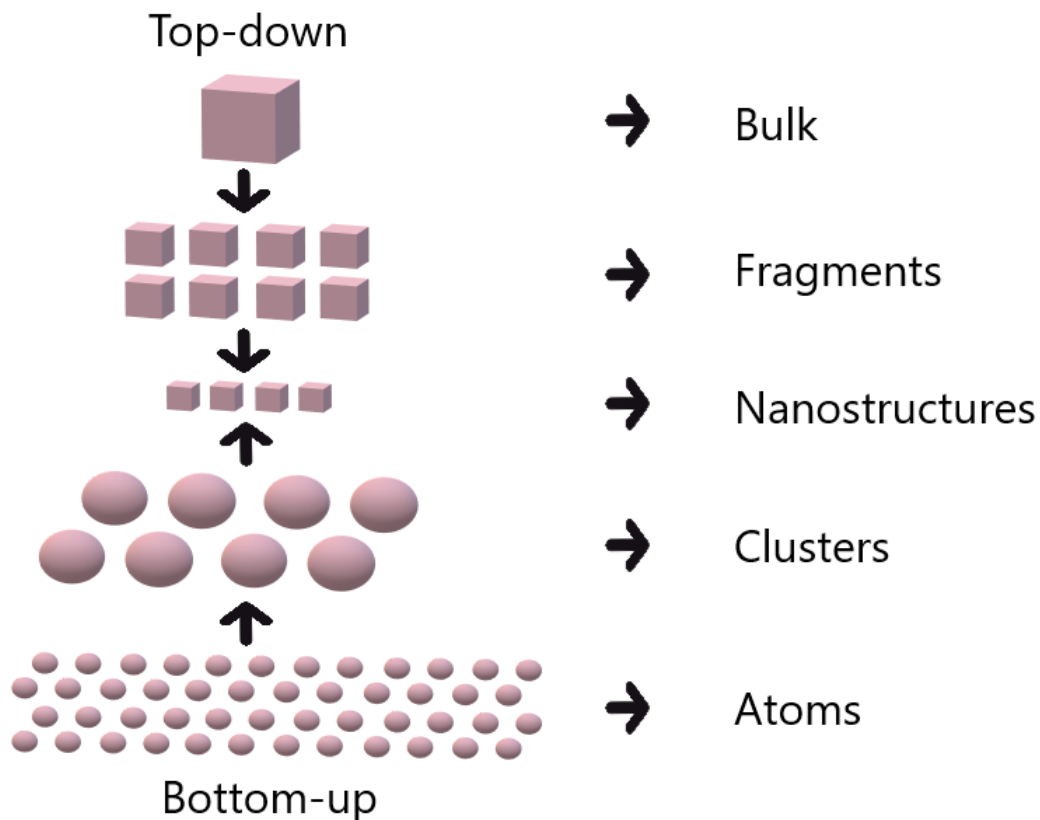
Figure 2.14: Schematic representation of the top-down and bottom-up ap- proaches for the fabrication of metasurfaces.

The top-down approach commences with "larger" materials, systematically refining them into progressively smaller fractions, culminating in the attainment of the desired shapes and dimensions. In contrast, the bottom-up approach takes the opposite route, starting with individual atoms that are meticulously assembled through a series of processes until the final product is realised. One notable distinction between the two approaches is the equipment and speed of production. Bottom-up approaches do not require highly expensive equipment and can rapidly produce nanoparticles. The top-down approach requires advanced tools to systematically reduce larger materials into smaller, precise structures. Electron Beam Lithography (EBL) is used for creating highly detailed and precise nanoscale patterns. It involves a scanning electron microscope (SEM) combined with a lithography system [124]. Photolithography transfers patterns from a mask to a substrate using light exposure. It needs a photolithography mask, mask aligner, and ultraviolet (UV) light exposure system [125]. Focused Ion Beam (FIB) Milling sculpts or modifies surfaces at the nanoscale. It involves a FIB system that uses a focused ion beam to ablate material from the substrate [126]. Etching processes are used for removing unwanted materials using dry or wet etching. The bottom-up approach relies on assembling atoms and molecules to form complex structures. Chemical Vapor Deposition (CVD) grows thin films from gas-phase precursors through chemical reactions. It involves a CVD reactor chamber, gas flow control systems, and temperature control [127]. Molecular Self-Assembly organises molecules into ordered structures using techniques like solution deposition where molecules self-assemble on a substrate [128]. Layer-by-Layer Assembly constructs nanostructures layer by layer, involving immersion or spray deposition equipment and environmental control for the deposition process [129]. However, the top-down approach offers meticulous control over metasurface design, rendering it particularly well-suited for crafting intricate structures with specific optical properties. Nonetheless, it

often necessitates the use of costly and intricate equipment, such as electron-beam lithography. The bottom-up approach offers scalability and the ability to assemble metasurfaces from the ground up, presenting opportunities in the fields of nanophotonics and materials science. Meanwhile, the top-down approach excels in providing precise control over metasurface design for creating intricate structures with specific optical properties [130]. For this work, since high precision and resolution and a specific arrangement of elements (pattern) on the metasurface were required, the top-down electron-beam lithography method was chosen due to its characteristic and good reproducibility, the full protocol and how this approach was use will be explain in the next two chapters (3 and 4).

2.8 Etching's techniques

The Reactive Ion Etching (RIE) is a technique that uses plasma, starting from gases, to react and "eat" a certain amount of material from a substrate. This process is fundamental in microfabrication because it allows for precise control over etch profiles, making it possible to create intricate patterns and structures essential for electronic devices. The two primary etching techniques are isotropic etching and anisotropic etching (Fig. 2.15) [131].
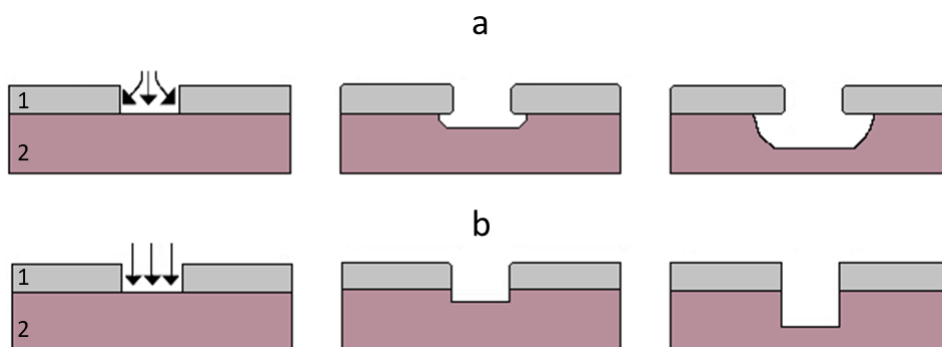
Figure 2.15: Comparison of two different kind of etching. a) result of the isotropic etching. b) result of anisotropic etching.In both images: 1 represent the mask, 2 functional material.

Isotropic etching removes material uniformly in all directions, meaning the etch rate is the same horizontally and vertically. This technique typically uses chemical etchants that react with the material on the substrate. Because the etching occurs equally in all directions, isotropic etching results in rounded or undercut profiles beneath the mask, as the material is removed laterally as well as vertically. Isotropic etching is commonly used in situations where precise control of the sidewall profile is not critical or where some undercutting is acceptable. An example of isotropic etching is wet chemical etching using solutions like hydrofluoric acid (HF) for silicon [132][133]. In contrast, anisotropic etching removes material preferentially in one direction, usually vertically. This results in a highly directional etch with vertical sidewalls and minimal lateral etching. Anisotropic etching is essential for applications requiring precise control of the etched feature's shape and dimensions. Reactive Ion Etching (RIE) and Deep Reactive Ion Etching (DRIE) are common techniques used to achieve anisotropic etching. In these processes, ion bombardment and controlled chemical reactions facilitate vertical etching while minimising lateral etching [134]. In this work two different Inductively Coupled Plasma (ICP) reactor had been used to obtain an anisotropic etch instead of an isotropic etch; for more details see Chapter 3 and 4.

2.9   Lithography techniques overview

When it comes to lithography, various techniques can be employed, each suitable for different applications. In this summary, some of the most commonly used methods are considered: Electron Beam Lithography (EBL), Nanoimprint Lithography (NIL) and Extreme Ultraviolet Lithography (EUV).

Electron Beam Lithography (EBL) involves the use of a focused beam of electrons to directly write patterns onto a resist-coated surface. This technique allows for extremely

high resolution, with feature sizes as small as sub-10 nm achievable due to the short wavelength of electrons. EBL is especially valued in research and prototyping, where intricate and custom patterns can be created without the need for masks. Despite its advantages, EBL is characterised by low throughput, as patterns are written point by point, and it incurs high costs for equipment and maintenance, making it less ideal for large-scale production [135].

Nanoimprint Lithography (NIL) Nanoimprint Lithography (NIL) is carried out by pressing a mould with nanoscale features into a thin resist layer on a substrate. This resist is then cured using heat or UV light, and the mould is removed, leaving behind a replicated pattern. NIL is noted for its high throughput and cost-effectiveness in mass production because it can process patterns in parallel over large areas. However, the creation of the initial mould is both complex and expensive, and any defects in the mould can be transferred to all subsequent imprints, leading to potential high defect rates in large-scale manufacturing [136].

Extreme Ultraviolet Lithography (EUV) uses extreme ultraviolet light with a wavelength around 13.5 nm to produce very small features on semiconductor wafers. This technique is crucial for manufacturing the latest generation of microchips, offering scalability for high-volume semiconductor production. Nevertheless, the equipment and infrastructure required for EUV are extremely expensive and complex, requiring sophisticated handling and extensive maintenance, which limits its use primarily to high-end semiconductor manufacturing [135]. For this project the EBL was chosen over other lithography techniques for several compelling reasons. Firstly, EBL equipment was already available in our facility, making it a practical and cost-effective option compared to NIL and EUVnm . Additionally, the complexity and high cost associated with creating the initial mould for NIL presented a significant obstacle. Given that the project aimed to produce a physical MPLC for the first time, there was considerable uncertainty about whether the physical

device would match the simulation results. This uncertainty made the investment in NIL moulds impractical, especially if design changes were required after initial tests. The flexibility of EBL in allowing direct pattern writing on substrates was another critical factor. This capability enabled easy modifications to designs and protocols based on experimental findings. If adjustments in the arrangement of structures on the metasurface were needed, EBL could accommodate these changes quickly and efficiently without the need to create new moulds, as would be required with NIL. Therefore, EBL was preferred for its immediate availability, adaptability to rapid design changes, and avoidance of the high costs and complexities associated with NIL mould fabrication. This made EBL the ideal choice for developing a dynamic and adaptable protocol for producing a physical MPLC, allowing for efficient adjustments based on experimental outcomes; for more detail about the EBL see section 3.9.

2.10   Machine learning

Machine Learning (ML) is a general term used to describe a set of techniques for interpreting data by comparing them to models of data behaviour. It is also a specific subset of artificial intelligence (AI) that trains computers on how to learn. In recent decades, ML has become a fundamental part of research and development practices in various fields, including finance, engineering, biology, and medicine. In order to make predictions or decisions "without being explicitly programmed" (Arthur Samuel, 1959), ML algorithms build models based on sample data (training data). These algorithms can be supervised, unsupervised, or reinforcement-based [137].

- ***Supervised learning***: involves training a model on a labelleddataset, which means the data includes both input variables (features) and the corresponding output variables (labels). During the training process, the model is trained using a dataset

where each example is paired with the correct output, and once trained, the model is used to predict outputs for new, unseen inputs. Common algorithms in supervised learning include linear regression, logistic regression, decision trees, support vector machines (SVM), and neural networks. This approach is used for tasks such as classification, where the goal is to predict a category and regression, where the goal is to predict a continuous value.

- ***Unsupervised learning***: involves training a model on a dataset without labelledresponses. The model tries to learn the underlying structure of the data. This process includes clustering, where the data is grouped into clusters based on similarity, and association, where relationships or associations between different data points are identified. Common algorithms in unsupervised learning include K-means clustering, hierarchical clustering, principal component analysis (PCA), and association rule learning.

- ***Reinforcement learning***: involves training a model to make a sequence of decisions by rewarding it for correct decisions and penalising it for incorrect ones. The model learns to maximise the cumulative reward over time. The reinforcement learning process includes an agent, which is the learner or decision-maker, interacting with the environment, which is the world with which the agent interacts. The agent takes actions, which are the set of all possible moves it can make, and receives rewards, which are feedback from the environment based on the agent's actions.

Feature	Supervised learning	Unsupervised learning	Reinforcement learning
Data	Labelled data	Unlabelled data	Interaction data (states, actions, rewards)
Goal	Predict output for new data	Find hidden patterns or intrinsic structure	maximise cumulative reward
Use Cases	Classification, regression	clustering, dimensionality reduction	game playing, robotics

Table 2.1: Comparison of Supervised learning, unsupervised learning, and reinforcement learning.

2.10.1 Convolutional Neural Networks (CNNs) and support vector machine (SVM)

For this thesis, various algorithms were employed depending on the specific experiments being conducted. Initially, the data obtained in the form of images were analyse d using Convolutional Neural Networks (CNNs). Subsequently, the data were transformed into numerical matrices and then analysed through classification and regression algorithms. In the appendices, the results of all experiments conducted with the different algorithms are presented, while Chapters 5 and 6 specifically report the results obtained with the Support Vector Machine (SVM) classification algorithm.

The choice to use a classification algorithm rather than a regression algorithm was influenced by the objective of these experiments, which was to evaluate the algorithm's effectiveness in correctly classifying the data into their respective categories. This focus on classification was essential for assessing the algorithm's predictive capability in assigning the correct class membership to the data.

These concepts will be explained in greater detail in Chapters 5 and 6, as previously mentioned. Below, a more detailed explanation of the two primary types of algorithms

used in the experiments, Convolutional Neural Networks (CNNs) and Support Vector Machines (SVMs), is provided. The **CNN** is a class of deep learning, in particular deep neural networks, widely used to analyse images [138]. The major difference between a classical neural network and deep neural networks is in the complexity of the algorithm itself. A neural network is considered "shallow" if it has at most two hidden layers in its structure, whereas deep learning networks have multiple layers, allowing them to capture more intricate patterns in data [139]. The basic structure of a CNN comprises several types of layers: convolutional layers, pooling layers, and fully connected layers, each playing a specific role in the network's operation [140]. Convolutional layers serve as the core building blocks of a CNN. These layers perform convolution operations on the input data using kernels (filters) to detect various features in the images, such as edges, textures, and patterns. The result of this process is a feature map that emphasises the presence of specific features in different regions of the input data [141]. Pooling layers are used to reduce the spatial dimensions (width and height) of the feature maps, which helps decrease the computational load and the number of parameters in the network, thus making the model more efficient. The most common type of pooling is max pooling, which selects the maximum value from each patch of the feature map [142]. Fully connected layers, typically placed at the end of the network, are used to perform the final classification or regression tasks. In these layers, each neuron is connected to every neuron in the previous layer, enabling the network to learn complex representations of the data. The final output layer in a CNN often employs a softmax activation function for classification tasks, providing a probability distribution over the classes [139]. To better understand the distinction between classical neural networks and deep neural networks, consider the Fig. 2.16:
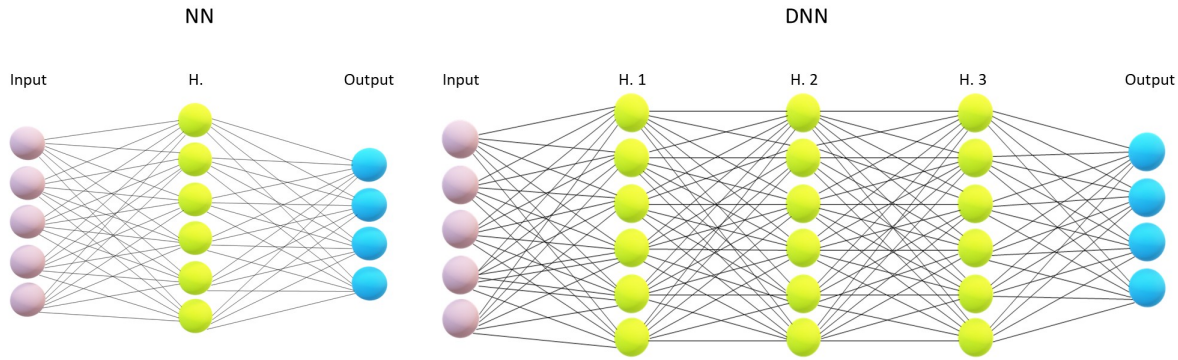
Figure 2.16: Illustration of a classical neural network with a single hidden layer on the left and a deep neural network with multiple hidden layers on the right. As seen, the deeper network can capture more complex patterns due to its layered structure.

SVMs, introduced by Vladimir Vapnik in 1963 [143], are robust supervised machine learning algorithms primarily used for classification. SVMs work by identifying the hyperplane that best separates data points of two classes in a high-dimensional space. This separation maximises the margin, which is the distance between the hyperplane and the closest data points from each class, known as support vectors [144]. Typically, the dataset is split into a training set and a test set, often in an 8:2 or 7:3 ratio. The training set is used to train the SVM model, where data points are mapped into a high-dimensional space, and the SVM algorithm finds the hyperplane that maximises the margin between classes [145]. When new data points are introduced, the SVM predicts their class based on their position relative to this hyperplane, allowing for precise classification [146]. One of the most significant advantages of SVMs is their ability to handle non-linear separable data through the use of kernel functions. This capability, known as the kernel trick, allows the SVM to implicitly transform the input data into a higher-dimensional space where a linear separation is possible, without explicitly computing the coordinates in that space. This transformation is computationally efficient and enables the SVM to handle complex datasets with non-linear boundaries effectively. Common kernels used in SVMs include the linear kernel, polynomial kernel, and radial basis function (RBF) kernel [143].

Chapter 3

Fabrication method and optimisation

3.1 Introduction

This chapter aims to explain the processes and tools necessary for the clean room manufacturing of the MPLC of interest and the parameters used for each tool while the actual protocols will be explained in the next chapter together with the results obtained. All images representing the diagrams of the instruments used were made using the software Affinity Designer2 based on the instrument manuals present in the JWNC.

3.2 Softwares used to design the patterns

For this project, two separate software were used for the design and drawing of the masks to be used. The first to have been used is L-edit; this is a microelectronic device design and layout software specialised in the creation of electronic diagrams and the physical arrangement of components on a substrate, it is a software that requires a specific licence and the resulting files are in GDSII (Graphic Data System) format.

The second software used is Klayout, an open-source programme able to create a file for reading from the EBPG. This software can convert a python script into an OASIS

(Open Artwork System Interchange Standard) file format and is user friendlier compare to other software like L-Edit. The OASIS format is preferred due to its ability to reduce file size compared to GDSII. Once the file is created in the appropriate format, GDSII for L-Edit and OASIS for Klayout, it will be worked in the same way: the layout is then processed using the JWNC's Beamer Software (a Windows terminal), which extracted features of the patterns, can choose the best fracturing mode, the resolution, the beam step size and generated the GPF (Grant Agreement Preparation Forms) file. Then, the cjob, a graphical user interface, was utilised to export the lithography job by selecting the appropriate parameters (as shown in section 3.4 Table 3.1) such as the position of the pattern/patterns on the sample, the dose and the aperture of the beam. Finally, the Belle for EBPG software was employed to export the file to the EBPG tool for writing on the sample.

3.3   Device cleaning

This is a standard procedure to clean the substrate; the JGS2 Fused Silica substrate were cleaned ultrasonically in methanol, acetone, and isopropyl alcohol (IPA) for 5 minutes each and were dried with nitrogen gun (N_2) after their exposure to the solvent. Additionally, the substrate was subjected to an oxygen plasma cleaning process using a Gala Plasma Prep 5 Oxygen Barrel Asher for 3 minutes at a power of 150 W and a pressure of $3x10^{-1}$ mTorr.

3.4   Plasma enhanced chemical vapour deposition

It is a technique in which chemical substances in the gaseous state react with each other using plasma for the deposition of a thin film of dielectric or metallic material. To process the sample, using this instrument, the first thing is to place it inside the high

vacuum chamber in which the various gases of interest will flow at constant temperature and pressure (Fig. 3.1, diagram of the PECVD delta tool).
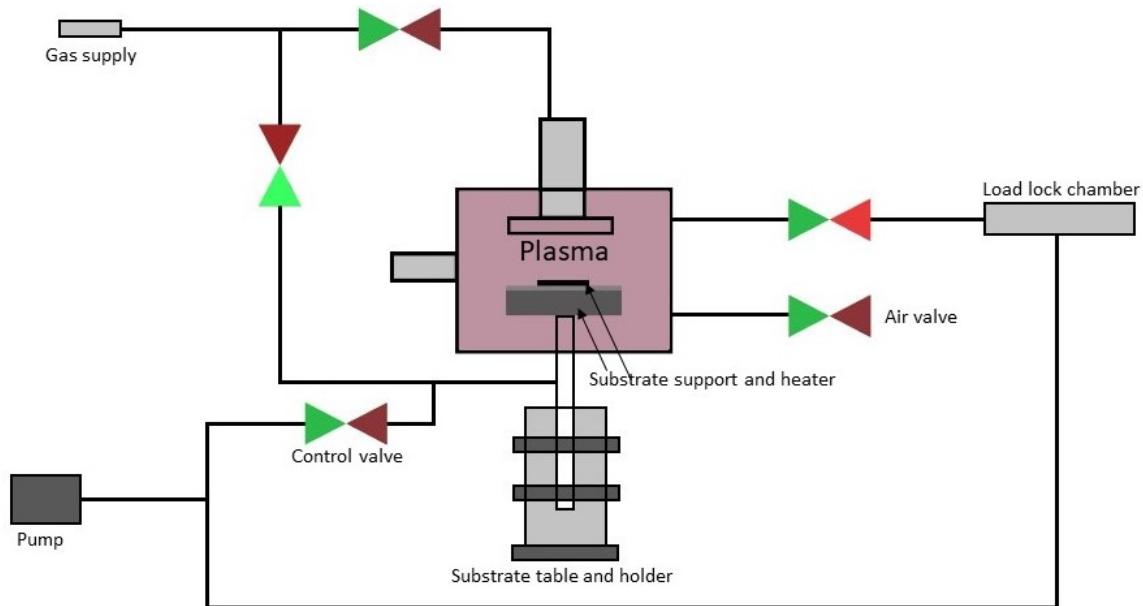
Figure 3.1: Diagram of the PECVD tool, lateral view. A tube containing Argon is placed centrally to the coil which is connected to an external power source; the plasma formed from noble gas is stuck in the tube and stream downward due to the flow of Ar. The deposition of the α-Si can now begin: the silane (SiH_4) is decomposed into SiH_x and H, subsequently the hydrogenated amorphous silicon (α-Si:H) starts to grow on the sample.

The electrons in the plasma move along an electromagnetic field and accumulate, forming a voltage bias, whose works task is to maintains the plasma and accelerates the ions between the vertical plates. The substrate table is brought to high temperature to help with the deposition process [147]. The entire process is made of 4 subprocesses that require different parameters. In this thesis the the ICP SPTS Delta Deep Tool was used to achieve the deposition of 800 nm of α-Si with the parameters shown in the following table (Table 3.1):

parametre	Step 1	Step 2	Step 3	Step 4
APC pre-position (%)	100	25	25	20
Ar (sccm)	0	0	1500	0
Electrode spacing (mm)	20	20	20	20
Gas stab time (sec)	5	5	5	5
HF RF load power (W)	5	5	5	5
N2 (sccm)	3500	0	0	1000
NO2 (sccm)	0	2000	0	0
Pressure (mTorr)	3000	2000	1000	800
SiH2 (sccm)	0	0	300	0
Time (sec)	30	180	410	10

Table 3.1: parameters used for the α-Si deposition.

3.5   Ellipsometer

This tool can measure the thickness and dielectric properties (refractive index, n, and extinction coefficient, k) of thin films on surfaces detecting the changes in the polarisation state of light after it reflects from a material's surface. Using some fitting algorithms is possible to understand the thickness of the film (in this particular case 800 nm of α-Si) [148]. In this work a J.A. Woollam Mark II Variable Angle Spectroscopic Ellipsometer was used.

3.6   Preparation of the negative resist

Hydrogen Silsesquioxane (HSQ) is characterised by its silicon-based structure with the approximate chemical formula $[\text{HSiO}_{3/2}]_n$. This structure comprises silicon (Si) atoms

bonded to oxygen (O) atoms, forming a cage-like network where each silicon atom is also

bonded to a hydrogen (H) atom as shown in Fig. 3.2.
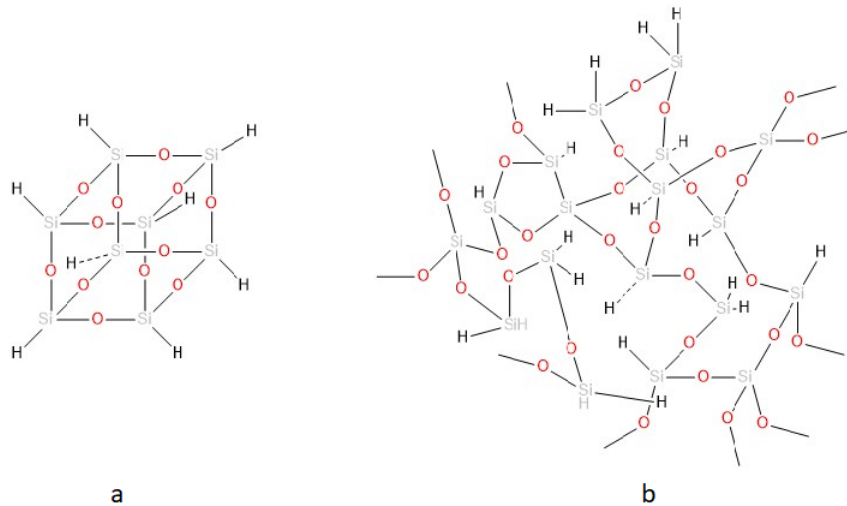
Figure 3.2: HSQ's transformation a) before lithography and b) after lithography. With the heat generated during the electron beam exposure in the lithography process, the structure of the bonds within the HSQ change arrangement.

This unique configuration allows HSQ to undergo significant chemical transformations during lithography. Before exposure to an electron beam, HSQ's network is relatively open, consisting of Si-H bonds which render it highly reactive and soluble. However, upon exposure to the electron beam, these Si-H bonds cross-link to form additional Si-O bonds, resulting in a denser and more rigid structure that becomes insoluble in developer solutions. This transformation is critical for creating stable, high-resolution patterns that can endure subsequent processing steps [149]. Proper handling and preparation of HSQ are essential to maintaining its performance. Typically, HSQ is stored at low temperatures, not exceeding 2 ^{0}C, to prevent degradation and maintain its chemical integrity. For preparing HSQ for spin coating, it is often diluted with Methyl Isobutyl Ketone (MIBK) to adjust its viscosity for a uniform thin film. A 2:1 (MIBK:HSQ) dilution ratio was used in this work, in particular 70 μl of MIBK were mixed with 35 μl of HSQ to ensure proper viscosity and film thickness. This mixture must be used immediately after removing HSQ

from refrigeration to prevent changes in viscosity due to temperature rise. After spin coating (2000 rpm), the substrate was baked at 90 ^{0}C for 5 minutes to further stabilise the film and prepare it for electron beam exposure. In electron-beam lithography (EBL), HSQ is exposed to a focused electron beam which induces cross-linking in the resist. This exposure makes the exposed areas less soluble, setting the stage for development where the unexposed, soluble parts are washed away, revealing a high-resolution pattern [150]. A significant factor influencing the quality of the patterns is the delay between exposure and development. Research suggests that delaying development, especially when the exposed samples are stored in a vacuum, enhances both contrast and sensitivity (Jones et al., 2018). Vacuum storage minimizes exposure to oxygen and moisture, which can otherwise react with HSQ and degrade its performance. This controlled environment helps maintain the chemical state of the resist, allowing for sharper and more defined patterning. The contrast, or the difference in solubility between exposed and unexposed regions, improves because the cross-linked network stabilises further during the delay. Similarly, sensitivity, which refers to the resist's response to the exposure dose, increases as the vacuum storage preserves the reactive state of the resist, making it more responsive to the developer [151].

3.7   Polystyrene sulfonic acid (PSSA) and Triton x100

After determining the negative resist to use, it was crucial to find a suitable development solution. Initially, a 20 nm layer of aluminium (Al) was used, but it was not possible to develop the sample consistently. Subsequently, Electra was used, which also yielded poor results. Finally, polystyrene sulfonic acid (PSSA) was employed, showing satisfactory results (for more details, see Chapter 4). The PSSA (Fig.3.3 a for the chemical structure) was chosen for its role as an effective intermediate layer between the

photoresist and the conductive layer. The selection of PSSA was driven by its high water solubility, which allows for easy application and removal. This property is particularly advantageous in processes requiring a clean removal without residues that could compromise the quality of subsequent layers [152]. In this context, PSSA was utilised to enhance adhesion between the photoresist and the conductive substrate while ensuring a smooth and defect-free surface. The concentration of PSSA at 4.5% was selected to achieve an optimal balance between viscosity and the ability to form thin, uniform films. Excessive concentration could lead to overly thick films that are difficult to control, whereas too low a concentration might result in insufficient coverage. To further improve the properties of the PSSA solution, 1% of Triton X-100, a nonionic surfactant, was added (Fig. 3.3b for the chemical structure). Triton X-100 plays a crucial role in reducing the surface tension of the solution, enhancing wettability, and ensuring uniform distribution of PSSA on the substrate. This helps prevent defects like drops or bubbles and ensures that PSSA spreads evenly across the surface, contributing to the overall quality of the intermediate layer [153].
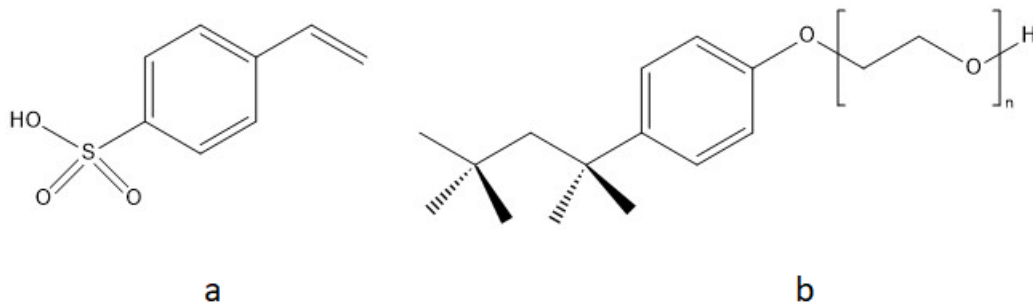
Figure 3.3: Chemical structure of PSSA (a) and Triton x100 (b).

3.8 Electron-beam physical metal evaporation

The EBPVD (Electron Beam Physical Vapour Deposition) process involves the precise and linear deposition of a metal onto a substrate. This is achieved by first loading the

sample into a load-lock chamber (Fig. 3.4a) that is maintained at high vacuum. An electron beam, generated at 9.7 kV, is then directed onto a metal target located in a lower chamber (Fig. 3.4b) through the use of a magnetic field. The electron beam causes the atoms from the target to vaporize, and these gaseous atoms then deposit onto the substrate as a thin film of the anode material. The process is monitored and controlled by measuring the evaporation rate and film thickness through the use of quartz crystal oscillation frequency detection. In this thesis were used the Plassys MEB 550S and the Plassys MEB 400S.
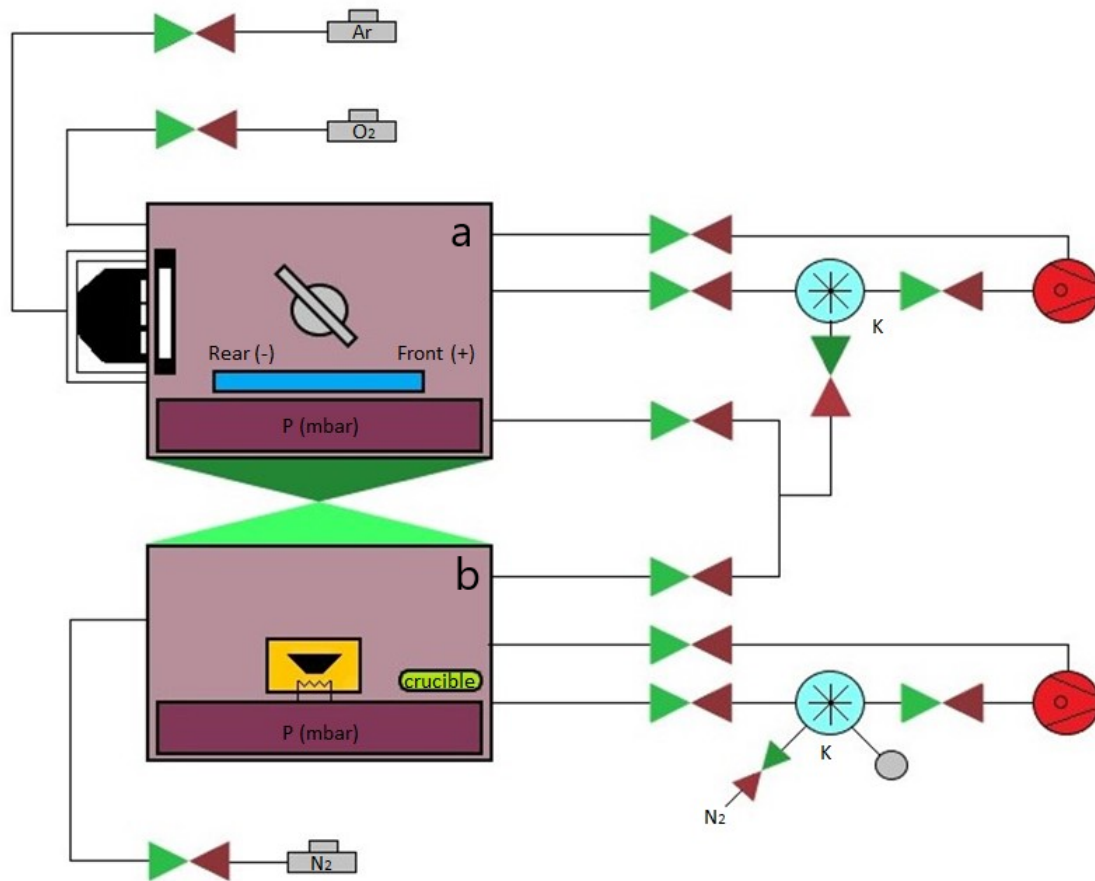
Figure 3.4: User interface of the evaporation process in the vacuum chamber.

This system comprises two main chambers and several gas circuits, including Argon,

Nitrogen, and Oxygen. The upper chamber (a) is designed to hold the sample that rotates continuously to ensure an even deposition of the thin film on the substrate. This chamber also features a pressure indicator to monitor internal conditions. In the lower chamber (b), crucibles contain various chemical compounds to be deposited, such as aluminium (Al). These compounds are heated and melted to be vaporized and deposited onto the substrate. When both chambers reach the same pressure (2×10^{-6} mbar) and the crucibles reach the operational temperature, the divider between the two chambers opens, allowing the vaporized material to transfer from the lower to the upper chamber. Pressure controls are also present in the lower chamber to ensure process stability. The system is equipped with a complex set of control valves, highlighted in green and red. The green valves indicate an open flow, while the red ones block the flow, allowing precise regulation of the gas amount entering the chambers. The gas flow is further managed by manometers (marked as "K"), which monitor pressure at key points within the system. The pumps, depicted as red circles, are critical for maintaining the necessary vacuum in the chambers. They remove excess gases, creating the low-pressure environment essential for the deposition processes. The system operation begins with preparation, where gases are introduced through control valves and pumps work to create a vacuum in the chambers. Once optimal conditions are achieved, the system starts the deposition process. This process is configured based on the chosen material and method and is executed by carefully controlling the pressure and gas flow to ensure that the deposited film is uniform and meets the desired specifications.

3.9 Electron Beam Pattern Generator

The electron beam lithography is one of the most useful tools used in the nano-fabrication process that can create nano-pattern by transferring the desiderated pattern onto the surface of a substrate [154]. A focused electron beam is scanned across a layer

made by electron-sensitive material, called resist, that covers the substrate; the resist changes its solubility properties according to the electron beam energy [155]. There are two kinds of resist: positive and negative. After the lithography process the area exposed (positive resist) or not exposed (negative resist) are removed by another step called development. There are several instruments suitable for lithography on the market, however they all have in common the main core formed by a high-voltage electron gun to produce the free electron, a series of lenses to concentrate the electron beam, various specific holders in terms of shape and size in which it is "loaded" the sample and a system of pumps to form the vacuum as well as a stage capable of moving the holders on the x and y axes. In Figure 3.5 is shown a schematic overview of the EBPG used for this work. Regarding this stage of device production, it's essential to determine the proper exposure dose of the sample, expressed in $\mu C/cm^2$. This is achieved through a "dose test", where multiple identical patterns are exposed to varying doses to determine the optimal one. If the dose is too high, the pattern will be oversized, and if it's too low, the pattern will be incomplete. However, the exposure does not depend exclusively on the dose but also on the scattering of the electrons that is created inside the tool and for this reason the sample is generally covered with a conductive layer to allow the dissipation of the electrons, otherwise there will be a pattern distortion. The exposure time is estimated by the product of the dose and the area of exposure divided by the electron beam current. The electron beam tool used for this work is the Raith EBPG 5200 that operate at 100 kV with the following parameters:

Parametre	Value
Resolution (μm)	0.01
Beam step size (μm)	0.03
Fracture mode	merge and step
Beam size FWHM (μm)	0.035
Dose (μC)	2000
Exposure time	2h 56min

Table 3.2: parameters used for the e-beam lithography.
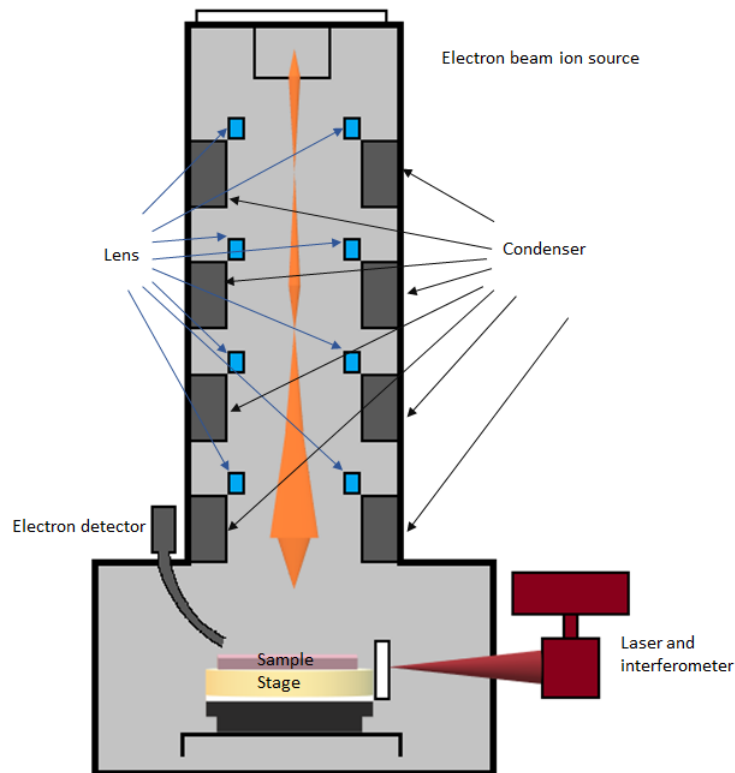
Figure 3.5: Schematic of e-beam lithography tool and vector scanning.The e-beam tool operates at high-vacuum. The electron gun generates an electron beam that is focused and deflected by a series of coils and lenses in the column. The stage can be moved between the chamber and loadlock. A laser interferometer system is used to measure and control the exact position of the stage, ensuring precise alignment and stability during the exposure process.

3.10   Strong acids, bases and respective PPE

For the correct manufacturing of this device it was necessary to use strong bases and acids. In particular, tetramethylammonium hydroxide (TMAH) was used for the development of the sample and hydrofluoric acid (HF) for the final removal of α-Si residues. For both of these chemical products it is necessary to use special PPE and be authorised after training, given the danger of these chemical products. As regards the PPE to be used they are:

- An additional pair of nitrile gloves: single use
- A pair of acid gloves: reusable after thorough washing, generally elbow-length
- A reinforced plastic apron: reusable and ankle-length
- One plastic apron: single use, to protect the other apron
- A plastic visor that covers face and neck

Both of these chemicals can have serious effects on health, including death, and the environment if they come into contact; the following image represents the chemical structure of these two products. If inhaled, TMAH can affect nerves and muscles, leading to breathing difficulties and muscle paralysis if inhaled/ingested, while it can cause chemical burns if in direct contact with skin and eyes. HF is corrosive to the eyes and skin but unlike TMAH its effects may not be immediate, as it attacks the nervous system, in particular it inhibits pain, at least initially, the bones and systemically the internal organs.
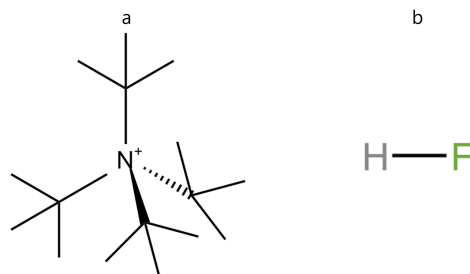
Figure 3.6: Lewis structure for the two chemical compounds: a) TMAH, b) HF.

3.11   ICP Estrelas 100

Its operation begins with system preparation, which is essential to ensure stable and optimal operating conditions. This includes checking the vacuum levels in the chambers, verifying the availability of necessary process gases, and ensuring all parameters are within operational limits. If required, the system may undergo preliminary conditioning, such as heating internal components to the working temperature to stabilise the process environment. Once the conditioning is complete the substrate is loaded into the load lock chamber (Fig. 3.7b); after loading, the chamber is sealed and the pumping process starts to reduce the pressure to a suitable vacuum level. This step is crucial to prepare the substrate for transfer to the main process chamber without introducing contaminants. Once the required vacuum is reached, the system's robotic arm transfers the sample from the load lock to the process chamber (Fig. 3.7a) under vacuum conditions, maintaining cleanliness and integrity. Inside the process chamber, the gases are selected and introduced through mass flow controllers (MFCs). The gases flow into the chamber following the specific etching recipe. The chamber pressure is then adjusted to the level required for plasma generation and etching. RF power is applied to the electrodes to ionize the process gases, creating a plasma field that consists of highly reactive ions and radicals that interact with the sample's surface. Throughout this phase, the process is monitored using the system's sensors and control displays to ensure all parameters, such as RF power, gas flow, and chamber pressure, are in accordance with the etching recipe. Material removal according to the desired pattern occurs during this stage (see table 3.3). Once the etch is complete, the RF power is turned off and the process gas flow is stopped. The robotic arm then transfers the substrate from the process chamber back to the load lock, again under vacuum conditions to maintain sample cleanliness and prevent contamination. After restoring the load lock to atmospheric pressure, the chamber is opened, and the processed substrate is removed. For this work an ICP Estrelas100 was choose with the parametre

shown in the table below to etch 800nm of α-Si and the hsq was used as etching mask:

Parametre	Value
IPC (W)	700
Pressure (mTorr)	12
SF_6 (sccm)	16
C_4F_8 (sccm)	48
Table temperature (^oC)	25
Process time (sec)	157
α-Si etch rate (nm/min)	165
HSQ etch rate (nm/min)	50

Table 3.3: parameters used for the dry-etch.

a   b
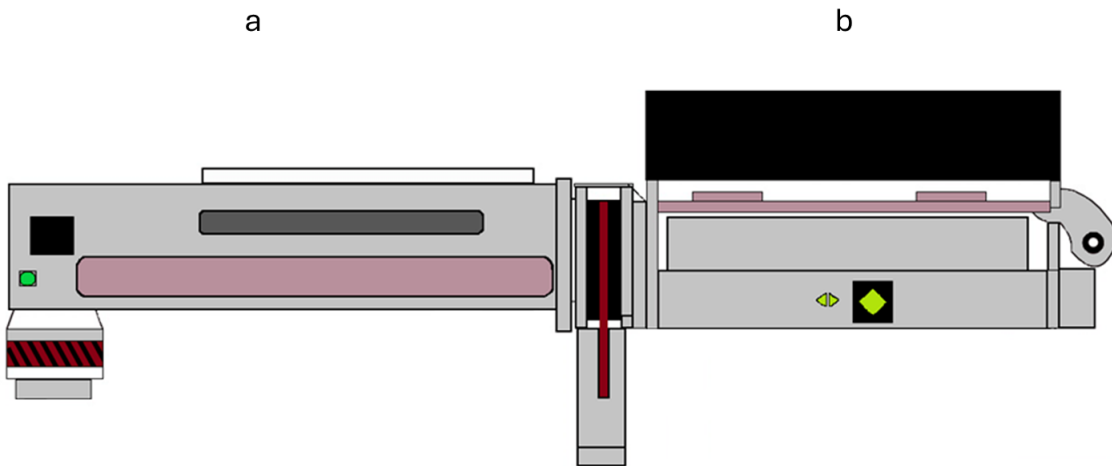
Figure 3.7: User interface of ICP Estrelas.

3.12 Interferometer

Regarding the manufacturing process, control over the dry etch step is crucial. One of the most challenging aspects is understanding the precise moment at which the process should be terminated. For this purpose, the interferometer is the necessary and essential tool. Interferometry is a technique that, using light, can measure small changes in the surface under examination and is based on the principle of interference. In the specific context, the setup relies on several key components, including a source of coherent light (laser), a beam splitter, and a series of mirrors. The beam splitter's task is to divide the light beam into two distinct beams, one serving as a reference while the other changes in accordance with the length of the path as the etching process progresses; changes in the length of the path of the second beam result in alterations in the interference pattern, which is captured by a photodetector. As the depth of the etching reaches the desired level, the interference pattern will exhibit a characteristic shift. This shift is a direct result of the changing path length in the sample path. By analysing the interference pattern and identifying the specific shift, the interferometer can precisely pinpoint when the etching process should be stopped. This ensures that the desired depth or pattern is achieved [156].

3.13 Scanning Electron Microscopy (SEM)

The SEM allows the users to obtain a high resolution image using a focused electron beam over a surface. The electron can interact with the sample and produce different signals that can give information about the composition and tomography of the device it is looking at. An electron gun generates the electron beam in a high-vacuum column (Fig 3.8). Various electromagnetic lenses can focus the beam and deflect it to scan the area by changing the lens and aperture to control and focus the beam. To produce a

high resolution and quality image, a secondary electron detector (SE) detects the signal

emitted from the sample. The amalgam of distance from the sample, voltage, current and

the beam alignment (stigma X and Y) play a foundamental role in the image's quality.

Some samples are not conductive and this causes the impossibility of analysis with this

instrument. To remedy the problem, the sample is generally covered with a conductive

layer which can be removed or not once the analyses have been completed. In this work

the images were taken using the Hitachi SU8230 and a Hitachi SU8240 SEM tool. The

microscopes were operated at $10kV/2\mu A$.
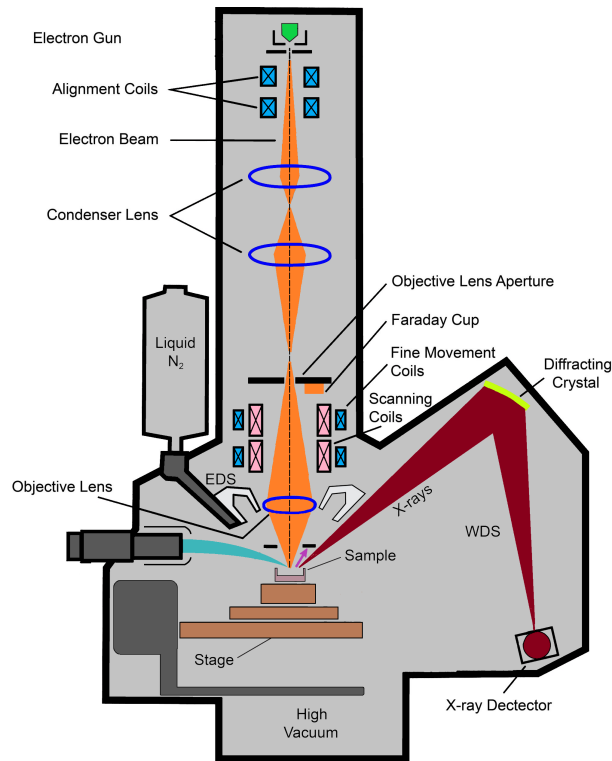
Figure 3.8: Schematic representation of SEM.

Chapter 4

Multi plane light converter

4.1 Introduction

The field of sensor technologies based on metasurfaces has witnessed significant growth in recent years, primarily attributed to the versatility and ease of production of metasurfaces once the protocol is established.

This growth has been further accelerated by the development of various mode sorters, or mode (de)multiplexers, designed to enhance the capability of decomposing a beam into its Laguerre-Gaussian components. This advancement is particularly crucial when aiming to increase the capacity of communication channels [157]. Metasurfaces have garnered increasing attention in recent years due to their unique ability to interact with light in unconventional ways, surpassing the characteristics of natural materials as explained in chapter 1.

One of the primary benefits of MPLC in telecommunications is the substantial increase in channel capacity through Mode Division Multiplexing (MDM). MDM allows multiple data streams to be transmitted simultaneously through different spatial modes within a single optical fibre. By converting HG modes into LG modes, MPLC facilitates the use

of these modes as distinct channels, increasing the data throughput without the need for additional fibres. This approach exploits the orthogonality of HG and LG modes, ensuring that signals remain isolated and independent, which is crucial for maintaining high data integrity and minimising cross-talk [158]. This capability is vital for meeting the growing demand for high-speed internet and large-scale data transfers [159]. Moreover, MPLC offers an efficient and compact solution for mode conversion. Traditional optical systems often require bulky and complex setups to achieve mode conversion and sorting. In contrast, MPLC incorporates multiple mode conversion functions into a single, compact device, utilising six distinct patterns on a glass slice in this specific scenario. This design reduces the physical space required for optical components and simplifies the integration process into existing network infrastructures, which is particularly beneficial for data centres and network nodes where space is at a premium. The scalable nature of MPLC technology means it can handle a large number of modes simultaneously, making it ideal for applications ranging from small-scale local networks to extensive global communication systems [160]. The work presented in this study extends the concept introduced by Fontaine in the journal Nature Communications a few years ago [161]. Our research group aimed to develop a mode sorter capable of converting HG bases into LG bases without necessitating an excessive number of conversion planes. The resulting MPLC device, manufactured for this thesis, represents the first-ever physical device based on metasurface capable of converting HG modes into LG modes. In contrast, existing solutions currently in use rely on projecting holograms onto other devices, such as SLMs. Simulations were employed to refine this concept, leading to the development of a device incorporating a metasurface. The choice to use a metasurface for this new device was motivated by the intrinsic characteristics of metasurfaces discussed in earlier chapters. As previously mentioned, six conversion masks were developed. Within this chapter, a comprehensive overview is provided of the numerical and experimental techniques employed throughout

this thesis. The entire process of fabrication, as well as the microscopic characterisation through both optical and scanning electron microscopy (SEM), was conducted inside of the James Watt Nanofabrication Centre (JWNC) at the University of Glasgow. Additionally, the acquisition of optical transmission data took place in the premises of the Advanced Research Centre Building, also situated at the University of Glasgow. All the tools and techniques employed in the creation of the device have been described in preceding chapters; here, only the manufacturing steps, characterisation results, the optical setup and their corresponding outcomes will be presented.

4.2 Materials

Material	Brand
Acetone	Fisher Scientific
Aluminium	Kurt J. Lesker Company
CCD camera	GoldenEye
HF	Fisher Scientific
HSQ	Dow Corning, Co
IPA	Sigma-Aldrich
Laser source	Thorlabs
Lenses	Thorlabs
MeOH	Sigma-Aldrich
MIBK	Fisher Scientific
ND filters	Thorlabs
SLM	Cambridge correlator
TMAH	Fisher Scientific
JGS2 Fused Silica	Microchemicals

Table 4.1: Materials, brands and tools required for the fabrication and analysis of the MPLC.

4.3 Determination of patterns through simulations

This paragraph explains how the phase masks were obtained through simulations.

The Hermite-Gaussian (HG) modes are decomposed into a Cartesian array of Gaussian spots using six phase planes. The process begins with a Cartesian grid of spots positioned at coordinates x,y (Fig. 4.1).
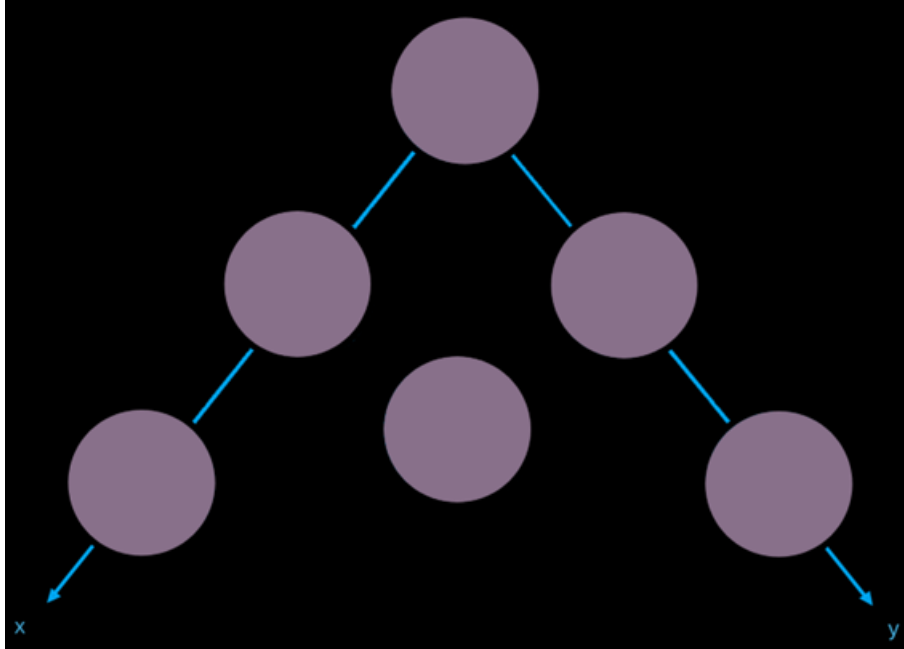
Figure 4.1: Cartesian representation of the spots.

Each of these spots is then mapped to its corresponding HG mode with an index of m, n (Fig. 4.2).
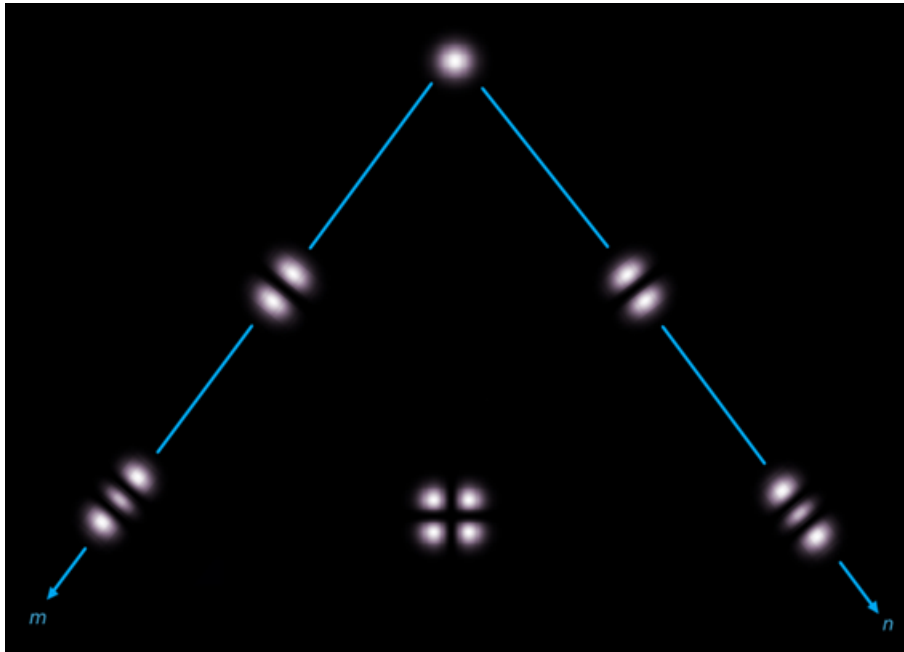
Figure 4.2: Cartesian coordinates for HG modes.

Following this, the HG modes are converted into LG modes through the use of cylindrical lenses (Fig. 4.3).
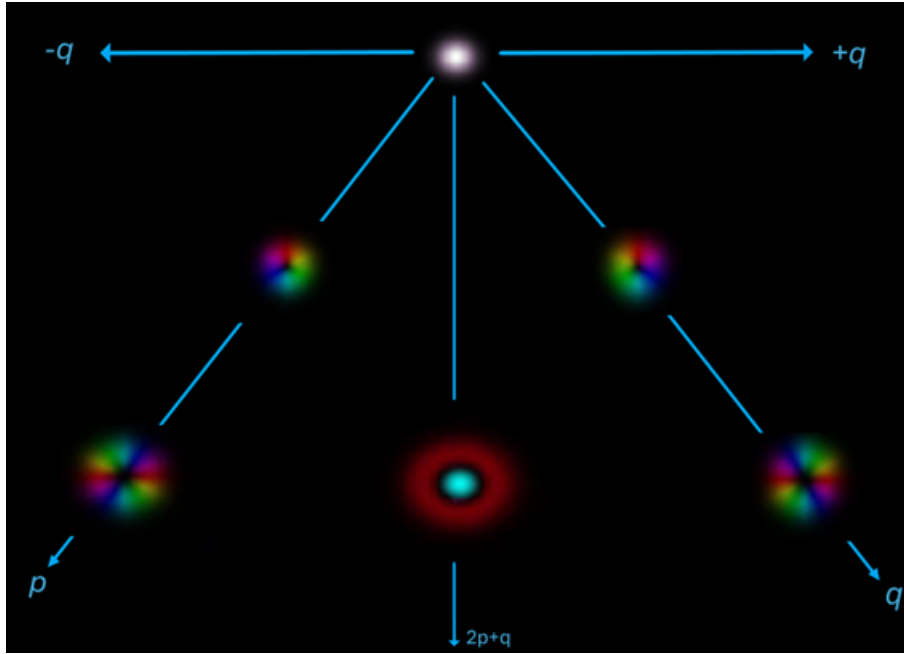
Figure 4.3: Cartesian coordinates for LG modes.

The fundamental algorithm employed is straightforward and is based on wavefront matching, also known as adjoint optimisation. To achieve the desired transformation, it is necessary for the fields to be matched in both forward and reverse directions at all points. This matching is accomplished through the use of phase planes.

An input basis, represented as an array of spots, is considered at the start. The desired output basis, which the transformation aims to achieve, is back-propagated through the initial system until the first phase plane is reached again. Adjustments are made to correct errors during this process.

The objective is to ensure that each forward-propagating mode aligns with its corresponding backward-propagating mode using the phase plane. The spatial overlap of each pair of input and output modes is calculated. These overlaps are then summed, and the resulting phase is used to form a new phase mask, which represents the average phase

error for all modes moving forward and backward.

This process is iteratively repeated: the spatial overlaps of each pair of input and output modes are calculated, summed, and their phases are extracted to create new phase masks. This cycle is continued, propagating back and forth through the phase planes, until convergence is achieved, the resulting masks are shown in Fig. 4.4.
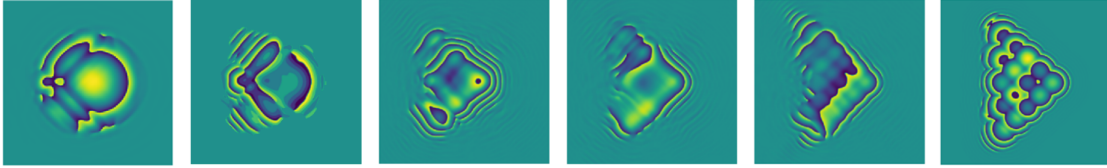
Figure 4.4: Representation of the 6 masks required for the MPLC resulting from the simulations.

4.4 Fabrication of the device

A top-down approach was used for the fabrication of the MPLC (see chapter 2.7). The figure below (Fig. 4.5) schematically represents all the steps necessary for the fabrication.

Once the fused silica has been cleaned (Fig. 4.5a) following the procedure in Chapter 3.3, 800 nm of α-Si were deposited using the PECVD Delta (Fig. 4.5b), and the substrate was cleaned again to ensure the removal of any residue (organic or inorganic).

After these steps, two different layers were spun onto the sample, one of HSQ (Fig. 4.5c) with a 1:2 ratio at 2000 rpm (resulting in a thickness of 360 nm), which serves as a photoresist for the lithography process, and the other of PSSA/Triton100 (Fig. 4.5d) (prepared according to the procedure explained in Chapter 3.7), which acts as an intermediate layer between the photoresist and the conductive layer to facilitate the removal of the latter. Between both layers, the sample was placed on a hotplate for 5 minutes at 90 ^{0}C. To prevent charge build-up and enable electron conduction during the e-beam lithography process, a 20 nm Al charge conduction layer was deposited (Fig. 4.5e) by electron-beam

metal evaporation (two different instruments were used for this step, the Plassys MEB 550S and the Plassys MEB 400S, which are interchangeable with each other); during the deposition process, the sample is continuously rotated, and both deposition and rotation are automatically controlled by the machine (0.5 nm/s deposition rate).

The sample was then subjected to lithography (Raith EBPG 5200)(Fig. 4.5f) with the parametres described in Table 3.2 in Chapter 3.9. In order to determine the correct electron dose for writing, a substrate consisting of the same pattern with varying doses was written and examined by SEM (Hitachi SU8230 and Hitachi SU8240). After lithography, it is necessary to develop the sample using TMAH (Fig. 4.5g). A 25% TMAH solution was used for 3 minutes and 15 seconds. Then, the sample was rinsed in water twice for 30 seconds each time.

Finally, it underwent a dry etching process using Estrelas100 for 6 minutes (Fig. 4.5h). Once the correct timing and recipe were confirmed with the instrument through multiple attempts and corresponding microscopic analyses, both optical and electron microscopy, the device was further etched in hydrofluoric acid to remove any remaining residues of HSQ mask (Fig. 4.5i).
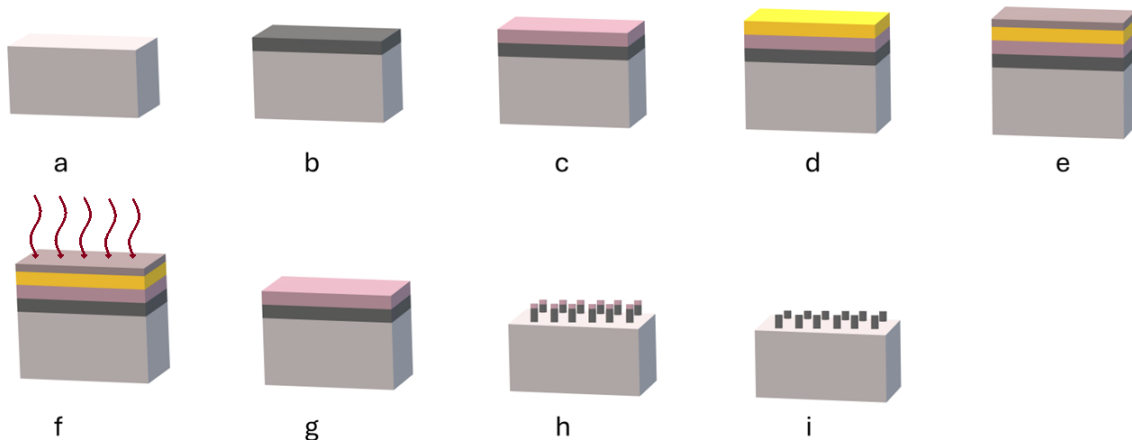
Figure 4.5: Fabrication's flow. a) substrate cleaning, b) α-Si deposition, c) HSQ spinning, d) PSSA+Triton100 spinning, e) Al deposition, f) e-beam lithography, g) development, h) etching, i) removal photoresist and unwanted α-Si.

4.5   Results

This paragraph focuses on the results obtained for each manufacturing step and how the metasurface looks like ones exposed to the laser source.

4.5.1   Dose and development test

As mentioned in the previous paragraph, once the file with the masks has been obtained it is necessary to start the manufacturing process; once the necessary cleaning of the sample and the deposition of the α-Si, HSQ/ PSSA/ Triton100/Al have been carried out, it is possible to move on to lithography. This step can create problems and it is necessary to carry out more than one test to understand the parametres necessary to obtain the desired results. The images below are a clear example of parametres not set correctly in the export phase with MobaXTerm, a Windows terminal. An important factor not to be underestimated during pattern fracturing is the time needed for lithography, the smaller the beam and the step the greater the time needed for EBPG, so it is necessary to be able to find a good compromise between the desired form and time. Both the results after fragmentation with the software and the images obtained with the microscope are depicted.

The figure is divided into parts A and B, where A shows the possible fractures obtained, in particular from 1 to 3 are fractures not suitable for fabrication as the circular shape is not maintained while image 4 is a good compromise between the shape and the time necessary for its lithography. Part B shows the images obtained by electron microscope of the first tests carried out for the completeness of the protocol; image B1 is a top view of an incorrect fracture, B2 is a lateral view of the same, while 3 and 4 are two examples of dose tests carried out, 3 specifically is an overexposure while 4 is the correct dose (in our case 2000 μC/cm^2 as explained in the previous chapter).
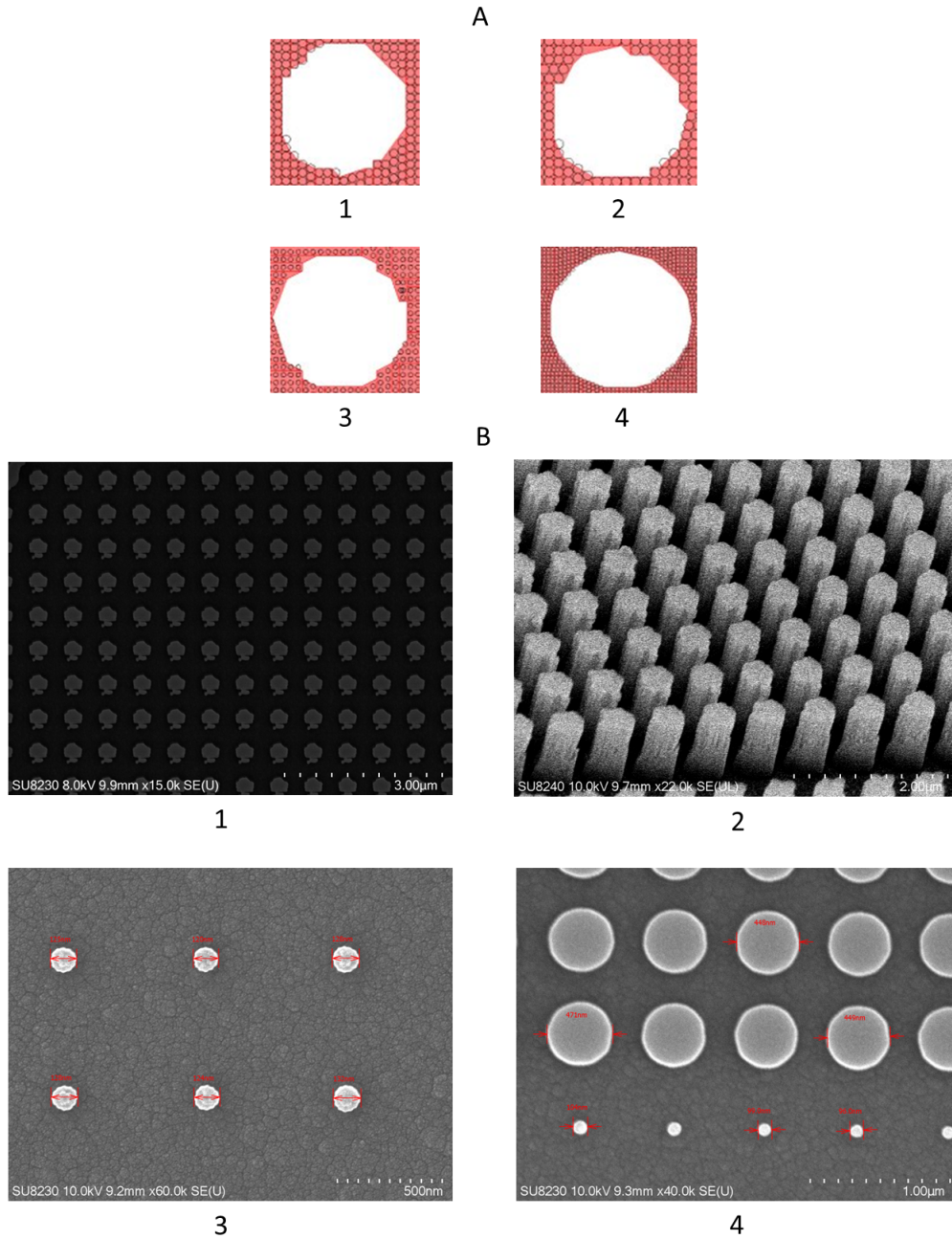
Figure 4.6: Representation of fracturing in the manufacturing process. A shows the fracturing images extracted by the software, 1-3 fracturing failed correctly, the images of the circles are not clear, 4 the fracturing with the relative parametres used. B1 top view of the dose-fracturing test, B2 lateral view B3 dose test failed B4 dose test successful.

4.5.2 Dry etch experiment

As with lithography and development, this step also required trying different approaches before finding the right combination of gases and time to achieve satisfactory results; to be certain of the end of the run, the interferometre was used, with particular attention to not positioning the laser on the pattern but close to it, otherwise the sample could be ruined and made unusable.

Parametre	Recipe 1	Recipe 2
SF_6 (sccm)	26	16
C_4F_8 (sccm)	53	48
He (mTorr)	10	0

Table 4.2: Differences in gaseous concentration between recipes.

Two different recipes were tested and the results are shown in the figure 4.7; these recipes differ for the concentration, expressed in sccm, of the gases of interest and for the presence of an additional gas in the first recipe, absent in the second as reported in the table 4.2, while the unchanged parametres are reported in table 3.3, chapter 3.

Figure 4.7, as previously mentioned, shows the results of the two different recipes used. In the first row, it is possible to notice that the cylinder profile is maintained; however, the apical part of each pillar appears "eaten." This indicates that there was an overetching, meaning the exposure was too long, resulting in the entire HSQ mask being removed. Consequently, the top of each structure inside the machine was exposed to the plasma (overetched) (FIg. 4.7a - c). Specifically, in Fig. 4.7c, the overetched apical part is circled, highlighting the area most affected by the excessive etching.

In the second row, the results of the second recipe used are presented. It is clear that, in this case, the cylindrical profile was maintained much more distinctly than in the first,

and the HSQ mask is still present, preserving the intact shape (Fig. 4.7d, e). In Fig. 4.7e, the remaining HSQ is represented by the red areas, indicating the portions of the mask that were not removed by the plasma.

Finally, image "f" provides a detailed enlargement of a pillar that has been overexposed to the plasma, further illustrating the effects of overetching.

In total, the run lasts 6 minutes, and the machine must be preconditioned for 15 minutes beforehand to create an environment suitable for the required recipe and to avoid contamination by other gases.
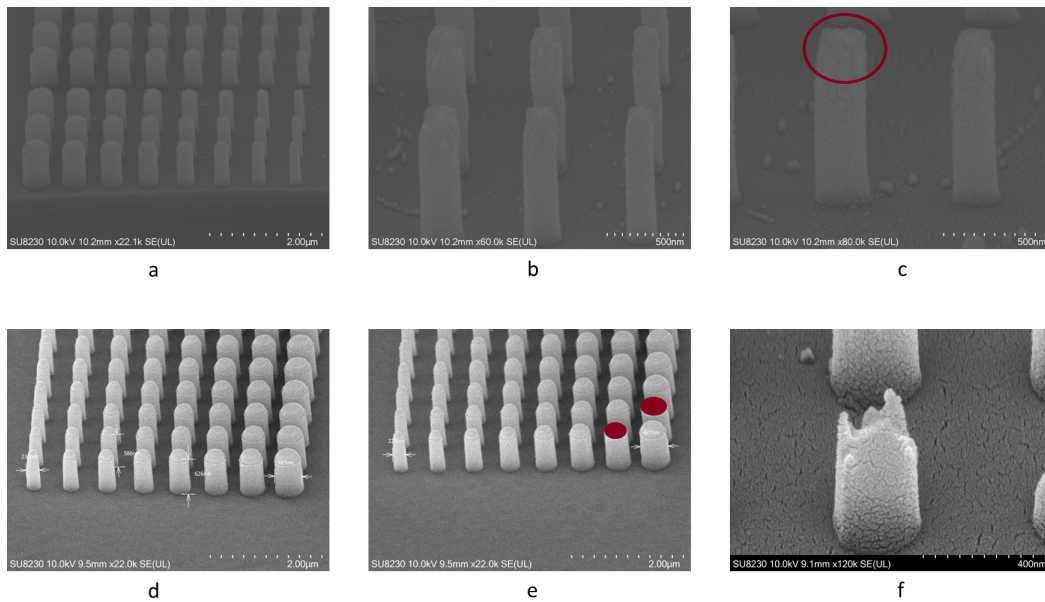
Figure 4.7: Images obtained with SEM to check the success of the dry etch process. a-c) results of the first recipe; the cylindrical profile is visible but not well-preserved. In image "c," the overetched apical part is circled, indicating where the excessive etching has occurred; d-e) results of the second recipe; the profile is sharper and more distinct; in image "e," the red areas represent the remaining HSQ, showing the portions of the mask that were preserved during the etching process; f) detailed enlargement showing the effect of an overetch run, where the excessive plasma exposure has altered the structure.

Once the fabrication process was finished, the first metasurfaces were used as tests to check the actual truthfulness and reproducibility of the protocol, in total 3 tests were carried out, the figures shown below are a comparison between the simulations, the optical

images taken after the development step and the electron microscopy images at the end

of the fabrication, the figure is divided into six different sections (a - f) each of which

depicts a specific mask.
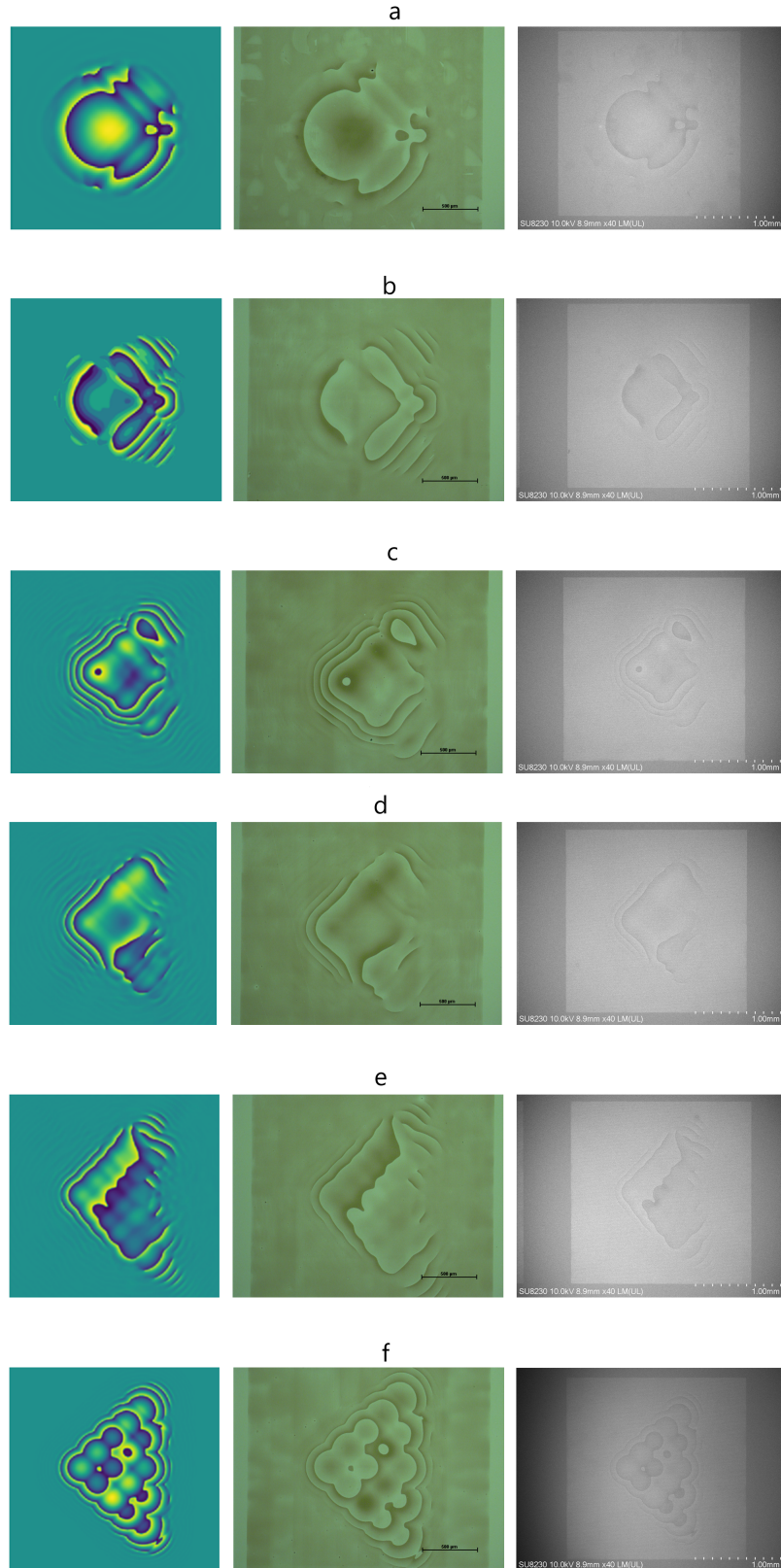
Figure 4.8: Comparison between three different steps of the manufacturing process for all masks (a -f). First image of each row: simulations; second: post-developmentoptical microscope; third: SEM at the end of the process.

The following images will show the patterns in greater detail than Figure 4.8, as the purpose of the former is to display the actual shape of the pillars, whereas the latter aimed to depict the entirety of the pattern.
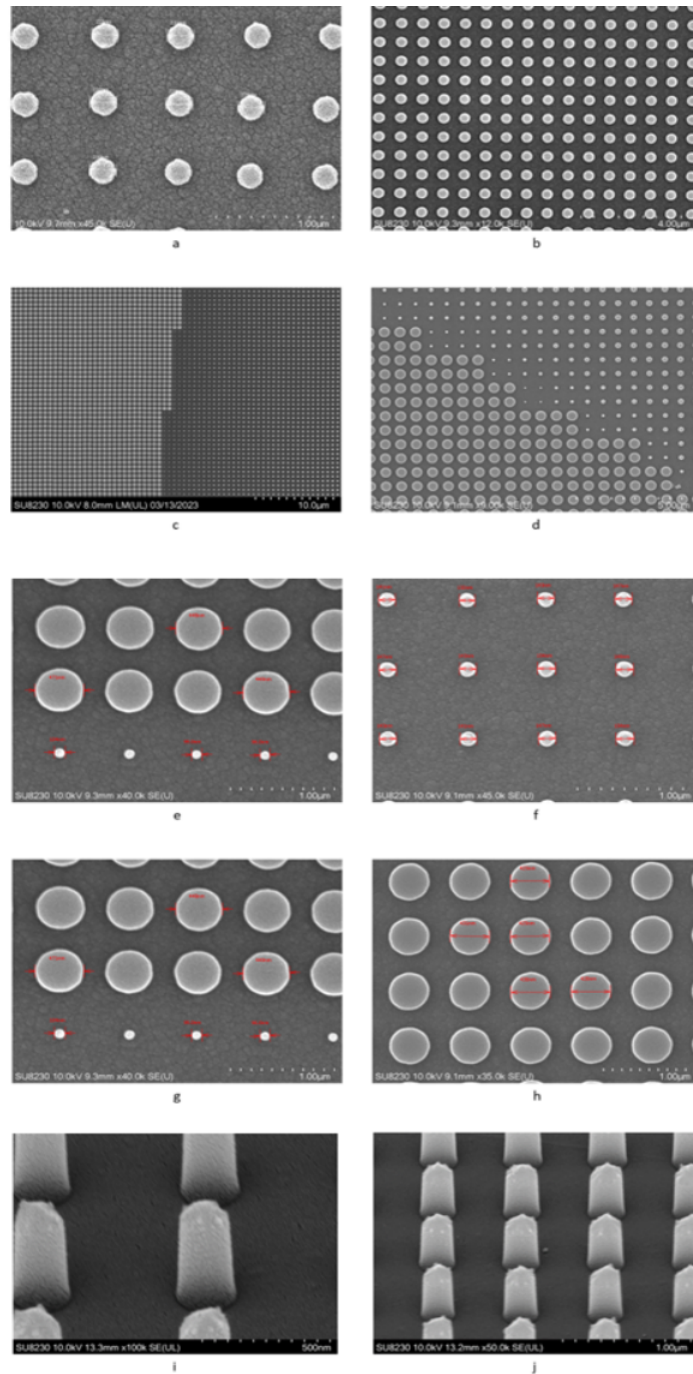
Figure 4.9: Enlargement of the pillars component of the MPLC obtained via SEM.

Figures 4.8 and 4.9 provide tangible evidence of the success of the manufacturing process. In the first image, a little enlargement is chosen to allow a detailed view of the inherent complexity of the generated patterns. These patterns have been meticulously compared with previous simulations and results obtained through optical microscopy.

It is particularly noteworthy that all six patterns exhibit a correspondence with the design expectations, underscoring the effectiveness of the implemented protocol. The patterns are labelled from A to F based on the order in which they are illuminated by light, where A is the first and F is the last.

In Figure 4.9, as previously mentioned, a visual deep dive is outlined. Here, groups of structures of varying sizes positioned on different patterns are highlighted. Once again, observation reveals a precise alignment of dimensions with what was predicted by simulations. This further confirms the robustness and reliability of the employed protocol.

In conclusion, these results consolidate the validity of the manufacturing process, emphasising the coherence between theoretical projections and actual practical realisation. Precision and adherence to predefined designs are key elements that delineate the success of this approach, opening promising prospects for future applications and further developments in the manipulation of optical modes.

4.6   Failed approaches

As with all new processes and protocols, one encounters several unsuccessful attempts. This research was no exception. One of the initial attempts to develop a protocol was initially based on using the STS Multiplex ICP as the tool for dry etching, and the protocol did not involve the use of HSQ as a mask. Instead, it employed a double layer of two different types of Poly(methyl methacrylate) (PMMA), and initially, there were 7 masks to be fabricated, which were later optimised to 6. Below is a schematic representation of

the protocol in which a double layer of PMMA with different molecular weights (50K, 310 nm of thickness and 950K 70 nm of thickness) is spin-coated (4000 rpm) onto 800 nm of α-Si and baked on a hotplate at 180 degrees Celsius for 5 minutes. Following this process, the sample undergoes lithography and subsequent development in MIBK:IPA 2.5:1 for 45 seconds (e). The next step involves depositing a 300 nm-thick layer of Al onto the sample surface and subjecting it to overnight lift-off (f). Finally, the sample undergoes dry etching (g), and thanks to the use of TMAH, the remaining Al layer is removed.
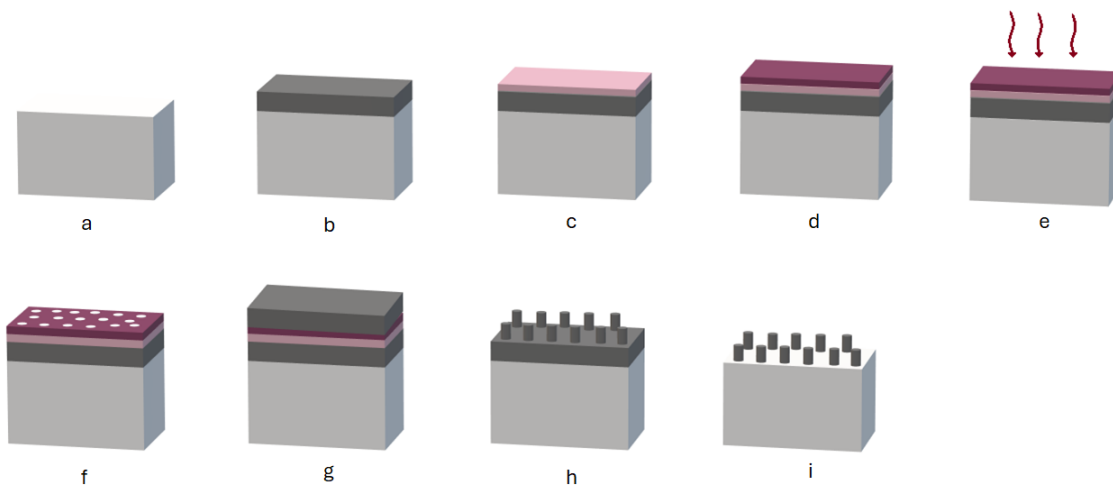
Figure 4.10: First fabrication's flow. a) substrate cleaning, b) α-Si deposition, c) first layer of PMMA, d) second layer of PMMA, e) e-beam lithography, f) development, g) Al deposition, h) etching, i) removal unwanted α-Si.

Utilising this protocol, only preliminary tests were carried out as the instrument was decommissioned shortly after confirming the protocol's effectiveness and repeatability. It was challenging to find a practical way to assemble the 7 different metasurfaces together, which led to the decision to fabricate the optimised masks on a single surface. Initially, an attempt was made to assemble the metasurfaces individually with the appropriate thickness of approximately 2 mm, but this was not easily controllable. Subsequently, a 3D support was created to place the metasurfaces, but this also proved to be tricky. For this reason, it was eventually decided to create patterns that could be placed on a

single substrate of fused silica. Below are some images taken with an optical microscope showcasing the results obtained using this method.
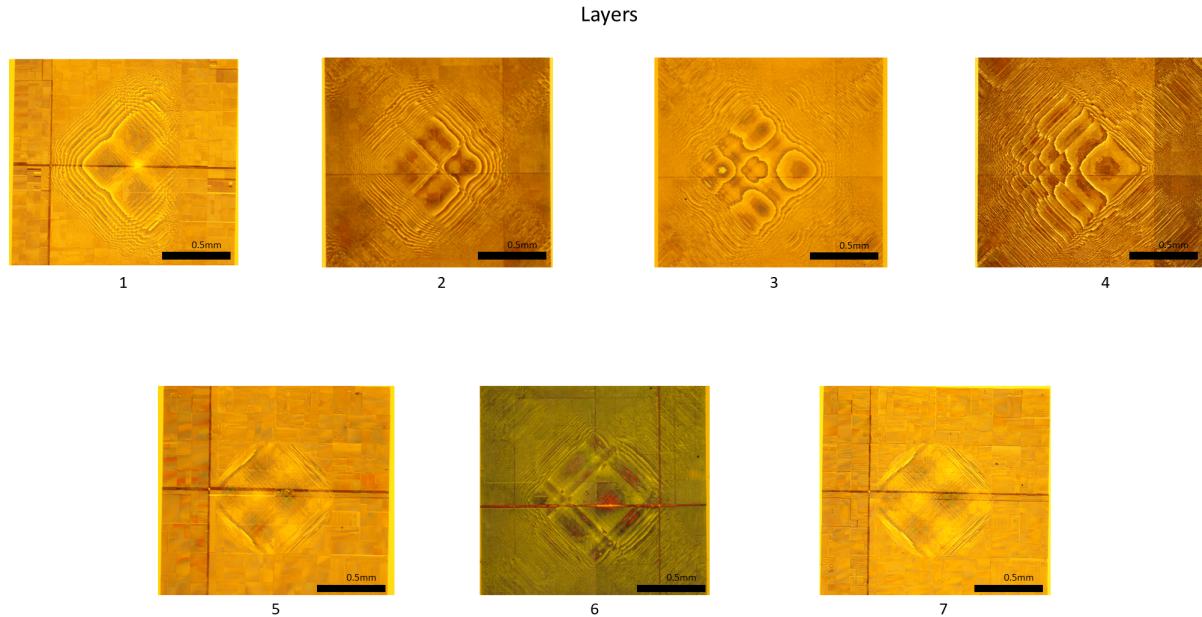
Figure 4.11: Images obtained with the optical microscope of the 7 initial patterns that make up the MPLC.

Once the decision was made to decommission the equipment, an alternative approach to fabrication was initiated, which led to the current procedure. In this new protocol, Electra was introduced as the electron conductor for lithography, replacing PSSA. On one hand, this eliminated one step in the process as the deposition of aluminium before lithography was no longer required. However, it was found to be challenging, if not impossible, to remove the polymer after exposure to e-beam. Various removal methods were experimented with, including immersion in room-temperature water (as suggested in the literature), as well as hot water (at 25 degrees and 50 degrees Celsius), but reproducible results were not achieved. While some samples exhibited complete removal of Electra, others showed only partial dissolution. After numerous attempts, the decision was made to abandon this approach and try to use of PSSA.

4.7 Preliminary optical analysis

Once the metasurface with the required masks is obtained, optical analyses can commence. To do so, it is necessary to align the optical setup and introduce the metasurface with care, ensuring that the distances between the mirrors and the metasurface are maintained and that the latter is handled delicately to avoid compromising the integrity of the patterns.
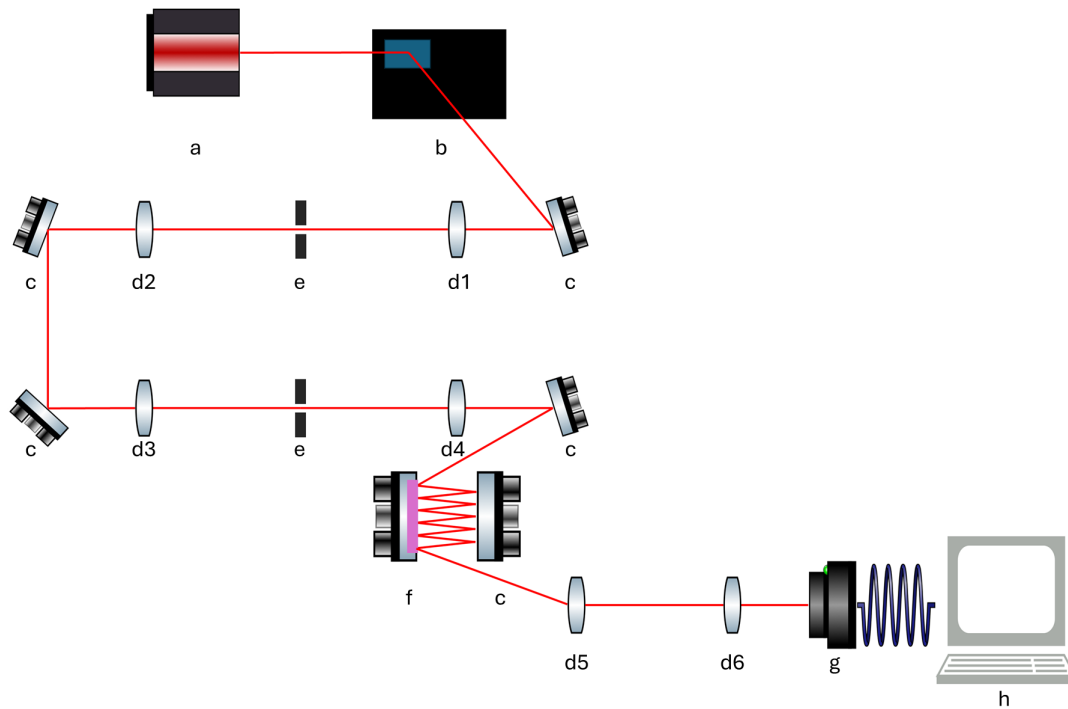
Figure 4.12: Schematic representation of the optical setup: a) ALK 8513 fibre; b) SLM SN5513 HSP1920-850-1650; c) mirror; d1) LA1805-c-ML 30mm; d2) AC 254-30-c-ML 300mm; d3) AC 254-300-c-ML 300mm; d4) LA 1608-c-ML 75 mm; d5) LA1131-c-ML 50 mm; d6) LA 1590-c-ML 100mm; e) pinhole; f) metasurface on support; g) CCD camera; h) pc.

As shown in Figure 4.12, the optical table setup initially consists of a 1550 nm ALK 8513 laser light source (a). This source is directed towards an SLM of model SN5513 HSP1920-850-1650, connected to a PC capable of imprinting an HG beam at the output (b). Subsequently, the light beam passes through two lenses (d1: LA1805-c-ML 30mm,

d2: AC 254-30-c-ML 300mm) and a pinhole (e) after being redirected towards the lenses by a mirror (c).

Given the initial size of the beam, it was necessary to reduce its magnitude, and to achieve this, two more lenses were used (d3: AC 254-300-c-ML 300mm; d4: LA 1608-c-ML 75 mm). From here, the beam reaches the metasurface. This metasurface is positioned between a mirror and a support and is placed above another support that allows specific and controlled movements in three dimensions, ensuring that each individual mask comes into contact with the light beam and is spaced correctly. The mirror in front of the metasurface is also equipped with three knobs to adjust its position.

Once the beam exits the metasurface, it needs to be resized for it to be of the appropriate size to be captured by the camera (g). For this purpose, two more lenses were used (d5: LA1131-c-ML 50 mm, d6: LA 1590-c-ML 100mm).

To align the MPLC, one of the crucial factors was ensuring that the mirror and the device were perfectly parallel at a distance of 27 mm from each other. To achieve this, a caliber was used. Once the two structures were parallel, the alignment of the first pattern was carried out, ensuring that the light hit the centre, then the second pattern, and so on. Each time, adjustments were made to the inclination of the metasurface using its supports, which allowed for tilting the metasurface and moving it along the x-axis. The figure below (Fig. 4.13) represents a magnification of how the light beam is directed in conjunction with the metasurface. The pink structure with blue squares represents the metasurface with the 6 masks (1-6), the two rectangular structures in shades of grey with three blue cylinders represent the mirror and its attached support. The black structures are the supports holding the MPLC, and the red arrows indicate the directions in which it is possible to manoeuvre the device's support.
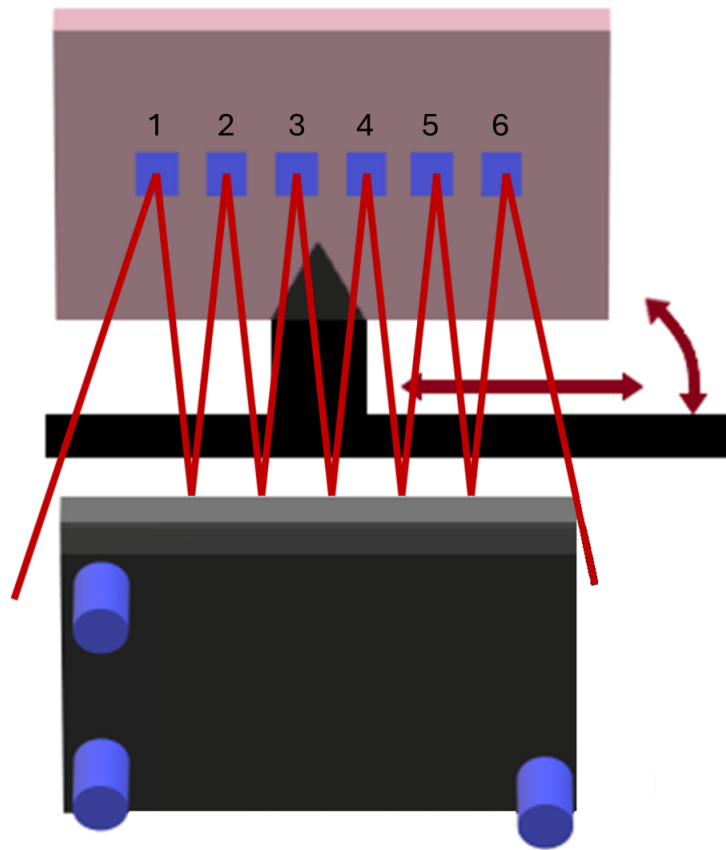
Figure 4.13: Schematic representation of how light passes through the MPLC. The beam strikes each mask and propagates through the mirror placed parallel to the device. The masks are spaced 27 mm apart from the mirror, starting from the centre.

Preliminary analyses involved capturing video data for a limited set of six HG modes, aiming to identify bright focal points required for the formation of a triangle and to validate the efficacy of MPLC. It is imperative to emphasise the system's high sensitivity to alignment, and while full alignment proved challenging, the initial findings are exceedingly encouraging. The system exhibits the capability to discern movements corresponding to each specific HG mode employed.

Figures 4.14 and 4.15 display the preliminary results of the experiments. The first image shows the overall result of the outcomes obtained in video format, with each frame overlaid on the previous one to create a single composite image. As can be seen, these

results match the simulations performed and presented earlier in the chapter. The second image shows each individual spot resulting from the transformation of an HG basis into an LG. Since the original file is in video format, it was necessary to extract individual frames, enlarge them, and highlight them, aided by the presence of red circles delineating the bright spots generated by the MPLC. It is evident that some of these spots are clearly discernible (a, c, f), while others appear less distinct, with two adjacent spots (b) or three spots (d) that are spatially separated, suggesting the potential for cross-talk among the incoming HG modes.
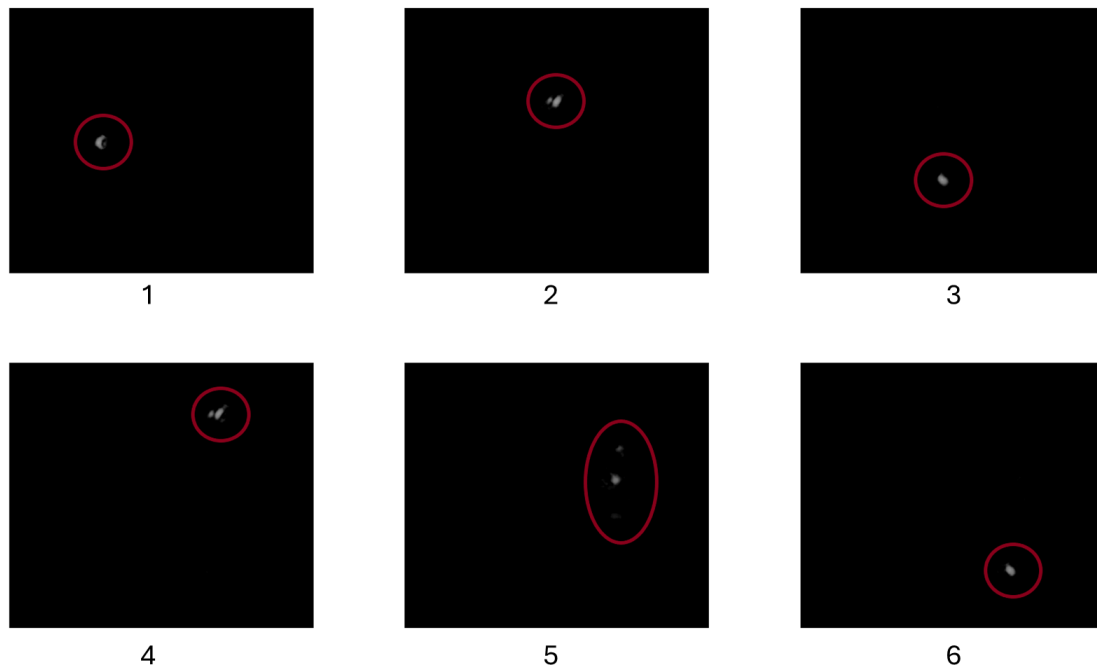
Figure 4.14: Results of the MPLC operation obtained by compiling the individual frames from the original video format.

Figure 4.15: Images extracted from the original video showcasing the MPLC's operation. Some spots are sharp (a, c, f), while others are less so; this is due to imperfect alignment of the optical setup.

The reasons for having unclear spots could be attributed to three main factors:

- The optical setup is not properly aligned, which is highly likely

- One or more patterns on the device are damaged (scratches, missing pillars, manu-facturing issues), which is less likely

- The design of the patterns is incorrect, which is improbable since the preliminary results appear to match those obtained in the simulations

4.8 Conclusion

In this chapter, a detailed explanation was provided on how the device was produced in a cleanroom environment, with all necessary steps and corresponding images used to support the accuracy of each specific step. Furthermore, an overview was given on how the optical table was set up and the instruments that were utilised. The results obtained so far indicate that the MPLC appears to be operated satisfactorily but not perfectly. However, further analyses and optimisations are deemed necessary to fully realise its potential.

Versatile applications are promised by this device across various sectors, from the

potential amplification of the signal in telecommunications[71] to its utilisation in energy-related fibre sensing technology, as well as its application in medical and biological fields such as flow cytometry[72]. This emerging technology is increasingly drawing the attention of the scientific community, particularly for its relatively cost-effective nature. The possible transition to new manufacturing approaches, such as the use of pattern printing to generate patterns, is believed to be significant in reducing production costs and opening up further opportunities for future development.

Chapter 5

Structured light enhanced ML for fibre bend sensing

The work presented in this chapter has led to the publication of an article in the journal Optics Express in February 2024 (Vol. 32, Issue 5, pp. 7882-7895 (2024)) [87]. This study was conducted in collaboration with Z. Chen, L. Škvarenina, A. W. Clark, A. Walles and M. P. J. Lavery hailing from various institutions including the University of Glasgow, the University of Brno and The Barcelona Institute of Science and Technology. My role focused on experimental aspects, including optical setup, experimental optimization, data acquisition, and analysis. The other authors made significant contributions to the theoretical component and provided guidance on the experimental aspects of the work.

5.1   Introduction

The increasing interest in studying how light interacts with different materials, as discussed in earlier chapters, has seen a significant rise in recent years. This growing has caught the attention of researchers and institutions worldwide. The surge in interest is mainly due to the way light changes when it travels through a material. A clear example of

this is seen in multi-mode optical fibers, where different modes of light mix together due to reasons like imperfections in manufacturing, impurities, and bending caused by external factors. As a result, this mixing of modes creates interference, making it challenging to distinguish between the different modes of light supported by the optical fiber during both input and output.

Efforts to address the issue of disorder in intricate media, encompassing, among others, optical fibres, have yielded a plethora of research findings across various domains, including communications [162][163][164][165], imaging [166][167][168][169], quantum optics [170] and optical sensors [171][172]. Nevertheless, the continual fluctuations in the relative phase between optical modes introduce a source of phase noise, thereby constraining the precision of sensors relying on few-mode or multi-mode optical fibres [173]. Although inter-modal coupling, in isolation, could serve as a reliable characteristic for optical fibre-based sensing, the precise quantification of this effect necessitates the minimization of intensity fluctuations arising from relative phase shifts within the superimposed coupled optical fibre modes. The development of low-complexity, high-precision shape-sensing techniques holds significant potential for the advancement of optical fibre sensors, creating opportunities for a wide spectrum of innovative sensing applications and facilitating their broader deployment.

One of the most commonly used techniques today for identifying damage in optical fibre is OTDR (Optical Time Domain Reflectometry). It emits high-frequency light pulses that travel inside the fibre. When the light encounters an irregularity, such as a bend or break, a portion of the light is reflected back, and the time required for the entire journey is used to calculate the distance between the instrument and the point of curvature or break [174]. Currently, tools have been commercialised that can distinguish breaks within a range of approximately ± 20 metres on multi-mode fibres. However, ongoing efforts are aimed at achieving even greater accuracy through enhancements in laser sources,

interferometric techniques, and timing electronics [175], all based on the principles of Rayleigh scattering [176]. Bragg grating technology represents another widely employed approach for shape sensing within optical fibres. This method involves the incorporation of periodic grating structures into the fibre. These grating structures, when subjected to perturbations, undergo a change in their periodicity and subsequently reflect light of a specific wavelength, which is indicative of the strain or temperature variations in proximity to these grating structures. Tailored fibre configurations have demonstrated their ability to deliver high-precision shape detection, with the sensor's accuracy primarily constrained by the frequency resolution of the optical spectrum analyser employed for measuring frequency shifts in the back-reflected signal [177][178][120]. While both OTDR and Bragg grating technology offer precise measurements, they present non-trivial challenges in achieving high-accuracy shape sensing, particularly when dealing with millimetre-scale resolution and shallow bend radii. Recent investigations have suggested that coherent detectors can be applied to single-mode fibres in use to extract environmental information [179]. Moreover, integrating traditional OTDR or Bragg-grating technology with machine learning techniques can enhance the resolution of sensors utilising few-mode fibers. However, intermodal coupling and phase noise significantly impact the accuracy of these systems [173]. Optical components have been effectively utilized as all-optical pre-processors for machine or deep learning, improving computational efficiency and accuracy [180][181][182][183]. Additionally, commercial shape sensing fibers, such as those developed by Philips using their Fiber Optic Real Shape (FORS) technology, have shown practical applications in various fields, including medical procedures. FORS technology enables real-time, 3D visualization of devices inside the body without the need for fluoroscopy, reducing radiation exposure and improving the accuracy of minimally invasive procedures. This technology has been successfully integrated into Philips' interventional X-ray systems and has demonstrated submillimetre precision in clinical studies, making it

a valuable tool for complex vascular interventions [184]. Thus, combining custom optical elements with machine learning could lead to the creation of low-complexity fiber shape sensors, potentially revolutionizing consumer electronics like wearable devices or vehicle sensors.

When there is inter-modal coupling in a fibre, power from one specific spatial mode is distributed among adjacent spatial modes. These relative phase shifts will continually change over time and due to varying environmental conditions. Consequently, they can be approximated as random variations over time. The impact of these relative phase shifts on the measurement of inter-modal coupling is minimised by the new modal decomposition method explained in this chapter which specifically employs intermodal coupling as a measurement technique, with an approach referred to as "structured light enhanced machine learning" for millimetre scale bend sensing in up to a 1 km of few-mode optical fiber. Modal decomposition, referred to as mode sorting or mode de-multiplexing [185][186], are optical methods used to determine the linear superposition of orthogonal modes that can be used to represent any structured optical field, such as the output from a bent few- or multi-mode optical fiber, as shown Fig. 5.1.
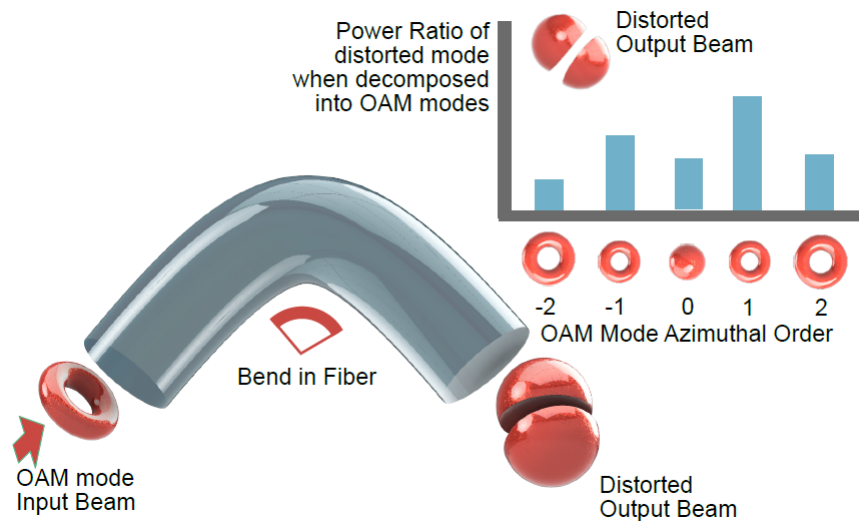
Figure 5.1: When high-order optical beams are coupled in optical fibers, intermodal coupling occurs, distorting the beam. This distortion can be measured using a mode de-multiplexer to quantify the distribution of power between OAM modes. When used as trainable features for machine learning, these power distributions can identify the positions (or degree of bending) in a few- or multi-mode optical fiber [87].

5.2 Optical table set up and ML algorithm

At the outset, the data collected from the optical fibres were found in the form of images, and an initial attempt was made to employ a CNN as the algorithm for determining both the position and the corresponding OAM mode. However, the results revealed a significantly low level of accuracy, which prompted the exploration of an alternative approach involving spectral data. This alternative approach was shown to have a notably higher level of accuracy, suggesting that the algorithm and data formatting best suited for the objectives of this series of experiments had been identified.

An additional rationale for choosing a spectrum-based classification algorithm over image-based methods arises from the substantial computational time required for the latter. In practice, analysing each individual OAM mode at a specific position using image-based calculations demanded approximately 4 hours. This resulted in excessively

prolonged analyses. However, after implementing optimization measures, the total processing time for all experiments, including both pure mode and superposition mode (which would have originally taken 12 hours combined), was reduced to around 3 hours, effectively saving 9 hours in the overall analysis time. After the data had been acquired, it was subjected to analysis using a variety of machine learning algorithms to determine the most suitable one for our dataset. The images were transformed into spectral matrices, with the resulting numerical values corresponding to each pixel on the camera. For each analysis, ten separate tests were carried out, each involving 100 spectra for OAM modes, encompassing both single positions and pure modes, distributed across 11 different fibre bending positions. The collected data were divided into two distinct datasets: one used for training the algorithm, referred to as the training set, and the other for testing to evaluate the algorithm's real-world accuracy, known as the test set. All the algorithms employed in this study are classification algorithms, which include Decision Tree, Logistic Regression, Naive Bayes, and others. Although they did not yield results as favourable as the SVM (for more details, refer to Chapter 2.10.1), the outcomes of these algorithms will not be displayed in this section. Instead, they will be presented as graph due to the substantial volume of data in the appendix. Below is an image showcasing the optical setup used for data acquisition.
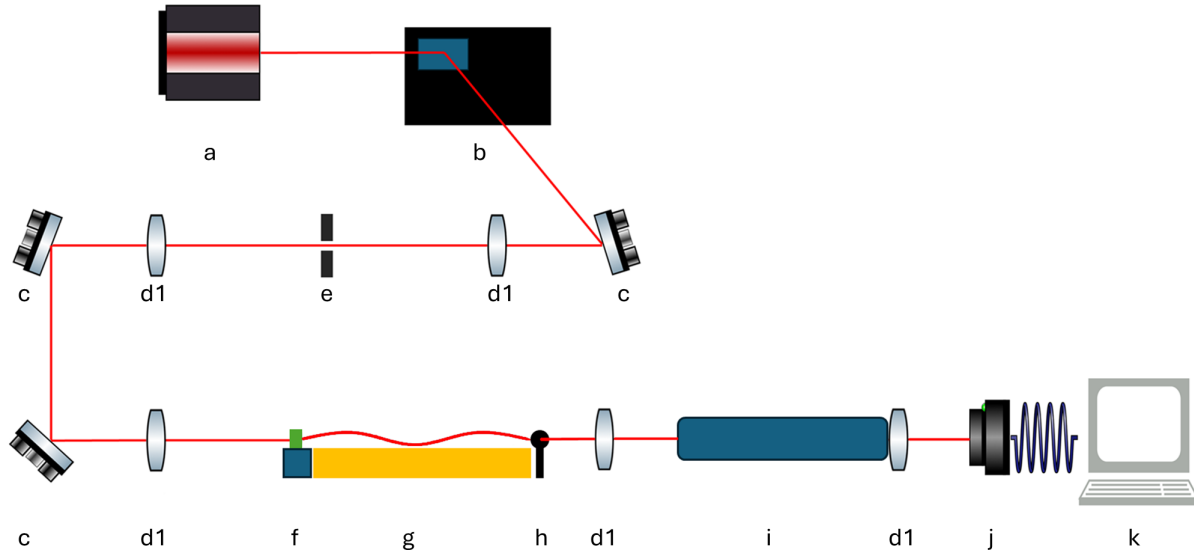
Figure 5.2: Schematic representation of the optical table. a) laser source, b) SLM, c) mirror, d) lens, e) pinhole, f) Microscope Olympus RMS10x, g) Thorlabs LTs300/M stage and memory foam, h) fibre suppport, i) mode sorter, j) CCD camera, k) pc.

In this setup, shown if Fig. 5.2, the LP660-SF2 few-mode fibre was illuminated with a power of 38 mW, and the SDE1024n Spatial Light Modulator (SLM) played a crucial role in optical computing. The light travelled a distance of 2 metres through free space, passing through a pinhole, a $4f$ optical system, and various mirrors strategically positioned to guide the light onto the fibre, whether it be multi-mode or few-mode. The coupling of free-space optical transmission to the fibre was meticulously controlled using a three-axis stage (Thorlabs MBT616D/M).

To induce bends in the fibre, a 5 mm diametre bar was gently applied to it, and this bar was mounted with a low-drag ball bearing to prevent any torsion on the fibre. The fibre itself was supported by memory foam, which included a hand made channel designed to restrict bending to specific locations where it was intentionally induced. This bending bar was affixed to a linear translation stage (Thorlabs LTs300/M), ensuring repeatable and precise bending adjustments as shown in Fig. 5.3.
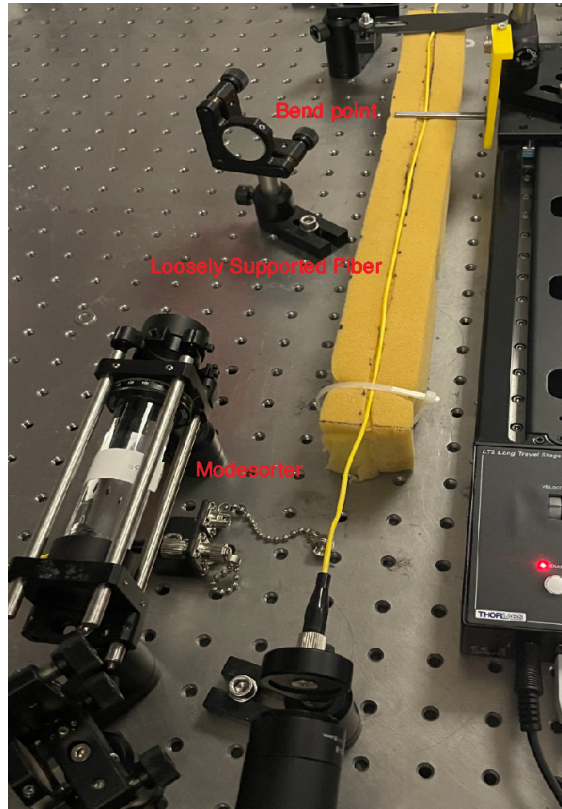
Figure 5.3: An illustration of the experimental setup features the fiber loosely supported, the mode-sorter apparatus, and the adjustable bend position.

Thanks to the incorporation of a mode sorter into the optical setup, the behaviour of fibers (multi-mode and few-mode) when subjected to pressure and subsequent bending was investigated using machine learning algorithms, particularly the SVM, although other classification methods like the decision tree were also tested. The mode sorter is an optical method capable of determining the linear superposition of orthogonal modes. When light beams carrying OAM are coupled into the fibers, inter-modal coupling phenomena occur. The interaction between different modes results in a unique power distribution at the de-multiplexer's output, which can be employed for training a machine learning algorithm; the result of which is a confusion matrix.

If we had only analysed the raw data output directly from the fiber, the effectiveness would have been significantly reduced. The mode sorter is essential for clarifying the

linear superposition of orthogonal modes, which is critical for accurately characterising fiber behaviour. Without it, the raw data would lack the clarity and resolution needed to identify specific mode interactions and power distributions, making it challenging to train the machine learning algorithms effectively and achieve precise results in the confusion matrix. The task of the confusion matrix is to graphically provide a visual representation of the statistical analysis of classification. It is composed of rows and columns, where the rows contain the actual values, and the columns contain the predicted values. A diagonal line is formed, and the more pronounced (higher values) it is, the higher the accuracy, making it easy to understand. Below is an example: in Figure A, a confusion matrix with poor results is depicted, whereas in Figure B, a matrix representing optimal accuracy (100%) is shown.
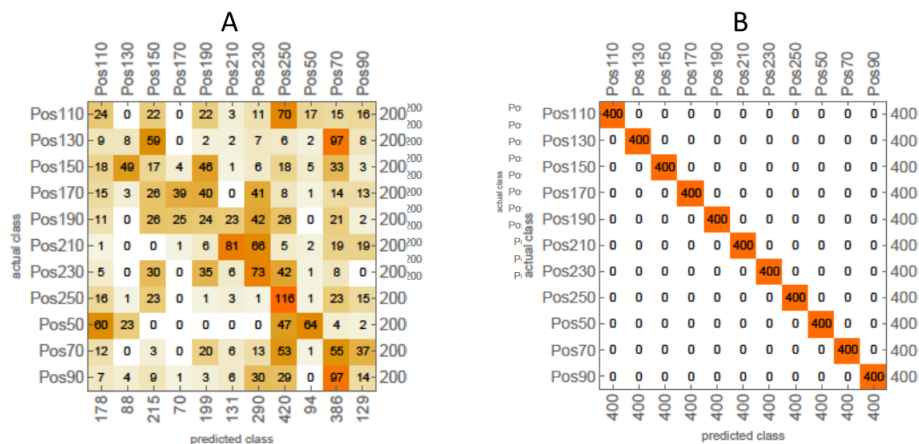
Figure 5.4: Example of two confusion matrices. A) Matrix with unclear results and an indistinct diagonal. B) Perfect matrix.

Changes in temperature and strain in the fibre lead to the intensity profile continually evolving over time, therefore making it difficult to determine explicit external environmental factors that create a particular output intensity or phase profile. This dynamic behaviour presents challenges for the use of multi-mode fibres in communications, imaging, or entangled quantum systems.

After leaving the fibre, the light encountered mirrors that directed it into the mode

sorter, and from there, it proceeded to reach the CCD camera (Imaging Source Skyris). The radius of curvature was controlled by altering the height of the bar, which induced bends in the fibre. Each bend position and radius was recorded 100 times.

5.3 Experiments conducted and curvature creation

The setup comprises a 50 mm thick piece of memory foam with a contour designed to accommodate the fibre. Subsequently, a 5 mm diametre metal bar, connected to a ball bearing, is positioned on the fibre and presses on it. This process induces curvature in the fibre itself, which varies depending on the final height of the metal bar. The method of fitting a circle to a group of points is employed for calculating the degrees of the curve, as it provides the most accurate approximation for determining the curvature.

To find the curvature, we use the following geometry:

$$R = \frac{r^2 + \left(\frac{\Delta h}{2}\right)^2}{2 \cdot \frac{\Delta h}{2}} \tag{5.1}$$

Where:

$$r = 2.5 \quad \text{(radius of the bar)} \tag{5.2}$$

$$\Delta h = 2 \quad \text{(compression height)} \tag{5.3}$$

Substituting the values:

$$R = \frac{2.5^2 + (1)^2}{2 \cdot 1} = \frac{6.25 + 1}{2} = \frac{7.25}{2} = 3.625\,\text{mm} \tag{5.4}$$

To find the angle of curvature, we use:

$$\theta \approx 2 \cdot \arcsin\left(\frac{\Delta h}{2r}\right) \tag{5.5}$$

Substituting the values:

$$\theta \approx 2 \cdot \arcsin\left(\frac{1}{2.5}\right) \approx 2 \cdot 0.3805 \, \text{radians} \approx 0.761 \, \text{radians} \tag{5.6}$$

Converting to degrees:

$$\theta(\text{degrees}) = 0.761 \times \frac{180}{\pi} \approx 38.6° \tag{5.7}$$

Therefore, the angle of curvature induced in the fibre by the metal bar and the memory foam compression is approximately 38.6°.

The following table displays the heights at which the metal bar has been positioned and the corresponding radii of curvature:

Memory foam height	Radius of curvature
48	38.7
45	63.4
43	70.3
40	76

Table 5.1: Final height of the memory foam and its corresponding curvature angle expressed in degrees.

Below is an explanatory and schematic image of the memory foam (in yellow), the fibre (in red), and the metal bar (in dark grey) both before (a) and after (b) the application of pressure. Section c, on the other hand, provides an enlargement with the respective measurements and the general formula for calculating the radii of curvature. In the formula, there is a 90-degree angle, one cathetus measuring 2.5 mm (the radius of the metal bar), and another cathetus measuring 2 mm (how much the bar has "compressed" the fibre onto the memory foam, h_f).
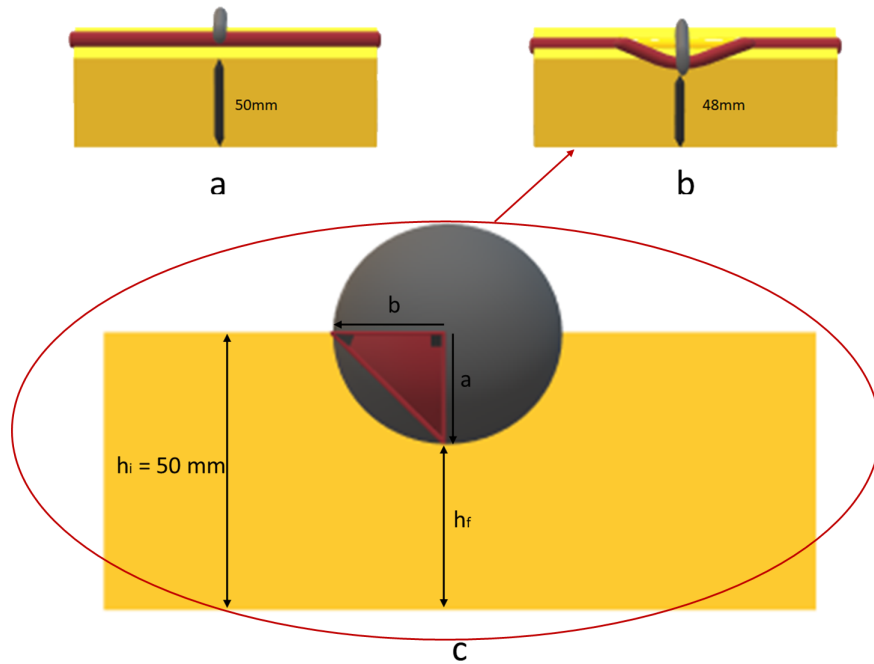
Figure 5.5: Visual representation of the optical fibre curvature, featuring the memory foam support (in yellow), the fibre (in red), and the metal bar (in grey). In situation (a), the fibre initially exhibits a natural curve, with the memory foam's height being 50 mm. In situation (b), following the addition of the metal bar, the height of the memory foam decreases to 48 mm. c) image magnification of b.

For each of these heights, 10 separate tests were carried out. Each test consisted of 11 different positions, with distances of 20, 10, 15, 10, 5, and 1 mm between them. At each position, various OAM modes (superposition and pure mode) were examined, and 100 images were captured for each mode. These images were subsequently transformed into strings called spectra.

The reason why each experiment was repeated 10 times is to obtain a comprehensive understanding of the fiber's behaviour as temperature and strain change, as shown in Fig. 5.6A displays selected distributions from a single data set, showcasing a slight variation in the weighting of the normalised power distribution with different bend positions. Analysing the power distribution of OAM commonly involves determining the center of mass (COM) [187]. Since this distribution may undergo slight variations over time or

with repeated changes in bend conditions, the average and standard deviation of the COM were computed for all 1000 distributions measured for both few- and multi-mode fiber, as depicted in Fig. 5.6B.
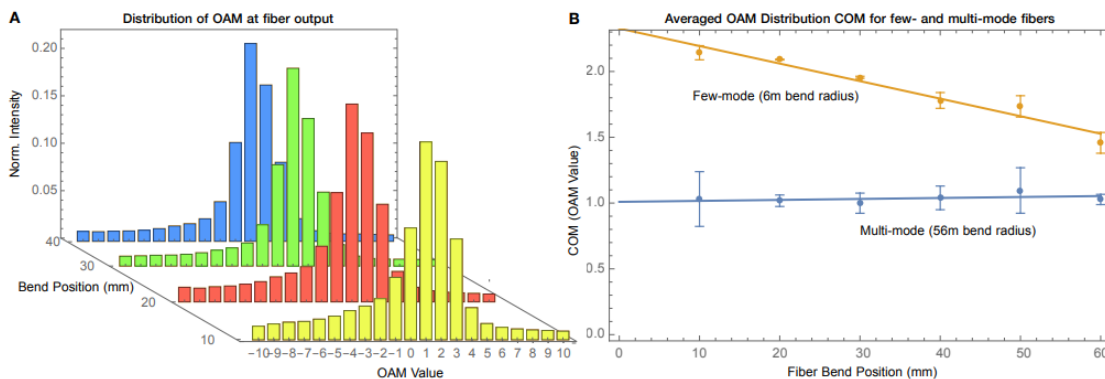
Figure 5.6: a) For an LG0,l=2 mode coupled into the fiber, a subtle change in power distribution was observed with a change in bend position. b) Analysing the data showed a continuous change in the center of mass (COM) for both few- and multi-mode fibers.

5.4 Metrics used in Machine Learning for fiber bend sensing

In the machine learning analysis conducted on fiber bend sensing, the primary metric used to evaluate the model's performance is accuracy. **Accuracy** is a measure of how well the model performs in correctly identifying the positions or curvatures of the fiber. It represents the ratio of correct predictions to the total number of predictions made by the model. The formula for accuracy is:

$$Accuracy = (\frac{Number\ of\ correct\ prediction}{Total\ prediction}) * 100 \tag{5.8}$$

This metric gives a straightforward indication of the model's overall performance, with a higher accuracy reflecting fewer errors in classification.

5.5 Results

In this section only the most prominent results will be displayed, specifically the superposition of OAM mode ± 1 and the pure mode ranging from -1 to +1, due to the large number of images generated for all experiments. The remaining results, including pure modes from -3 to +3 and the superposition of 0, 2, and 3 are presented as graph.

5.5.1 Misalignment

One of the crucial steps in this type of experiment involves the challenges of accurately collimating the light beam within the fibre. To truly understand the impact of these changes, misalignment experiments at various radii were conducted. These experiments were performed on a few-mode fibre of 38.7 degrees with 20 mm steps. The experiments were conducted by starting from a proper alignment using the same setup shown before (Fig. 5.2) and then moving the microscope with the fibre attached by several micrometres (from 2 to 9 µm). Data were captured and compiled into a single graph (Fig. 5.7) where the colours in the legend represent the different OAM pure modes (pm) and the accuracy.

Subsequently, the results of the misalignment are presented in graphical form. As it can be observed in Fig. 5.4, the further the alignment deviates from the correct one, the more inaccurate and confusing the results tend to be. However, it is worth noting that there is a consistent behaviour among the superpositions at all levels of misalignment. In particular, all the superpositions move uniformly, increasing or decreasing in accuracy consistently with each other.
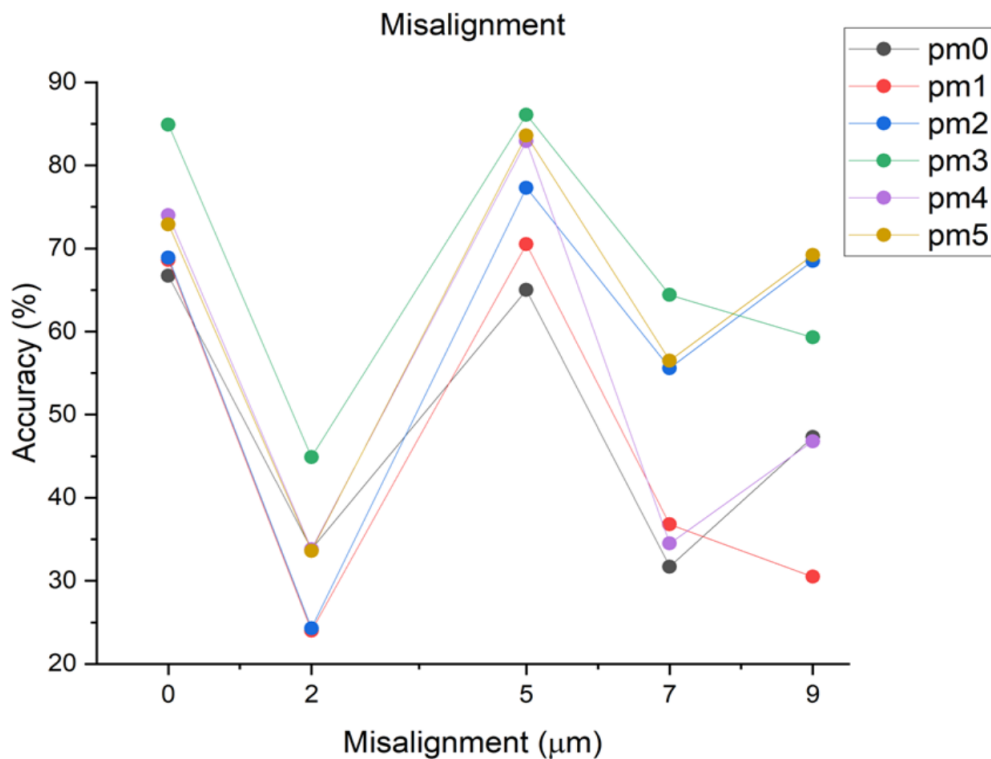
Figure 5.7: The importance of proper alignment

5.5.2 Multi-mode fibre

With regard to the Thorlabs M14L fibre, various analyses have been conducted, including different radius of curvature (38.7, 63.4, 70.3, and 76) and various step sizes, to understand the extent to which the Machine Learning algorithm could discern the actual distance between measurements and with what level of accuracy. These experiments were carried out for both superposition (ranging from 0 to 3) and pure mode (from OAM -4 to 0).

Below, some examples of the confusion matrixes obtained are provided, while the complete results, for both accuracy and weighted distance error, are attached in graphical and table form to present the data more compactly.
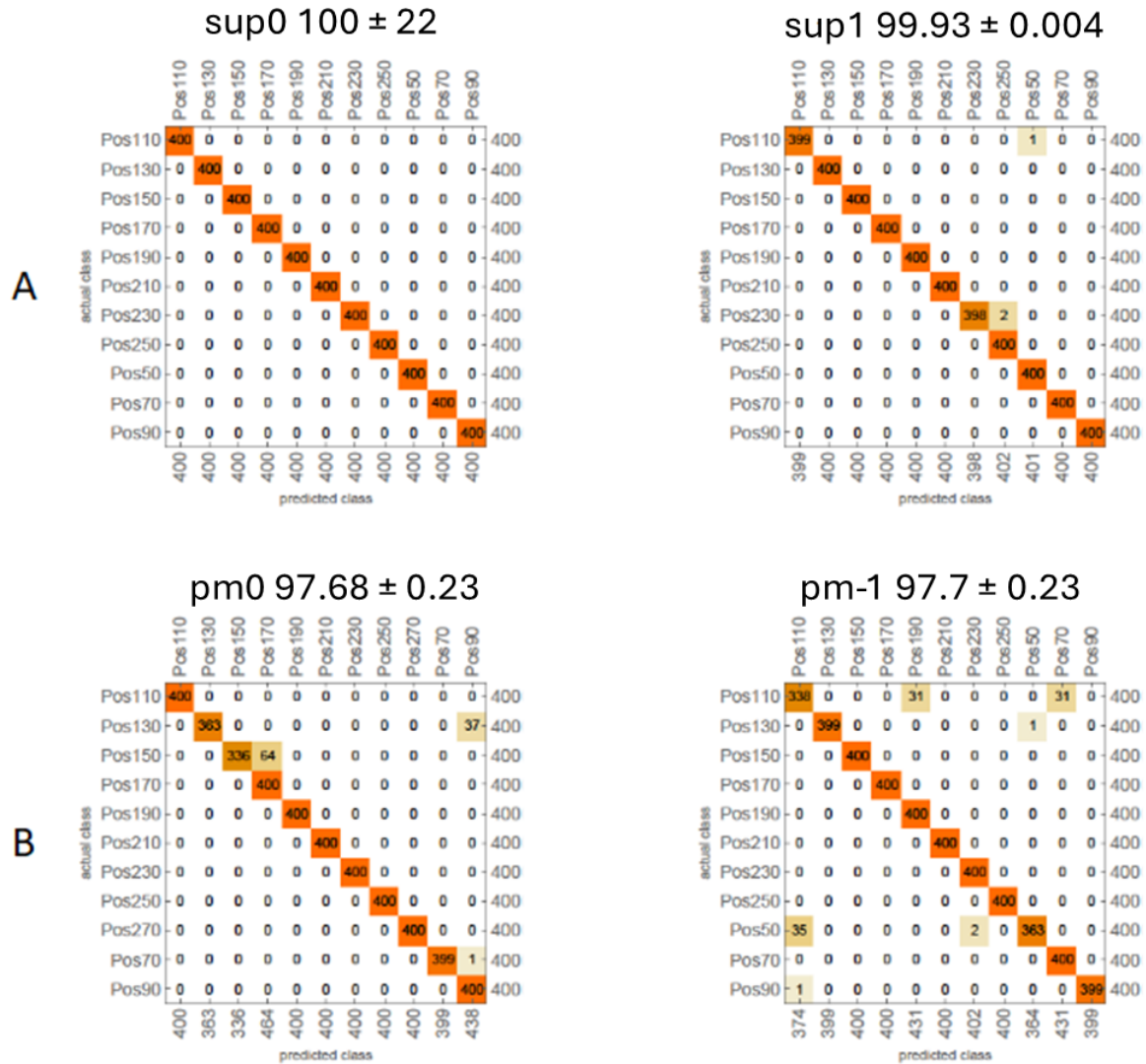
Figure 5.8: Results of the MM fibres at 38.6 ^{o} with a 20 mm step. A) superposition OAM 0 and 1, B) OAM pure mode 0 and -1.

In particular, Fig. 5.8A shows the OAM superposition of 0 (confused matrix on the left) and 1 (confused matrix on the right), while part B shows the pure OAM mode for 0 and -1.

Figure 5.9: Accuracy vs steps at 38.7 degree (multi-mode fibre pure mode.)

Figure 5.10: Accuracy vs steps at 38.7 degree (multi-mode fibre superposition.)

**Accuracy vs curvature at 20 mm step
(multi-mode fiber pure mode)**
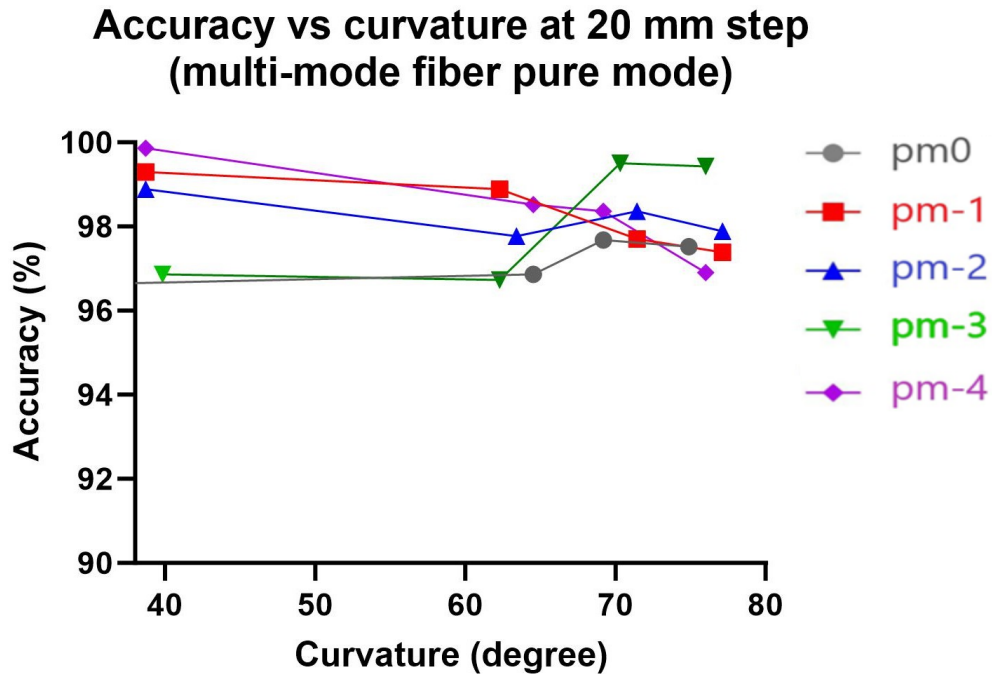
Figure 5.11: Accuracy vs curvature at 20 mm step (multi-mode fibre pure mode.)

**Accuracy vs curvature at 20 mm step (multi-mode fiber
superposistion)**
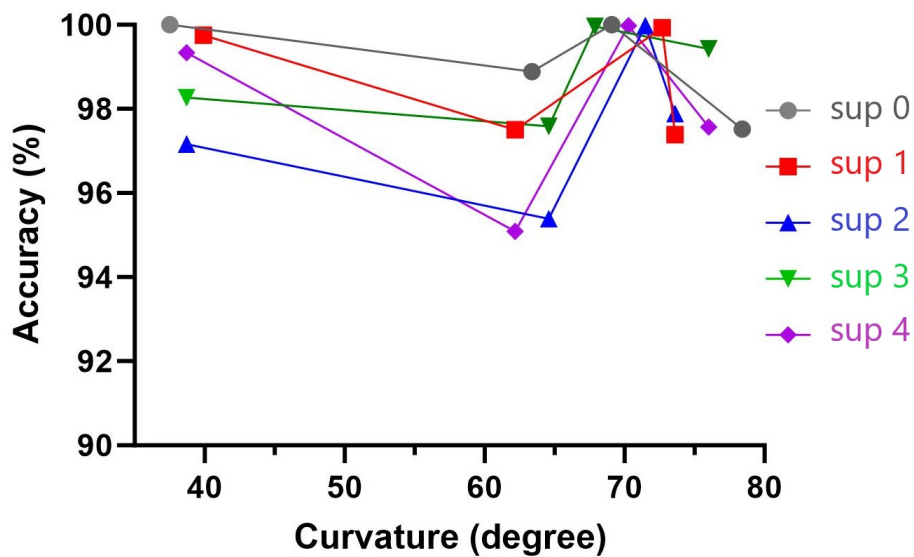
Figure 5.12: Accuracy vs radii at 20 mm step (multi-mode fibre pure mode.)

The primary findings are both promising and intriguing, with the most favourable

outcomes consistently appearing at the highest step (20 mm) for both superposition and pure mode. Remarkably, when it comes to the degrees of fibre curvature, no substantial disparities in the results are evident.

Furthermore, a notable aspect of the study is the absence of discernible differences in the fibre's behaviour between the various OAM modes examined, such as superposition 1,-1 and OAM pure mode -1. This uniformity in behaviour across different modes serves as a compelling validation of the algorithm's robustness and the effectiveness of the alignment process. If there were issues with either parametre, the results would differ, and the data would be unusable.

5.5.3   Few-mode fibre

The chosen fibre for this study was the 8.2 μm core few-mode fibre SMF28 by Thorlabs, commonly used as a single-mode fibre at 1550 nm, while at 660 nm (the wavelength used in the experiments), it behaves as a few-mode fibre. Almost the same experiments as those conducted on the multi-mode fibres were performed on this one, with a few additional bends to provide a more comprehensive understanding of its behaviour. In this case as well, some representative experiments will be presented, while others will be available for review in the appendix. In this experimental implementation we utilise a step index fibre with a core size of 8.2 μm (SMF28) and couple in light from a laser of wavelength 660 nm. At this wavelength, the fibre will support multiple modes and can be considered a few-mode optical fibre.

As with the multi-mode fibers, below, some confusion matrices are displayed to illustrate the data obtained from a single experiment, while the rest of the results are presented in the form of graphs to make all the findings more concise and reader-friendly. The results are divided into four graphs because they represent four different experiments and cannot be combined into a single graph.
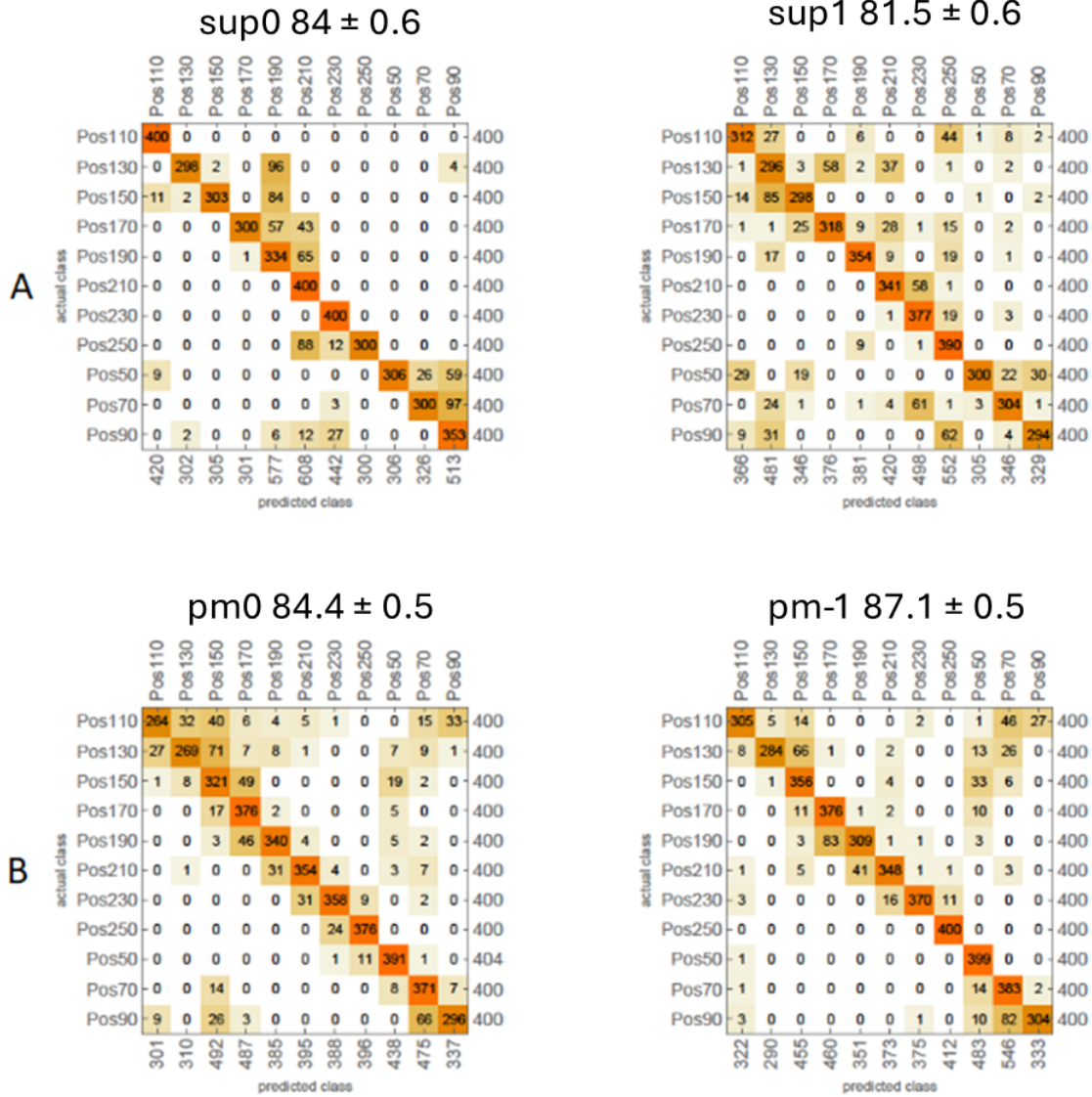
Figure 5.13: Results of the FM fibres at the smallest curvature with a 20 mm step. A) superposition OAM 0 and 1, B) OAM 0 and -1.
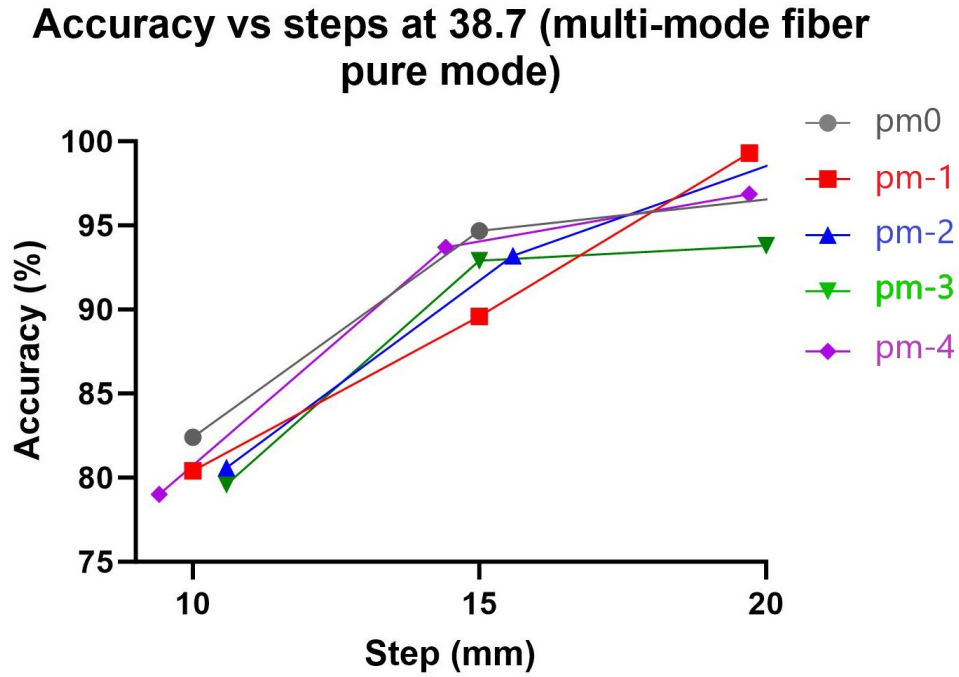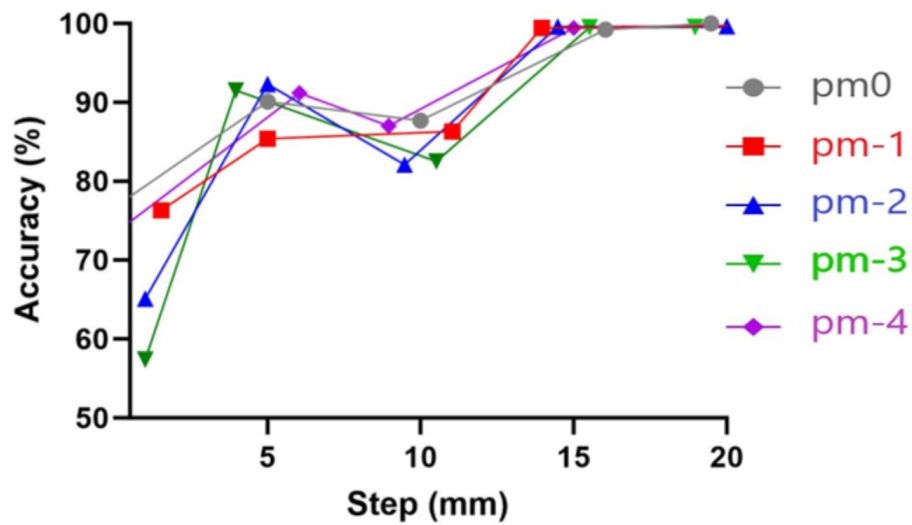
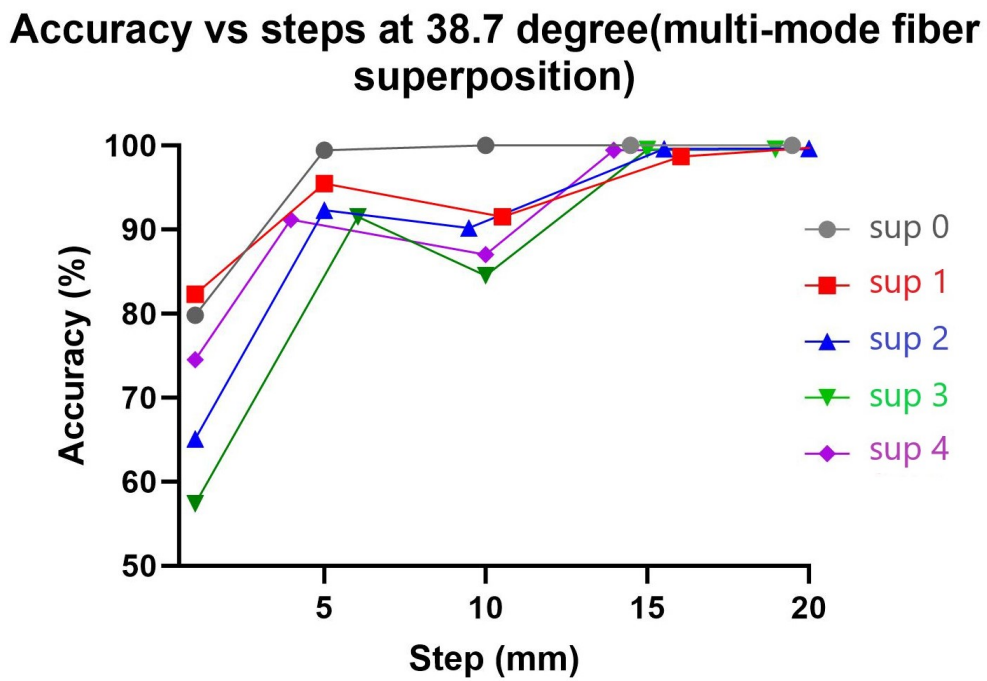Figure 5.14: Accuracy vs steps at 38.7 degree few-mode fibre pure mode.
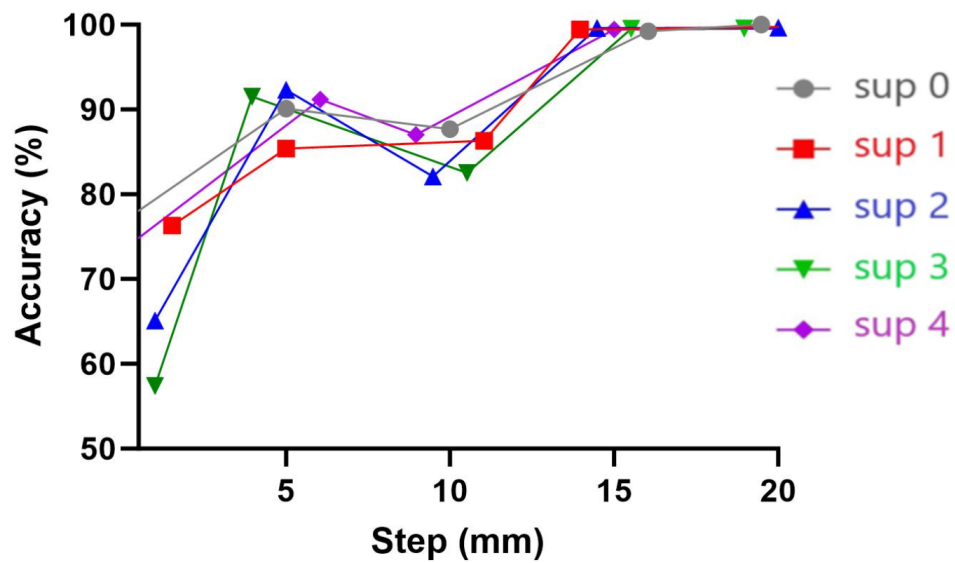
Figure 5.15: Accuracy vs steps at 38.7 degree few-mode fibre superposition.
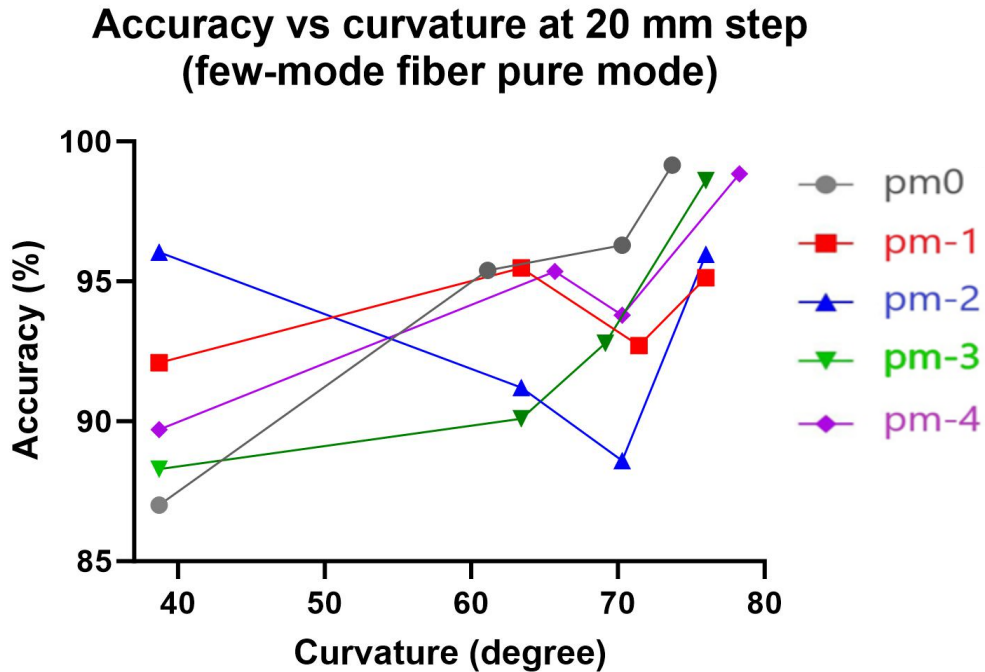
Figure 5.16: Accuracy vs curvature at 20 mm step few-mode fibre pure mode.
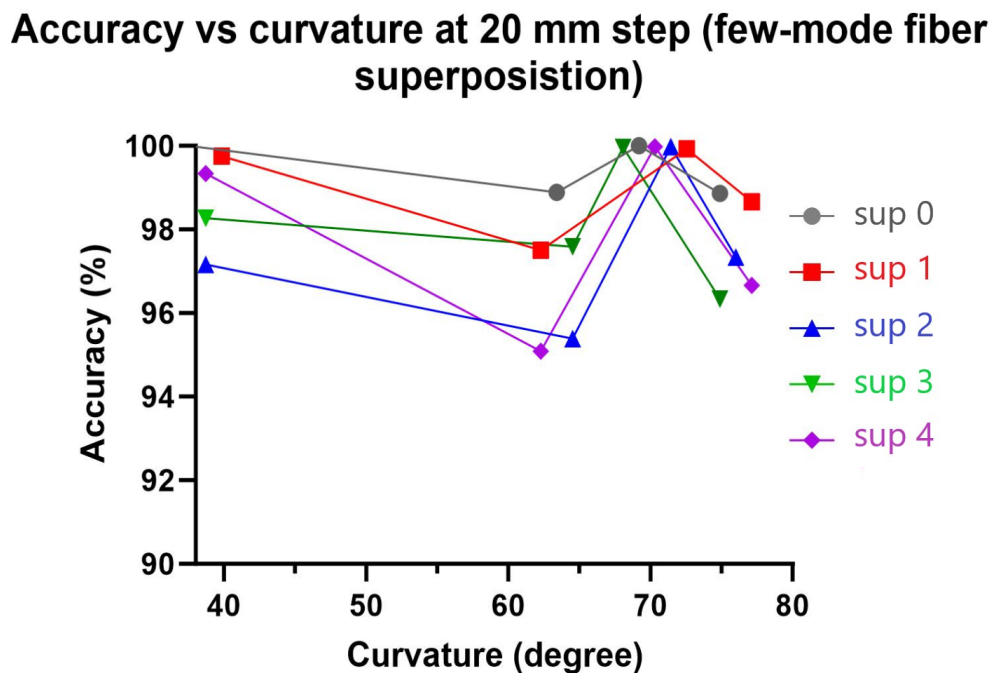
Figure 5.17: Accuracy vs curvature at 20 mm step few-mode fibre superposition.

As observed with the multi-mode fiber, the results in this case are also consistent

within themselves. However, it is worth noting that at a bend of 38.7 degrees with a 10 mm step, the algorithm's accuracy diminishes. This same behaviour is evident in the multi-mode fiber. The results, while satisfactory, demonstrate an accuracy exceeding 95% in all cases where the movement step is 20 mm. The accuracy decreases proportionally as the analysis interval shortens. This could suggest the need for further refinement of the algorithm for smaller step sizes to maintain high accuracy. Implementing the algorithm effectively for such small steps might be crucial to ensure the precision and reliability of the measurements in more intricate scenarios.

5.6 Conclusion

In this study, a robust and innovative fibre bend sensor has been developed, enabling the location of bends to be determined through the inter-modal coupling induced by these bends. Sensitivity to relative phase has been reduced through modal decomposition, revealing features within the inter-modal coupling that can provide accurate information about the shape or position of bends within the fibre.

Due to the relative simplicity of this approach, systems for fibre shape sensing could be developed for a range of applications, including wearable technology for motion sensors, monitoring flexure hinges, sensing the shape of aeroplane wings and as an ODTR, offering cost-effective, time-efficient, and highly accurate results in comparison to traditional methods for examples. It should be noted that this demonstration is limited to bends in a single direction and over known fibre lengths. Recognition should be given to the fact that bends in multiple directions or over longer or shorter fibre lengths could result in errors in classification.

In this implementation, the information within relative phase changes between modes is not utilised. However, similar mode-demultiplexing approaches could be employed to

analyse statistical variations in relative phase to further enhance system sensitivity. More broadly, mode de-multiplexing combined with ML is a potentially powerful technique that could be applied to a wide range of applications, particularly in scenarios where the constant evolution in relative phase between modes can be treated as noise within the system. This includes monitoring atmospheric conditions or extracting information from environments with dense scattering.

Retraining will be required for significant changes in the system or fibre type; however, once fully trained, retraining is generally not needed for weeks to months under normal temperature fluctuations. Further investigation for extreme temperature variations, such as those encountered in aeroplane applications, would be required for the development of prototype systems. For enhanced sensitivity to multiple directions, the utilisation of multi-core fibres is recommended to measure the differential in bend state at each fibre, similar to the approach taken with customised Bragg grating fibres.

This study has demonstrated the feasibility of using machine learning to accurately identify the precise point at which curvature occurs on a millimetric scale, incorporating a mode sorter (mode de-multiplexing) into the optical setup, capable of determining the superposition that occurs between orthogonal modes.

Increasing the bend radius will lead to heightened inter-modal coupling in the fibre and will expedite coupling to other modes. However, it should be acknowledged that our current approach cannot detect bends or movements in the fibre that do not introduce changes in inter-modal coupling and relative phase shifts.

Chapter 6

Further study and experiment for sensing technology

6.1 Introduction

Given the favourable results achieved in the initial experiments, which were significant enough to justify their publication as detailed in the previous chapter, the deliberate choice was made to expand the scope of our experimentation. Initially, few-mode fibres with lengths of both 100 metres and 1 kilometre were utilised, and identical experiments to those performed on the previously discussed fibres were conducted.

Subsequently, the investigation was broadened to include the application of SMF28 by Thorlabs, with a specific emphasis on the observation of the characteristics of fibre bending. Additionally, a detailed exploration of the behaviour of SMF28 by Thorlabs was undertaken, this time incorporating a Thorlabs retro-reflector into the setup. In this context, rather than examining the usual 11 positions, the analysis was extended to encompass 30 distinct positions.

6.2   100 m and 1 km fibres

In this section, the comprehensive presentation of results related to both the 100 m and 1 km fibre experiments is delved into. It should be noted that in these cases, our approach to data acquisition and analysis deviated from our prior experiments, as a more focused strategy was adopted. Specifically, the objective was to rigorously evaluate the algorithm's performance under a finer 0.5 mm step interval while subjecting the fibres to a range of bending conditions.

In contrast to the previous reliance on confusion matrices, a graphical representation of the data was opted for. This choice was made to offer a fresh perspective on the algorithm's behaviour when confronted with varying radii of fibre bending at this finer step interval. By visualising the results graphically, the aim was to provide a more intuitive and visually informative presentation that enhances the clarity and interpretability of the data.

An important aspect of the data collection process was the commitment to consecutive data acquisition. This decision was driven by the desire to maintain data consistency and integrity, thereby mitigating the risk of misalignment due to fluctuations in humidity or temperature within the laboratory. This methodical approach ensures the reliability and accuracy of the findings, allowing meaningful insights to be drawn from the experiments.

Accuracy vs steps at 38.7 degree (100 m few-mode fiber superposition)
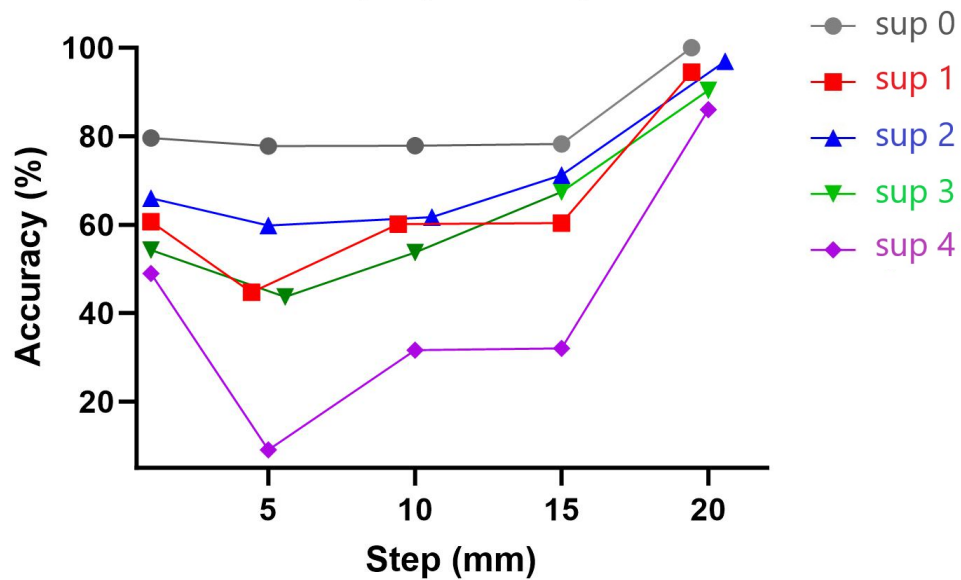
Figure 6.1: Accuracy vs step (mm) at fixed bend of a 100 m few-mode fibre

Accuracy vs curvature at 20 mm step (100 m few-mode fiber superposistion)
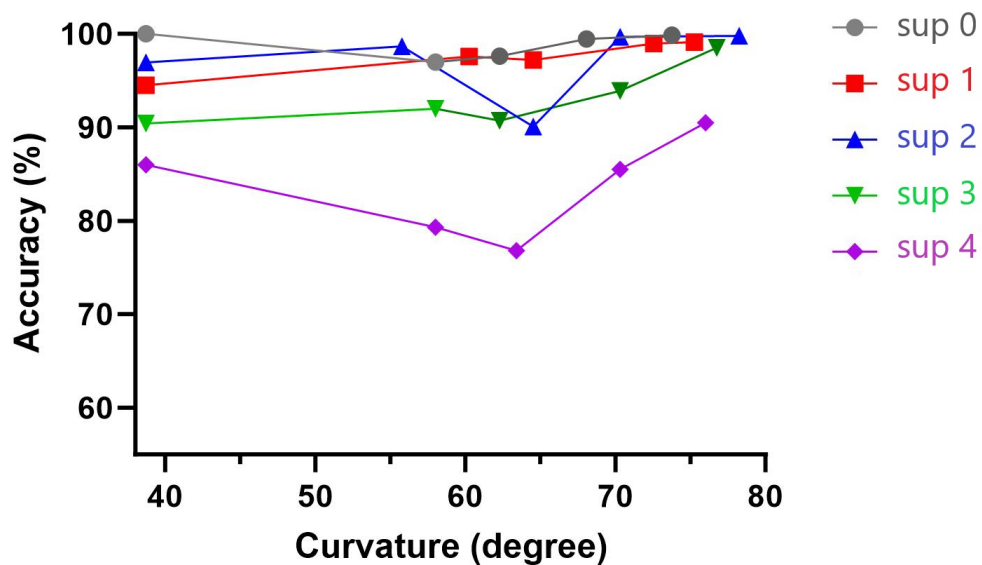
Figure 6.2: Accuracy vs different bending at 20 mm step of a 100 m few-mode fibre

Accuracy vs steps at 38.7 degree (1 km few-mode fiber superposition)
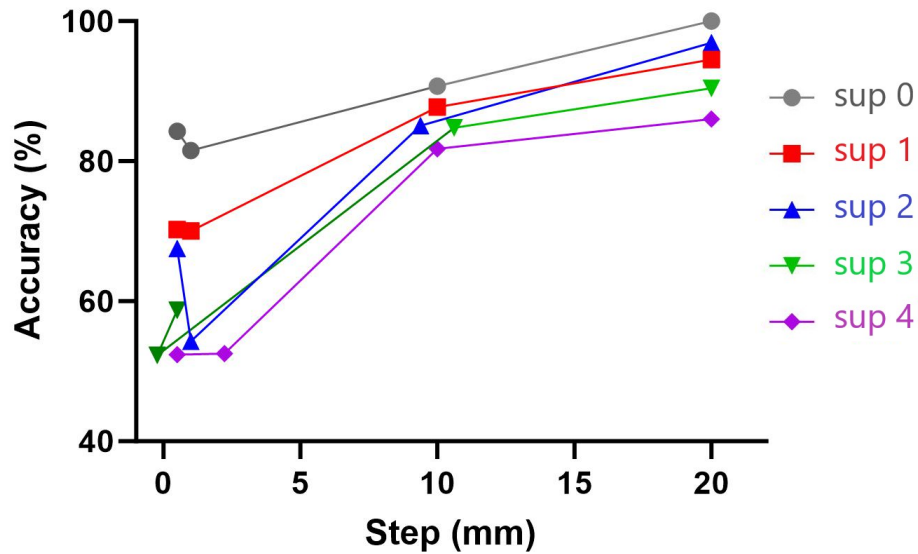
Figure 6.3: Accuracy vs step (mm) at fixed bend of a 1 km few-mode fibre

Accuracy vs curvature at 20 mm step (1 km few-mode fiber superposistion)
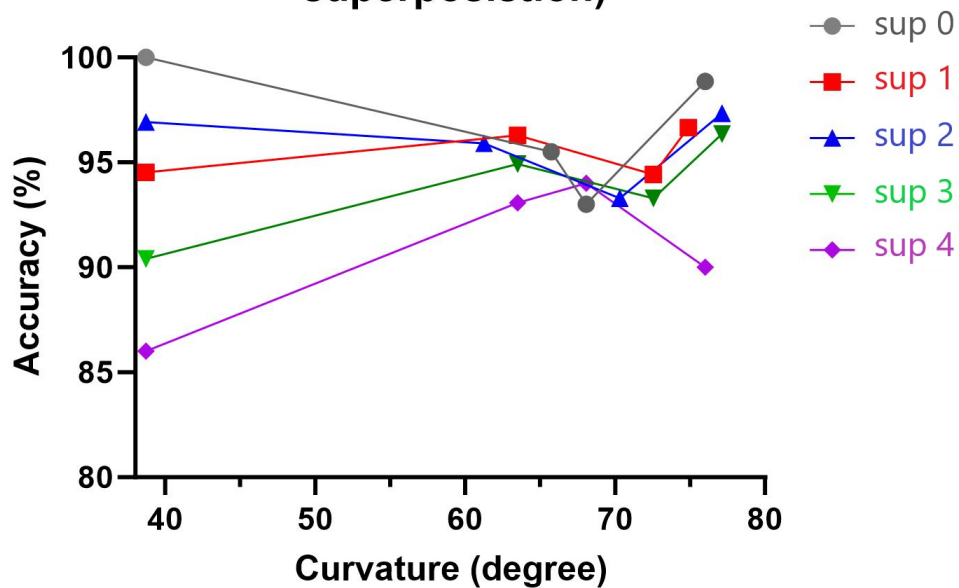
Figure 6.4: Accuracy vs different bending at fixed step of a 1 km few-mode fibre

Upon close examination of these case studies, it becomes evident that the results are,

on the whole, quite promising. Nevertheless, there is a notable deviation in the behaviour of the 100-metre fibre, which warrants further exploration.

One plausible explanation for this deviation may be associated with the specific characteristics of the fibre's length and the current state of algorithm optimization. As previously discussed in the prior chapter, it is clear that the algorithm is in need of updates and enhancements to render it more versatile and adaptable for a diverse range of applications. These findings underscore the importance of ongoing algorithm development and fine-tuning to ensure its effectiveness across various scenarios and fibre lengths.

6.3   1 m few-mode fibre

In order to provide further validation of the algorithm's functionality, a series of follow-up experiments were undertaken to explore the optical fiber's response to increased bending, which introduced a higher degree of complexity to the analysis. These experiments involved the examination of three distinct fibre positions, adding an extra layer of scrutiny to the data.

The primary objective of this experiment was to evaluate not only the algorithm's performance but also the overall stability of the process and the laboratory environment. An important aspect to highlight is that the results demonstrated a remarkable degree of consistency, remaining impervious to the passage of time during the data acquisition process. This unwavering stability in the results underscores the robustness of the algorithm and lends further confidence to its utility in practical applications.

All day 30 positions 0.5 mm step (few-mode fiber pure mode)
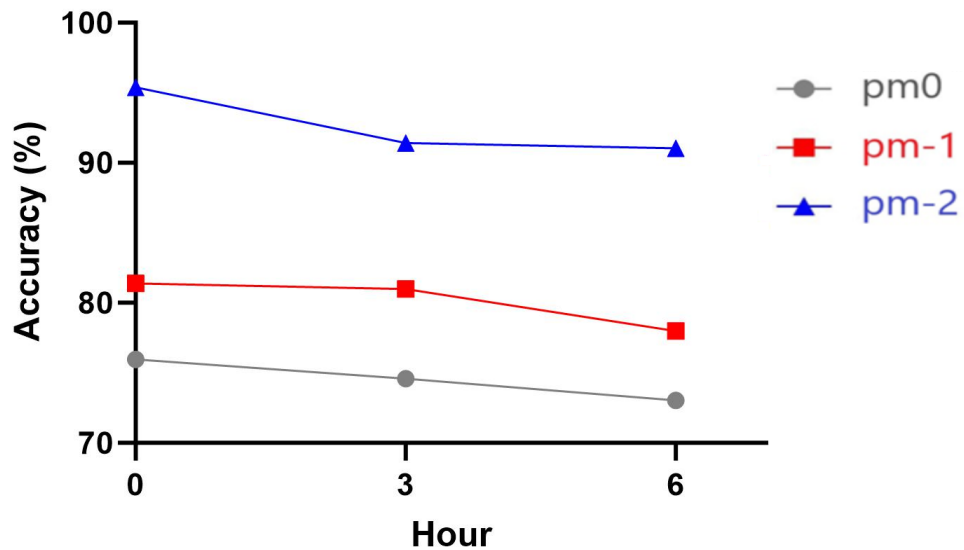
Figure 6.5: 6 hours experiment, superposition behaviour of a 1 m few-mode fibre with 0.5 mm step

All day 30 positions 1 mm step (few-mode fiber pure mode)
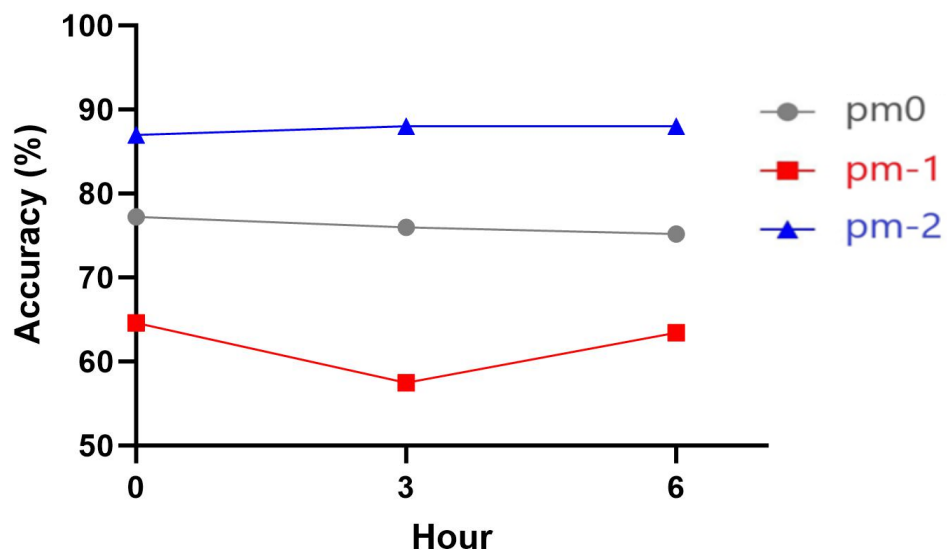
Figure 6.6: 6 hours experiment, superposition behaviour of a 1 m few-mode fibre with 1 mm step

The suboptimal results observed when using a 0.5 mm step size can be attributed to several factors. Firstly, the diminutive step size tends to induce substantial cross-talk, making it inherently challenging for the algorithm to effectively discriminate between the individual modes. Additionally, this issue may arise because the spectra generated at such small step intervals bear a striking resemblance to each other, and the algorithm is not fine-tuned for handling such minute variations.

Conversely, the experiments carried out with a 1 mm step size reaffirm the effectiveness of both the alignment process and the algorithm. The results at this step indicate a more optimal balance between data granularity and the algorithm's capabilities, which in turn contributes to a higher level of accuracy and reliability in mode differentiation.

The 1 mm step size results in stable accuracy across the different modes, indicating that the algorithm performs well with this step size, maintaining its ability to differentiate between modes effectively. The 0.5 mm step size results in declining accuracy over time for all modes, indicating that the algorithm struggles more with this finer step size, likely due to increased cross-talk and spectral similarity. The series of experiments confirm that the algorithm performs optimally with a 1 mm step size, balancing data granularity and accuracy. The stability and consistency observed with this step size validate the algorithm's functionality and robustness. Conversely, the suboptimal results with the 0.5 mm step size highlight the challenges posed by finer step intervals, emphasising the importance of choosing an appropriate step size for accurate mode differentiation in optical fibers.

6.4 Back reflection

A retroreflector, also known as a retroreflector or corner-cube prism, is an optical device that reflects light or other forms of electromagnetic radiation back to its source,

regardless of the angle at which the radiation hits the device. Retroreflectors are designed in a way that the incident light is reflected back in the direction it came from. This property makes them particularly useful for applications like surveying, vehicle headlights, and various optical measurement systems. Retroreflectors are commonly used in road signs, where they enhance the visibility of signs to drivers at night by reflecting the light from their headlights directly back towards the drivers [188].
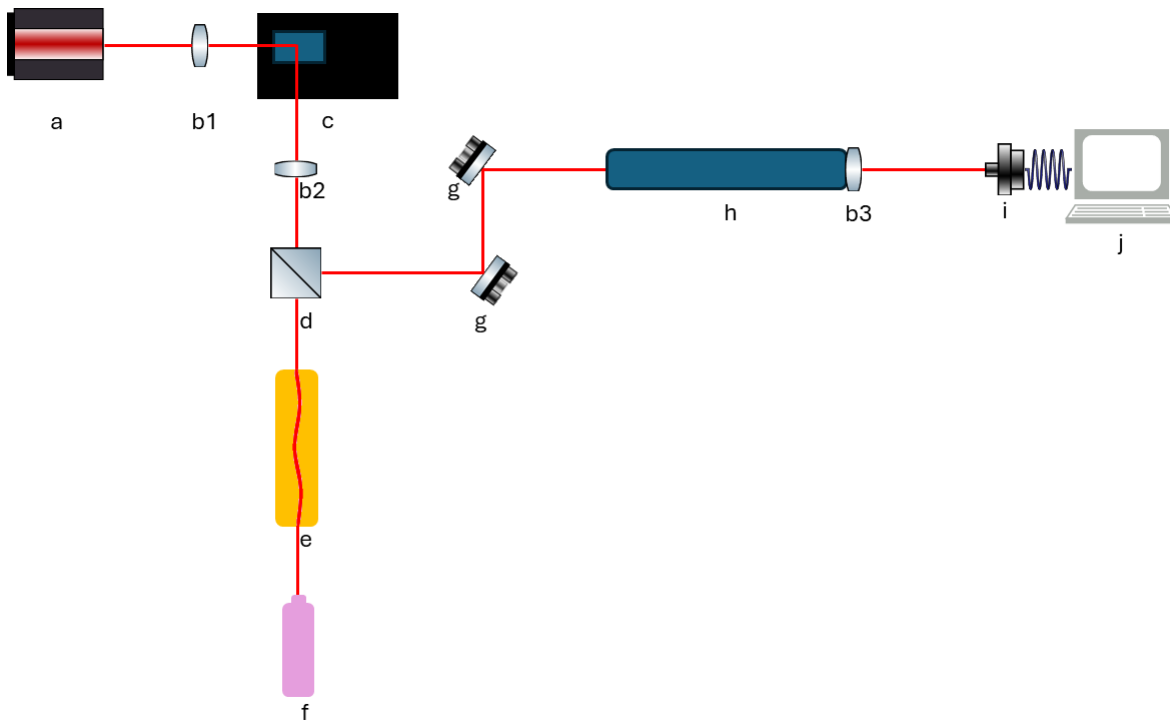
Figure 6.7: Schematic representation of the optical table. a) laser source, b) lens, c) SLM, d) beam splitter, e)Thorlabs LTs300/M stage and memory foam, f) retroreflector, g) mode sorter, i) CCD camera, j) pc.

In this experimental configuration, the LP660-SF2 few-mode fibre was illuminated with a laser power of 38 mW, while the SDE1024n SLM played a pivotal role in the optical computing process. The light traversed a 2-metre path through free space, which included passing through a pinhole, a $4f$ optical system, and various strategically positioned mirrors, all meticulously aligned to precisely direct the light onto the fibre. The

entire process of coupling free-space optical transmission to the fibre was meticulously managed using a three-axis stage (Thorlabs MBT616D/M).

Upon exiting the fibre, the light was guided toward a retroreflector and then redirected back towards the fibre, ultimately reaching the beam splitter. From there, it was channelled through a series of mirrors, leading to the mode sorter and, ultimately, the camera. Data acquisition and storage in the camera followed the same procedure as described in the experiments outlined in the previous chapter.

As in the previous chapter, in this case, several OAM modes were analyzed: pure modes from -3 to +3 and superpositions. However, only the smallest curvature radius (38.7) was analysed at various step intervals due to the project nearing its end and the impossibility of implementing further experiments.

As can be observed from the graphs, the accuracy increases with the increase in the distance between the analysis steps, which is consistent with those obtained in all previous experiments, and it drops dramatically at the step of 0.01 mm.

Figure 6.8: Accuracy vs step at fixed bend of 1 m few-mode fibre pure mode.

Accuracy vs step at 38.7 degree (1 m few-mode fiber)
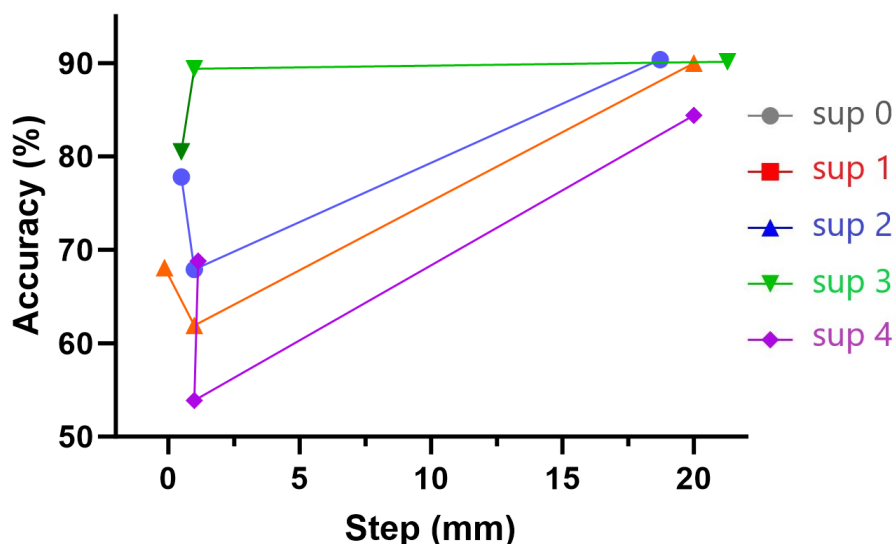
Figure 6.9: Accuracy vs step at fixed bend of 1 m few-mode fibre superposition.

The graphs indicate that the accuracy for various OAM modes, both pure and super-position, tends to increase as the step size increases, with most modes showing a rise in accuracy at larger step sizes. This suggests that larger step sizes provide more distinguishable spectra, allowing the algorithm to differentiate between modes more effectively, resulting in higher accuracy. Conversely, smaller step sizes show lower accuracy due to increased spectral similarity and cross-talk. The experimental results confirm that increasing the distance between analysis steps leads to higher accuracy in both pure and superposition OAM modes, reinforcing the importance of choosing appropriate step sizes to ensure effective mode differentiation in optical fibers. While it is true that normalisation can help account for smaller step sizes, the issue here extends beyond simple normalisation.

The core challenge with smaller step sizes, such as 0.01 mm, lies in the increased spectral similarity and cross-talk between the modes. When the step size is too small, the spectra generated at these intervals are very similar to each other, making it inherently

difficult for the algorithm to distinguish between the different modes. This results in lower accuracy because the algorithm is not fine-tuned to handle such minute variations. Normalising the data alone cannot fully compensate for the fundamental limitations imposed by the increased spectral overlap and cross-talk at smaller step sizes. Therefore, while normalisation is an important aspect, the primary factor affecting accuracy in this context is the inherent difficulty in mode differentiation due to the small step size.

6.5 Conclusion

As evidenced by the experiments conducted, the algorithm exhibits robust performance, even when subjected to similar fibre bending profiles and relatively close distances. Nevertheless, a notable decrease in accuracy becomes evident when dealing with relatively large OAM modes, such as ±4. This decline in accuracy can be attributed to the fact that the experiments were carried out using a multimode fibre at 1550 nm, which effectively behaves as a few-mode fibre at 660 nm, the wavelength employed for all experiments. This discrepancy highlights the necessity of specialised fibers tailored to support a broader range of diverse OAM modes for optimal algorithm performance in such scenarios.

An additional noteworthy observation stemming from these results is the remarkable consistency in alignment and outcomes, even when measurements are spaced hours apart. This observation underscores the stability and reliability of the experimental setup, further strengthening our confidence in the algorithm's performance.

Moreover, the conclusions drawn in this chapter align with and reinforce the insights obtained from the analyses performed on different fibers, bending profiles, and step variations in the previous chapter. This comprehensive approach to experimentation and

analysis collectively contributes to a more robust understanding of the algorithm's capabilities and limitations.

Chapter 7

Conclusion

In conclusion, a comprehensive journey through the world of metasurfaces has been undertaken, encompassing the exploration of their fundamental principles, practical applications, and the fabrication methods required for their realization. Furthermore, a detailed account of the fabrication process of the MPLC device has been presented, with each critical step supported by accompanying images that validate the precision of our approach. While the initial results indicate that the MPLC functions satisfactorily, it is evident that further analyses and optimizations are required to unlock its full potential.

The promise of versatile applications spanning various sectors, from the potential amplification of signals in telecommunications to contributions to energy-related fibre sensing technology, is held by the MPLC device. Relevance is also found in the medical and biological domains, such as in the field of flow cytometry [189]. The relatively cost-effective nature of the technology has drawn the attention of the scientific community, making it an emerging technology of great interest. The potential transition to innovative manufacturing approaches, such as pattern printing, could significantly reduce production costs and pave the way for further advancements.

159

In the course of this study, a robust and innovative fibre bend sensor has been developed, capable of precisely locating bends through the inter-modal coupling they induce. By employing modal decomposition, sensitivity to relative phase has been reduced, unearthing features within inter-modal coupling that provide accurate information about the shape or position of bends within the fibre.

The simplicity of this approach offers the potential for developing systems for fibre shape sensing across various applications. Whether for wearable technology, motion sensors, monitoring flexure hinges, or sensing the shape of airplane wings, cost-effectiveness, time-efficiency, and high accuracy compared to traditional methods are offered by our approach. However, it's essential to acknowledge that our current demonstration is limited to bends in a single direction and over known fibre lengths. Recognizing that bends in multiple directions or over longer/shorter fibre lengths may introduce errors in classification is crucial.

In this implementation, the information within relative phase changes between modes has not been leveraged. Nevertheless, similar mode-demultiplexing approaches could enhance system sensitivity by analyzing statistical variations in relative phase. More broadly, combining mode de-multiplexing with machine learning holds the potential for powerful applications, particularly in scenarios where constant variations in relative phase between modes can be treated as noise within the system, such as monitoring atmospheric conditions or extracting information from environments with dense scattering.

For the practical deployment of the system, retraining will be required in cases of significant changes in the system or fibre type. However, once fully trained, retraining typically isn't needed for weeks to months under normal temperature fluctuations. Further research is warranted to explore extreme temperature variations encountered in applications like aviation. To enhance sensitivity to multiple directions, the use of multi-core fibres is recommended to measure the differential bend state at each fibre, akin to

the approach employed with custom Bragg grating fibres.

In summary, the feasibility of utilizing machine learning to accurately pinpoint curvature on a millimetric scale has been demonstrated by incorporating a mode sorter (mode de-multiplexing) into the optical setup, enabling the determination of the superposition that occurs between orthogonal modes. Increasing the bend radius heightens inter-modal coupling in the fibre and expedites coupling to other modes. However, it's important to acknowledge that our current approach can't detect bends or movements in the fibre that don't introduce changes in inter-modal coupling and relative phase shifts.

As evidenced by our experiments, robust performance is exhibited by the algorithm, even when subjected to similar fibre bending profiles and relatively close distances. However, a notable decrease in accuracy becomes evident when dealing with relatively large OAM modes, such as ± 4. This decline can be attributed to the fact that the experiments were conducted using a multimode fibre at 1550 nm, which effectively behaves as a few-mode fibre at 660 nm, the wavelength employed for all experiments. This highlights the necessity of specialized fibres tailored to support a broader range of diverse OAM modes for optimal algorithm performance in such scenarios.

A noteworthy observation from these results is the remarkable consistency in alignment and outcomes, even when measurements are spaced hours apart. This underscores the stability and reliability of our experimental setup, further bolstering our confidence in the algorithm's performance.

Furthermore, the conclusions drawn in this chapter harmonize with and reinforce the insights gleaned from the analyses performed on different fibres, bending profiles, and step variations in the previous chapter. A more robust understanding of the algorithm's capabilities and limitations is collectively contributed by this comprehensive approach to experimentation and analysis.

These findings represent a substantial contribution to the field, and a foundation for

further research and advancements in the realm of metasurfaces and fibre bend sensing is laid. With continued refinement and exploration, it is likely that these innovations will have a lasting impact on a wide range of applications and industries.

References

[1] R. Kumar, M. Kumar, J. S. Chohan, and S. Kumar, "Overview on metamaterial: History, types and applications," *Materials Today: Proceedings*, vol. 56, pp. 3016–3024, Jan. 2022, ISSN: 22147853. DOI: `10.1016/j.matpr.2021.11.423`.

[2] R. S. Kshetrimayum, *A brief intro to metamaterials*, Dec. 2004. DOI: `10.1109/MP.2005.1368916`.

[3] S. A. Tretyakov, *A personal view on the origins and developments of the metamaterial concept*, Jan. 2017. DOI: `10.1088/2040-8986/19/1/013002`.

[4] J. F. O'hara,] Azad, and Abul K, "A discussion on the interpretation and characterization of metafilms/metasurfaces: the two-dimensional equivalent of metamaterials," Tech. Rep. [Online]. Available: `https://www.osti.gov/biblio/960956`.

[5] "1968, Veselago-ChihWeiChang (1),"

[6] J. B. Pendry, "Ci, 42.30.Wb, 73.20.Mf, 78," Tech. Rep., 2000.

[7] D. R. Smith, W. J. Padilla, D. C. Vier, S. C. Nemat-Nasser, and S. Schultz, "Composite Medium with Simultaneously Negative Permeability and Permittivity," Tech. Rep., 2000.

[8] A. N. Lagarkov and A. K. Sarychev, "Electromagnetic properties of composites containing elongated conducting inclusions," Tech. Rep., 1996.

[9]   Z. Chen, B. Guo, Y. Yang, and C. Cheng, "Metamaterials-based enhanced energy harvesting: A review," *Physica B: Condensed Matter*, vol. 438, pp. 1–8, Apr. 2014, ISSN: 09214526. DOI: `10.1016/j.physb.2013.12.040`.

[10]   N. I. Landy, S. Sajuyigbe, J. J. Mock, D. R. Smith, and W. J. Padilla, "Perfect metamaterial absorber," *Physical Review Letters*, vol. 100, no. 20, May 2008, ISSN: 00319007. DOI: `10.1103/PhysRevLett.100.207402`.

[11]   P. Wu, K. Wei, D. Xu, M. Chen, Y. Zeng, and R. Jian, "Ultra-wideband and wide-angle perfect solar energy absorber based on titanium and silicon dioxide colloidal nanoarray structure," *Nanomaterials*, vol. 11, no. 8, Aug. 2021, ISSN: 20794991. DOI: `10.3390/nano11082040`.

[12]   H. Long, C. Shao, C. Liu, Y. Cheng, and X. Liu, "Broadband near-perfect absorption of low-frequency sound by subwavelength metasurface," *Applied Physics Letters*, vol. 115, no. 10, Sep. 2019, ISSN: 00036951. DOI: `10.1063/1.5109826`.

[13]   I. Lindell, A. H. Sihvola, S. Tretyakov, and A. Viitar, *Electromagnetic Waves in Chiral and Bi-Isotropic Media*, Artech Print on Demand, Ed. 1994, p. 332.

[14]   M. Khorasaninejad, W. T. Chen, R. C. Devlin, *et al.*, "Planar Lenses at Visible Wavelengths," Tech. Rep.

[15]   N. Yu and F. Capasso, *Flat optics with designer metasurfaces*, 2014. DOI: `10.1038/nmat3839`.

[16]   M. Rahm, D. Schurig, D. A. Roberts, S. A. Cummer, D. R. Smith, and J. B. Pendry, "Design of electromagnetic cloaks and concentrators using form-invariant coordinate transformations of Maxwell's equations," *Photonics and Nanostructures - Fundamentals and Applications*, vol. 6, no. 1, pp. 87–95, Apr. 2008, ISSN: 15694410. DOI: `10.1016/j.photonics.2007.07.013`.

[17]   P. Genevet, F. Capasso, F. Aieta, M. Khorasaninejad, and R. Devlin, "Recent advances in planar optics: from plasmonic to dielectric metasurfaces," *Optica*, vol. 4, no. 1, p. 139, Jan. 2017, ISSN: 23342536. DOI: `10.1364/optica.4.000139`.

[18]   P. Lalanne and P. Chavel, "Metalenses at visible wavelengths: past, present, perspectives," *Laser and Photonics Reviews*, vol. 11, no. 3, May 2017, ISSN: 18638899. DOI: `10.1002/lpor.201600295`.

[19]   M. Miscuglio, N. J. Borys, D. Spirito, *et al.*, "Planar Aperiodic Arrays as Metasurfaces for Optical Near-Field Patterning," *ACS Nano*, vol. 13, no. 5, pp. 5646–5654, May 2019, ISSN: 1936086X. DOI: `10.1021/acsnano.9b00821`.

[20]   G. Yoon, D. Lee, K. T. Nam, and J. Rho, "Pragmatic Metasurface Hologram at Visible Wavelength: The Balance between Diffraction Efficiency and Fabrication Compatibility," *ACS Photonics*, vol. 5, no. 5, pp. 1643–1647, May 2018, ISSN: 23304022. DOI: `10.1021/acsphotonics.7b01044`.

[21]   H. Cao, J. Y. Xu, Y. Ling, *et al.*, *Random lasers with coherent feedback*, Jan. 2003. DOI: `10.1109/JSTQE.2002.807975`.

[22]   A. Pors, O. Albrektsen, I. P. Radko, and S. I. Bozhevolnyi, "Gap plasmon-based metasurfaces for total control of reflected light," *Scientific Reports*, vol. 3, 2013, ISSN: 20452322. DOI: `10.1038/srep02155`.

[23]   N. Yu, P. Genevet, M. A. Kats, *et al.*, "Light Propagation with Phase Discontinuities: Generalized Laws of Reflection and Refraction Downloaded from," Tech. Rep. [Online]. Available: `www.sciencemag.orgSCIENCEVOLhttp://science.sciencemag.org/`.

[24]   A. Arbabi, Y. Horie, M. Bagheri, and A. Faraon, "Dielectric metasurfaces for complete control of phase and polarization with subwavelength spatial resolution

and high transmission," *Nature Nanotechnology*, vol. 10, no. 11, pp. 937–943, Nov. 2015, ISSN: 17483395. DOI: 10.1038/nnano.2015.186.

[25] W. Liu and A. E. Miroshnichenko, "Beam steering with dielectric metalattices," Oct. 2017. DOI: 10.1021/acsphotonics.7b01217. [Online]. Available: http://arxiv.org/abs/1710.03380%20http://dx.doi.org/10.1021/acsphotonics.7b01217.

[26] X. Ni, A. V. Kildishev, and V. M. Shalaev, "Metasurface holograms for visible light," *Nature Communications*, vol. 4, Nov. 2013, ISSN: 20411723. DOI: 10.1038/ncomms3807.

[27] F. Aieta, P. Genevet, M. A. Kats, *et al.*, "Aberration-free ultrathin flat lenses and axicons at telecom wavelengths based on plasmonic metasurfaces," *Nano Letters*, vol. 12, no. 9, pp. 4932–4936, Sep. 2012, ISSN: 15306984. DOI: 10.1021/nl302516v.

[28] M. Decker, I. Staude, M. Falkner, *et al.*, "High-Efficiency Dielectric Huygens' Surfaces," *Advanced Optical Materials*, vol. 3, no. 6, pp. 813–820, Jun. 2015, ISSN: 21951071. DOI: 10.1002/adom.201400584.

[29] L. V. Poulikakos, J. A. Dionne, and A. García-Etxarri, "Optical helicity and optical chirality in free space and in the presence of matter," *Symmetry*, vol. 11, no. 9, 2019, ISSN: 20738994. DOI: 10.3390/sym11091113.

[30] T. J. Cui, M. Q. Qi, X. Wan, J. Zhao, and Q. Cheng, "Coding metamaterials, digital metamaterials and programmable metamaterials," *Light: Science & Applications*, vol. 3, no. 10, e218–e218, Oct. 2014. DOI: 10.1038/lsa.2014.99.

[31] X. Wan, M. Q. Qi, T. Y. Chen, and T. J. Cui, "Field-programmable beam reconfiguring based on digitally-controlled coding metasurface," *Scientific Reports*, vol. 6, Feb. 2016, ISSN: 20452322. DOI: 10.1038/srep20663.

[32] V. Joy, A. Dileep, P. V. Abhilash, R. U. Nair, and H. Singh, *Metasurfaces for Stealth Applications: A Comprehensive Review*, Jun. 2021. DOI: `10.1007/s11664-021-08927-3`.

[33] A. A. Eteng, H. H. Goh, S. K. A. Rahim, and A. Alomainy, "A Review of Metasurfaces for Microwave Energy Transmission and Harvesting in Wireless Powered Networks," *IEEE Access*, vol. 9, pp. 27 518–27 539, 2021, ISSN: 21693536. DOI: `10.1109/ACCESS.2021.3058151`.

[34] A. A. G. Amer, S. Z. Sapuan, N. Nasimuddin, A. Alphones, and N. B. Zinal, "A comprehensive review of metasurface structures suitable for RF energy harvesting," *IEEE Access*, vol. 8, pp. 76 433–76 452, 2020, ISSN: 21693536. DOI: `10.1109/ACCESS.2020.2989516`.

[35] M. E. Badawe and O. M. Ramahi, "Efficient Metasurface Rectenna for Electromagnetic Wireless Power Transfer and Energy Harvesting," Tech. Rep., 2018, pp. 35–40.

[36] H. A. Atwater and A. Polman, *Plasmonics for improved photovoltaic devices*, Mar. 2010. DOI: `10.1038/nmat2629`.

[37] C.-C. Chang, W. J. M. Kort-Kamp, J. Nogan, *et al.*, "High-Temperature Refractory Metasurfaces for Solar Thermophotovoltaic Energy Harvesting," Tech. Rep.

[38] H. Ojukwu, B. C. Seet, and S. Ur Rehman, "Metasurface-Aided Wireless Power Transfer and Energy Harvesting for Future Wireless Networks," *IEEE Access*, vol. 10, pp. 52 431–52 450, 2022, ISSN: 21693536. DOI: `10.1109/ACCESS.2022.3170106`.

[39] G. Zheng, H. Mühlenbernd, M. Kenney, G. Li, T. Zentgraf, and S. Zhang, "Metasurface holograms reaching 80% efficiency," *Nature Nanotechnology*, vol. 10, no. 4, pp. 308–312, Apr. 2015, ISSN: 17483395. DOI: `10.1038/nnano.2015.2`.

[40] A. Andryieuski and A. V. Lavrinenko, "Graphene metamaterials based tunable ter-
      ahertz absorber: effective surface conductivity approach," *Optics Express*, vol. 21,
      no. 7, p. 9144, Apr. 2013, ISSN: 10944087. DOI: `10.1364/oe.21.009144`.

[41] C. L. Holloway, E. F. Kuester, J. A. Gordon, J. O'hara, J. Booth, and D. R.
      Smith, "An Overview of the Theory and Applications of Metasurfaces: The Two-
      Dimensional Equivalents of Metamaterials," Tech. Rep. 2, 2012.

[42] W. C. Brown, "The History of Power Transmission by Radio Waves," Tech. Rep.
      9, 1984.

[43] M. S. Bin-Alam, O. Reshef, Y. Mamchur, *et al.*, "Ultra-high-Q resonances in plas-
      monic metasurfaces," *Nature Communications*, vol. 12, no. 1, Dec. 2021, ISSN:
      20411723. DOI: `10.1038/s41467-021-21196-2`.

[44] J. R. Mejía-Salazar and O. N. Oliveira, *Plasmonic Biosensing*, Oct. 2018. DOI:
      `10.1021/acs.chemrev.8b00359`.

[45] Z. Wang, J. Chen, S. A. Khan, *et al.*, *Plasmonic metasurfaces for medical diagnosis
      applications: A review*, Jan. 2022. DOI: `10.3390/s22010133`.

[46] M. Amin, O. Siddiqui, H. Abutarboush, M. Farhat, and R. Ramzan, "A THz
      graphene metasurface for polarization selective virus sensing," *Carbon*, vol. 176,
      pp. 580–591, May 2021, ISSN: 00086223. DOI: `10.1016/j.carbon.2021.02.051`.

[47] S. Jahani and Z. Jacob, *All-dielectric metamaterials*, Jan. 2016. DOI: `10.1038/
      nnano.2015.304`.

[48] A. I. Kuznetsov, A. E. Miroshnichenko, M. L. Brongersma, Y. S. Kivshar, and
      B. Luk'yanchuk, *Optically resonant dielectric nanostructures*, Nov. 2016. DOI: `10.
      1126/science.aag2472`.

[49] D. Lin, P. Fan, E. Hasman, and M. L. Brongersma, "Dielectric gradient metasurface optical elements," *Science*, vol. 345, no. 6194, pp. 298–302, 2014, ISSN: 10959203. DOI: `10.1126/science.1253213`.

[50] R. Soref, "The past, present, and future of silicon photonics," *IEEE Journal on Selected Topics in Quantum Electronics*, vol. 12, no. 6, pp. 1678–1687, Nov. 2006, ISSN: 1077260X. DOI: `10.1109/JSTQE.2006.883151`.

[51] I. Javed, J. Kim, M. A. Naveed, *et al.*, "Broad-Band Polarization-Insensitive Metasurface Holography with a Single-Phase Map," *ACS Applied Materials and Interfaces*, vol. 14, no. 31, pp. 36 019–36 026, Aug. 2022, ISSN: 19448252. DOI: `10.1021/acsami.2c07960`.

[52] M. I. Shalaev, J. Sun, A. Tsukernik, A. Pandey, K. Nikolskiy, and N. M. Litchinitser, "High-Efficiency All-Dielectric Metasurfaces for Ultracompact Beam Manipulation in Transmission Mode," *Nano Letters*, vol. 15, no. 9, pp. 6261–6266, Sep. 2015, ISSN: 15306992. DOI: `10.1021/acs.nanolett.5b02926`.

[53] A. Silva, F. Monticone, G. Castaldi, V. Galdi, A. Alù, and N. Engheta, "Performing mathematical operations with metamaterials," *Science*, vol. 343, no. 6167, pp. 160–163, 2014, ISSN: 10959203. DOI: `10.1126/science.1242818`.

[54] D. Visser, S. B. Basuvalingam, Y. Désières, and S. Anand, "Optical properties and fabrication of dielectric metasurfaces based on amorphous silicon nanodisk arrays," *Optics Express*, vol. 27, no. 4, p. 5353, Feb. 2019, ISSN: 10944087. DOI: `10.1364/oe.27.005353`.

[55] K. Huang, Z. Dong, S. Mei, *et al.*, "Silicon multi-meta-holograms for the broadband visible light," *Laser and Photonics Reviews*, vol. 10, no. 3, pp. 500–509, May 2016, ISSN: 18638899. DOI: `10.1002/lpor.201500314`.

[56] S. Arba-Mosquera, S. Verma, and S. T. Awwad, "Theoretical effect of coma and spherical aberrations translation on refractive error and higher order aberrations," *Photonics*, vol. 7, no. 4, pp. 1–15, Dec. 2020, ISSN: 23046732. DOI: `10.3390/photonics7040116`.

[57] R. Horn, M. Rosenberger, G. Notni, A. Golomoz, R. Fütterer, and P. G. Dittrich, "Investigation on chromatic aberrations and its potential for application in depth measurement," in *Measurement: Sensors*, vol. 18, Elsevier Ltd, Dec. 2021. DOI: `10.1016/j.measen.2021.100113`.

[58] A. She, S. Zhang, S. Shian, D. R. Clarke, and F. Capasso, "A P P L I E D S C I E N C E S A N D E N G I N E E R I N G Adaptive metalenses with simultaneous electrical control of focal length, astigmatism, and shift," Tech. Rep., 2018. [Online]. Available: `https://www.science.org`.

[59] S.-W. Moon, Y. Kim, G. Yoon, and J. Rho, "iScience Review Recent Progress on Ultrathin Metalenses for Flat Optics," 2017. DOI: `10.1016/j.isci`. [Online]. Available: `https://doi.org/10.1016/j.isci.`.

[60] C. Chen, W. Song, J. W. Chen, *et al.*, "Spectral tomographic imaging with aplanatic metalens," *Light: Science and Applications*, vol. 8, no. 1, Dec. 2019, ISSN: 20477538. DOI: `10.1038/s41377-019-0208-0`.

[61] B. Wilburn, N. Joshi, V. Vaish, *et al.*, "High Performance Imaging Using Large Camera Arrays," Tech. Rep.

[62] T. Georgiev and A. Lumsdaine, "Reducing plenoptic camera artifacts," *Computer Graphics Forum*, vol. 29, no. 6, pp. 1955–1968, 2010, ISSN: 14678659. DOI: `10.1111/j.1467-8659.2010.01662.x`.

[63] P. Vabishchevich and Y. Kivshar, "Nonlinear photonics with metasurfaces," *Photonics Research*, vol. 11, no. 2, B50, Feb. 2023, ISSN: 23279125. DOI: `10.1364/prj.474387`.

[64] A. Zhan, S. Colburn, R. Trivedi, T. K. Fryett, C. M. Dodson, and A. Majumdar, "Low-Contrast Dielectric Metasurface Optics," *ACS Photonics*, vol. 3, no. 2, pp. 209–214, Feb. 2016, ISSN: 23304022. DOI: `10.1021/acsphotonics.5b00660`.

[65] F. Liu, O. Tsilipakos, X. Wang, *et al.*, "Electromagnetic Aspects of Practical Approaches to Realization of Intelligent Metasurfaces," in *2018 12th International Congress on Artificial Materials for Novel Wave Phenomena, METAMATERIALS 2018*, Institute of Electrical and Electronics Engineers Inc., Nov. 2018, pp. 260–262, ISBN: 9781538647028. DOI: `10.1109/MetaMaterials.2018.8534164`.

[66] K. Shastri and F. Monticone, "Nonlocal Flat Optics," Tech. Rep.

[67] C. G. Kibebe, Y. Liu, and J. Tang, *Harnessing optical advantages in computing: a review of current and future trends*, 2024. DOI: `10.3389/fphy.2024.1379051`.

[68] Y. Ding, Z. Luo, G. Borjigin, and S. T. Wu, "Breaking the optical efficiency limit of virtual reality with a nonreciprocal polarization rotator," *Opto-Electronic Advances*, vol. 7, no. 3, 2024, ISSN: 20964579. DOI: `10.29026/oea.2024.230178`.

[69] Z. Li, P. Lin, Y.-W. Huang, *et al.*, "Meta-optics achieves RGB-achromatic focusing for virtual reality," Tech. Rep., 2021, pp. 4458–4485.

[70] F. P. Kapron, D. B. Keck, and R. D. Maurer, "Radiation losses in glass optical waveguides," *Applied Physics Letters*, vol. 17, no. 10, pp. 423–425, 1970, ISSN: 00036951. DOI: `10.1063/1.1653255`.

[71] P. Cordier, J. C. Doukhan, E. Fertein, *et al.*, "TEM characterization of structural changes in glass associated to Bragg grating inscription in a germanosilicate optical fibre preform," Tech. Rep., 1994, pp. 269–275.

[72] K. O. Hill, Y. Fujii, D. C. Johnson, and B. S. Kawasaki, "Photosensitivity in optical fiber waveguides: Application to reflection filter fabrication," *Applied Physics Letters*, vol. 32, no. 10, pp. 647–649, May 1978, ISSN: 10773118. DOI: 10.1063/1.89881.

[73] C. Pendão and I. Silva, *Optical Fiber Sensors and Sensing Networks: Overview of the Main Principles and Applications*, Oct. 2022. DOI: 10.3390/s22197554.

[74] X. He, P. Beckett, and R. R. Unnithan, "Progress in Optical Science and Photonics Multispectral Image Sensors Using Metasurfaces," Tech. Rep. [Online]. Available: https://link.springer.com/bookseries/10091.

[75] Q. Liang, T. S. Durrani, Y. Pi, and S. W. Samn, *Hybrid Wireless Sensor Networks: Theory and Design*, 2016. DOI: 10.1155/2016/8253168.

[76] V. Novotny, A. Prokeš, K. Slavicek, *et al.*, "Long-Range Optical Fiber Based Distributed Mechanical Vibration Sensing Long-Range Optical Fiber Based Distributed Mechanical Vi-bration Sensing," 2021. DOI: 10.20944/preprints202104.0514.v1. [Online]. Available: www.preprints.org.

[77] P. Nag, K. Sadani, and S. Mukherji, "Optical Fiber Sensors for Rapid Screening of COVID-19," *Transactions of the Indian National Academy of Engineering*, vol. 5, no. 2, pp. 233–236, Jun. 2020, ISSN: 2662-5415. DOI: 10.1007/s41403-020-00128-4.

[78] X. Bao and L. Chen, *Recent Progress in Distributed Fiber Optic Sensors*, Jul. 2012. DOI: 10.3390/s120708601.

[79] G. P. (P. Agrawal, *Fiber-optic communication systems.* Wiley-Interscience, 2002, p. 546, ISBN: 0471221147.

[80] D. Inaudi and B. Glisic, "Long-Range Pipeline Monitoring by Distributed Fiber Optic Sensing," *Journal of Pressure Vessel Technology*, vol. 132, no. 1, Dec. 2009, ISSN: 0094-9930. DOI: 10.1115/1.3062942. [Online]. Available: https://doi.org/10.1115/1.3062942.

[81] K. Bremer, M. Wollweber, F. Weigand, *et al.*, "Fibre Optic Sensors for the Structural Health Monitoring of Building Structures," *Procedia Technology*, vol. 26, pp. 524–529, 2016, ISSN: 22120173. DOI: 10.1016/j.protcy.2016.08.065.

[82] A. H. Hartog, "SERIES IN FIBER OPTIC SENSORS DISTRIBUTED OPTICAL FIBRE SENSORS," Tech. Rep.

[83] D. A. Krohn, T. W. MacDougall, and A. Mendez, *Fiber Optic Sensors: Fundamentals and Applications.* Society of Photo-Optical Instrumentation Engineers (SPIE), 2014. DOI: 10.1117/3.1002910.

[84] J. Homola, *Surface plasmon resonance sensors for detection of chemical and biological species*, Feb. 2008. DOI: 10.1021/cr068107d.

[85] A. Venketeswaran, N. Lalam, J. Wuenschell, *et al.*, "Recent Advances in Machine Learning for Fiber Optic Sensor Applications," *Advanced Intelligent Systems*, vol. 4, no. 1, Jan. 2022, ISSN: 2640-4567. DOI: 10.1002/aisy.202100067.

[86] "Simon Rogers, Mark Girolami A First Course in Machine Learning,"

[87] S. Angelucci, Z. Chen, L. Škvarenina, A. W. Clark, A. Vallés, and M. P. J. Lavery, "Structured light enhanced machine learning for fiber bend sensing," *Optics Express*, vol. 32, no. 5, p. 7882, Feb. 2024, ISSN: 10944087. DOI: 10.1364/oe.513829.

[88] P. Mancosu, "Acoustics and optics," in *The Cambridge History of Science: Early Modern Science*, vol. 3, Cambridge University Press, Jan. 2006, pp. 596–631, ISBN: 9781139054010. DOI: 10.1017/CHOL9780521572446.026.

[89] M. Young, "Optics_and_Lasers_including_Fibres_and_I,"

[90] J.-L. Basdevant, "Famous optician: Augustin Fresnel and the wave theory of light," *Photoniques*, pp. 18–22, Mar. 2019, ISSN: 1629-4475. DOI: `10.1051/photon/2019s418`.

[91] J. C. Maxwell, "maxwell-1997-viii-a-dynamical-theory-of-the-electromagnetic-field," [Online]. Available: `https://royalsocietypublishing.org/doi/10.1098/rstl.1865.0008`.

[92] M. Planck, "7. On the theory of the Energy Distribution Law of the Normal Spectrum 20," Tech. Rep.

[93] S. Klassen, *The Photoelectric Effect: Reconstructing the Story for the Physics Classroom*, Jul. 2011. DOI: `10.1007/s11191-009-9214-6`.

[94] D. R. Murdoch, "Niels Bohr and wave-particle duality," in *Niels Bohr's Philosophy of Physics*, Cambridge University Press, Jul. 2011, pp. 16–33. DOI: `10.1017/cbo9780511564307.004`.

[95] G. E. Cossali, "Appunti di fisica tecnica," [Online]. Available: `http://www.den.unipi.it/paolo.dimarco/eps/disp22complete.pdf`.

[96] E. Rousseau and D. Felbacq, "Detailed derivation of the generalized Snell-Descartes laws from Fermat's principle," *Journal of the Optical Society of America. A Optics*, vol. 40, no. 4, 2023. DOI: `10.1364/JOSAA.478123{\"{i}}`. [Online]. Available: `https://hal.science/hal-04073052`.

[97] X. Chen, L. Huang, H. Mühlenbernd, *et al.*, "Dual-polarity plasmonic metalens for visible light," *Nature Communications*, vol. 3, 2012, ISSN: 20411723. DOI: `10.1038/ncomms2207`.

[98] B. E. A. Saleh and M. C. Teich, "Fundamentals of Photonics," in *Fundamentals of Photonics*, Wiley, Aug. 1991. DOI: `10.1002/0471213748.fmatter{\_}indsub`.

[99] F. Pampaloni and J. Enderlein, "Gaussian, Hermite-Gaussian, and Laguerre-Gaussian beams: A primer," Tech. Rep.

[100] L. Carbone, P. Fulda, C. Bond, *et al.*, "The generation of higher-order Laguerre-Gauss optical beams for high-precision interferometry," *Journal of visualized experiments : JoVE*, no. 78, 2013, ISSN: 1940087X. DOI: `10.3791/50564`.

[101] A. E. Siegman, "Lasers,"

[102] H. Kogelnik and T. Li, "Laser Beams and Resonators," Tech. Rep.

[103] Yariv Amnon, "Quantum Electronics,"

[104] L. Allen, S. M. Barnett, and M. J. Padgett, *Optical Angular Momentum*, 1st Edition, CRC Press, Ed. Boca Raton: CRC Press, 2003, pp. -300.

[105] J.-r. Qian and W.-p. Huang, "LP Modes and Ideal Modes on Optical Fibers," Tech. Rep. 6, 1986.

[106] J. Durnin, J. J. Miceli, i. York, and J. H. Eberly, "Diffraction-Free Beams," DOI: `10.Hc`.

[107] M. W. Beijersbergen, L. Allen, H. E. L. O. Van Der Veen, and J. P. Woerdman, "OPTICS COMMUNICATIONS Astigmatic laser mode converters and transfer of orbital angular momentum," Tech. Rep., 1993, pp. 123–132.

[108] L. Allen, M. W. Beijersbergen, R. J. C. Spreeuw, and J. P. Woerdman, "Orbital angular momentum of light and the transformation of Laguerre-Gaussian laser modes," Tech. Rep., 1992.

[109] H. Poynting J., "The Wave Motion of a Revolving Shaft, and a Suggestion as to the Angular Momentum in a Beam of Circularly Polarised Light.," *Proceedings of the Royal Society of London. Series A, Containing Papers of a Mathematical and Physical Character*, vol. 82.557, pp. 560–567, 1909.

[110] A. Einstein, "The Quantum Theory of Radiation," Tech. Rep., p. 121.

[111] H. M. Asif, A. Affan, N. Tarhuni, and K. Raahemifar, "Deep Learning-Based Next-Generation Waveform for Multiuser VLC Systems," *Sensors*, vol. 22, no. 7, Apr. 2022, ISSN: 14248220. DOI: `10.3390/s22072771`.

[112] N. Bozinovic, Y. Yue, Y. Ren, *et al.*, "Terabit-scale orbital angular momentum mode division multiplexing in fibers," *Science*, vol. 340, no. 6140, pp. 1545–1548, 2013, ISSN: 10959203. DOI: `10.1126/science.1237861`.

[113] Y. Shen, X. Wang, Z. Xie, *et al.*, *Optical vortices 30 years on: OAM manipulation from topological charge to multiple singularities*, Dec. 2019. DOI: `10.1038/s41377-019-0194-2`.

[114] A. Mair, A. Vaziri, G. Weihs, and A. Zeilinger, "Entanglement of Orbital Angular Momentum States of Photons," Tech. Rep., 2002.

[115] R. Fickler, R. Lapkiewicz, W. N. Plick, *et al.*, "Quantum Entanglement of High Angular Momenta," Tech. Rep.

[116] H. Rubinsztein-Dunlop, A. Forbes, M. V. Berry, *et al.*, "Roadmap on structured light," *Journal of Optics (United Kingdom)*, vol. 19, no. 1, Jan. 2017, ISSN: 20408986. DOI: `10.1088/2040-8978/19/1/013001`.

[117] S. W. Director, R. N. Bracewell, C. Cherry, *et al.*, "McGraw-Hill Series in Electrical and Computer Engineering SENIOR CONSULTING EDITOR Circuits and Systems Communications and Signal Processing Computer Engineering Control Theory Electromagnetics Electronics and VLSI Circuits Introductory Power and Energy Radar and Antennas PREVIOUS CONSULTING EDITORS Elec tromagnetics SENIOR CONSULTING EDITOR," Tech. Rep.

[118]   H. Kupianskyi, S. A. Horsley, and D. B. Phillips, "High-dimensional spatial mode sorting and optical circuit design using multi-plane light conversion," *APL Photonics*, vol. 8, no. 2, Feb. 2023, ISSN: 23780967. DOI: `10.1063/5.0128431`.

[119]   W. P. Bleha and L. A. Lei, "Advances in Liquid Crystal on Silicon (LCOS) spatial light modulator technology," in *Display Technologies and Applications for Defense, Security, and Avionics VII*, vol. 8736, SPIE, Jun. 2013, 87360A, ISBN: 9780819495273. DOI: `10.1117/12.2015973`.

[120]   A. Othonos, K. Kalli, D. Pureur, and A. Mugnier, "Fibre Bragg gratings," *Springer Series in Optical Sciences*, vol. 123, pp. 189–269, 2006, ISSN: 03424111. DOI: `10.1007/3-540-31770-8{\_}6`.

[121]   K. O. Hill and G. Meltz, "Fiber Bragg Grating Technology Fundamentals and Overview," Tech. Rep. 8, 1997, p. 1263.

[122]   A. D. Kersey, M. A. Davis, H. J. Patrick, *et al.*, "Fiber Grating Sensors," Tech. Rep. 8, 1997.

[123]   Y. Shen, H. Sun, D. Peng, *et al.*, "Optical image reconstruction in 4f imaging system: Role of spatial coherence structure engineering," *Applied Physics Letters*, vol. 118, no. 18, May 2021, ISSN: 00036951. DOI: `10.1063/5.0046288`.

[124]   G. A. López-Muñoz, A. Cortés-Reséndiz, J. Ramón-Azcón, and A. Rydosz, "Scalable, Lithography-Free Plasmonic Metasurfaces by Nano-Patterned/Sculpted Thin Films for Biosensing," *Frontiers in Sensors*, vol. 3, Jun. 2022. DOI: `10.3389/fsens.2022.945525`.

[125]   G. T. Carroll, N. J. Turro, A. Mammana, and J. T. Koberstein, "Photochemical Immobilization of Polymers on a Surface: Controlling Film Thickness and Wettability," *Photochemistry and Photobiology*, vol. 93, no. 5, pp. 1165–1169, Oct. 2017, ISSN: 17511097. DOI: `10.1111/php.12751`.

[126] L. A. Giannuzzi and F. A. Stevie, "A review of focused ion beam milling techniques for TEM specimen preparation," Tech. Rep. [Online]. Available: `www.elsevier.com/locate/micron`.

[127] J. O. Carlsson and P. M. Martin, "Chemical Vapor Deposition," in *Handbook of Deposition Technologies for Films and Coatings: Science, Applications and Technology*, Elsevier, Nov. 2009, pp. 314–363, ISBN: 9780815520313. DOI: `10.1016/B978-0-8155-2031-3.00007-7`.

[128] D. Pochan and O. Scherman, *Introduction: Molecular Self-Assembly*, Nov. 2021. DOI: `10.1021/acs.chemrev.1c00884`.

[129] J. J. Richardson, J. Cui, M. Björnmalm, J. A. Braunger, H. Ejima, and F. Caruso, *Innovation in Layer-by-Layer Assembly*, Dec. 2016. DOI: `10.1021/acs.chemrev.6b00627`.

[130] W. A. Murray and W. L. Barnes, *Plasmonic materials*, Nov. 2007. DOI: `10.1002/adma.200700678`.

[131] M. Huff, "Recent advances in reactive ion etching and applications of high-aspect-ratio microfabrication," *Micromachines*, vol. 12, no. 8, Aug. 2021, ISSN: 2072666X. DOI: `10.3390/mi12080991`.

[132] M. Ohring, *Thin-Film Evaporation Processes*. DOI: `https://doi.org/10.1016/B978-0-12-524975-1.X5000-9`.

[133] J. R. Roth, *Industrial plasma engineering*, ISBN: 0750303174.

[134] K. R. Williams, K. Gupta, and M. Wasilik, "Etch rates for micromachining processing - Part II," *Journal of Microelectromechanical Systems*, vol. 12, no. 6, pp. 761–778, Dec. 2003, ISSN: 10577157. DOI: `10.1109/JMEMS.2003.820936`.

[135] E. Sharma, R. Rathi, J. Misharwal, *et al.*, *Evolution in Lithography Techniques: Microlithography to Nanolithography*, Aug. 2022. DOI: `10.3390/nano12162754`.

[136] N. Unno and T. Mäkelä, *Thermal Nanoimprint Lithography—A Review of the Process, Mold Fabrication, and Material*, Jul. 2023. DOI: `10.3390/nano13142031`.

[137] A. L. Samuel, "Some Studies in Machine Learning Using the Game of Checkers," Tech. Rep.

[138] I. Goodfellow, Y. Bengio, and A. Courville, "Deep Learning," Tech. Rep.

[139] M. Jordan, J. Kleinberg, and B. Schölkopf, "Information Science and Statistics," Tech. Rep.

[140] Y. Lecun, Y. Bengio, and G. Hinton, *Deep learning*, May 2015. DOI: `10.1038/nature14539`.

[141] K. P. Murphy, *Machine learning : a probabilistic perspective*, p. 1067, ISBN: 9780262018029.

[142] E. Alpaydin, *Introduction to Machine Learning*, 3th edition, The MIT Press, Ed. The MIT Press, 2020.

[143] V. N. Vapnik, *The nature of statistical learning theory*, 2nd edition, Springer, Ed. Berkeley: Springer, 1999, pp. -334.

[144] C. Cortes, V. Vapnik, and L. Saitta, "Support-Vector Networks Editor," Tech. Rep., 1995, pp. 273–297.

[145] B. Schölkopf and A. J. Smola, *Learning with Kernels: Support Vector Machines, Regularization, Optimization, and Beyond*. The MIT Press, Jun. 2018, ISBN: 9780262256933. DOI: `10.7551/mitpress/4175.001.0001`. [Online]. Available: `https://doi.org/10.7551/mitpress/4175.001.0001`.

[146] Cristianini, Nello, and J. Shawe-Taylor, "An introduction to support vector machines and other kernel-based learning methods. Repr," *Introduction to Support*

Vector Machines and other Kernel-Based Learning Methods, vol. 22, Jun. 2001. DOI: `10.1017/CBO9780511801389`.

[147] T. Neubert and M. Vergöhl, "Organic optical coatings," in *Optical Thin Films and Coatings: From Materials to Applications*, Elsevier, Jan. 2018, pp. 425–447, ISBN: 9780081020739. DOI: `10.1016/B978-0-08-102073-9.00010-2`.

[148] A. Rothen, "The ellipsometer, an apparatus to measure thicknesses of thin surface films," *Review of Scientific Instruments*, vol. 16, no. 2, pp. 26–30, 1945, ISSN: 00346748. DOI: `10.1063/1.1770315`.

[149] H. Yang, A. Jin, Q. Luo, J. Li, C. Gu, and Z. Cui, "Electron beam lithography of HSQ/PMMA bilayer resists for negative tone lift-off process," *Microelectronic Engineering*, vol. 85, pp. 814–817, Jun. 2008. DOI: `10.1016/j.mee.2008.01.006`.

[150] Y. Chen, "Nanofabrication by electron beam lithography and its applications: A review," *Microelectronic Engineering*, vol. 135, pp. 57–72, 2015, ISSN: 0167-9317. DOI: `https://doi.org/10.1016/j.mee.2015.02.042`. [Online]. Available: `https://www.sciencedirect.com/science/article/pii/S016793171500101X`.

[151] C. C. Yang and W. C. Chen, "The structures and properties of hydrogen silsesquioxane (hsq) films produced by thermal curing," *Journal of Materials Chemistry*, vol. 12, no. 4, pp. 1138–1141, 2002, ISSN: 09599428. DOI: `10.1039/b107697n`.

[152] B. W. Chen, Y. C. He, S. Y. Sung, *et al.*, "Synthesis and characterization of magnetic nanoparticles coated with polystyrene sulfonic acid for biomedical applications," *Science and Technology of Advanced Materials*, vol. 21, no. 1, pp. 471–481, Jan. 2020, ISSN: 18785514. DOI: `10.1080/14686996.2020.1790032`.

[153] T. Tevi, S. W. Saint Birch, S. W. Thomas, and A. Takshi, "Effect of Triton X-100 on the double layer capacitance and conductivity of poly(3,4-ethylenedioxythiophene):poly(styrenesulfo

(PEDOT:PSS) films," *Synthetic Metals*, vol. 191, pp. 59–65, 2014, ISSN: 0379-6779. DOI: `https://doi.org/10.1016/j.synthmet.2014.02.005`. [Online]. Available: `https://www.sciencedirect.com/science/article/pii/S0379677914000423`.

[154] A. E. Grigorescu and C. W. Hagen, *ZResists for sub-20-nm electron beam lithography with a focus on HSQ: State of the art*, 2009. DOI: `10.1088/0957-4484/20/29/292001`.

[155] M. Altissimo, "E-beam lithography for micro-/nanofabrication," *Biomicrofluidics*, vol. 4, no. 2, 2010, ISSN: 19321058. DOI: `10.1063/1.3437589`.

[156] Z. Cui, *Nanofabrication: Principles, Capabilities and Limits: Second Edition*. Springer International Publishing, Jan. 2017, pp. 1–432, ISBN: 9783319393612. DOI: `10.1007/978-3-319-39361-2`.

[157] A. Trichili, K. H. Park, M. Zghal, B. S. Ooi, and M. S. Alouini, "Communicating Using Spatial Mode Multiplexing: Potentials, Challenges, and Perspectives," *IEEE Communications Surveys and Tutorials*, vol. 21, no. 4, pp. 3175–3203, Oct. 2019, ISSN: 1553877X. DOI: `10.1109/COMST.2019.2915981`.

[158] L. Li, H. Zhao, C. Liu, L. Li, and T. J. Cui, *Intelligent metasurfaces: control, communication and computing*, Dec. 2022. DOI: `10.1186/s43593-022-00013-3`.

[159] Y. Lee, S. J. Kim, H. Park, and B. Lee, *Metamaterials and metasurfaces for sensor applications*, Aug. 2017. DOI: `10.3390/s17081726`.

[160] Z. Zhang, H. Shi, L. Wang, *et al.*, *Recent Advances in Reconfigurable Metasurfaces: Principle and Applications*, Feb. 2023. DOI: `10.3390/nano13030534`.

[161] N. K. Fontaine, R. Ryf, H. Chen, D. T. Neilson, K. Kim, and J. Carpenter, "Laguerre-Gaussian mode sorter," *Nature Communications*, vol. 10, no. 1, Dec. 2019, ISSN: 20411723. DOI: `10.1038/s41467-019-09840-4`.

[162] J. Carpenter, B. J. Eggleton, and J. Schröder, "Complete spatiotemporal characterization and optical transfer matrix inversion of a 420 mode fiber," *Opt. Lett.*, vol. 41, no. 23, pp. 5580–5583, Dec. 2016. DOI: `10.1364/OL.41.005580`. [Online]. Available: `https://opg.optica.org/ol/abstract.cfm?URI=ol-41-23-5580`.

[163] R. Ryf, N. K. Fontaine, H. Chen, *et al.*, "Mode-multiplexed transmission over conventional graded-index multimode fibers," *Opt. Express*, vol. 23, no. 1, pp. 235–246, Jan. 2015. DOI: `10.1364/OE.23.000235`. [Online]. Available: `https://opg.optica.org/oe/abstract.cfm?URI=oe-23-1-235`.

[164] H. Huang, G. Milione, M. P. Lavery, *et al.*, "Mode division multiplexing using an orbital angular momentum mode sorter and MIMO-DSP over a graded-index few-mode optical fibre," *Scientific Reports*, vol. 5, Oct. 2015, ISSN: 20452322. DOI: `10.1038/srep14931`.

[165] J. Carpenter, B. J. Eggleton, and J. Schröder, "Observation of Eisenbud-Wigner-Smith states as principal modes in multimode fibre," *Nature Photonics*, vol. 9, no. 11, pp. 751–757, Oct. 2015, ISSN: 17494893. DOI: `10.1038/nphoton.2015.188`.

[166] D. Stellinga, D. B. Phillips, S. P. Mekhail, *et al.*, "Time-of-flight 3D imaging through multimode optical fibers," *Science*, vol. 374, no. 6573, pp. 1395–1399, 2021. DOI: `10.1126/science.abl3771`. [Online]. Available: `https://www.science.org/doi/abs/10.1126/science.abl3771`.

[167] P. Caramazza, O. Moran, R. Murray-Smith, and D. Faccio, "Transmission of natural scene images through a multimode fibre," *Nature Communications*, vol. 10, no. 1, Dec. 2019, ISSN: 20411723. DOI: `10.1038/s41467-019-10057-8`.

[168] T. Čižmár and K. Dholakia, "Exploiting multimode waveguides for pure fibre-based imaging," *Nature Communications*, vol. 3, 2012, ISSN: 20411723. DOI: `10.1038/ncomms2024`.

[169]   A. P. Mosk, A. Lagendijk, G. Lerosey, and M. Fink, *Controlling waves in space and time for imaging and focusing in complex media*, May 2012. DOI: `10.1038/nphoton.2012.88`.

[170]   S. Leedumrongwatthanakun, L. Innocenti, H. Defienne, *et al.*, *Programmable linear quantum networks with a multimode fibre*, Mar. 2020. DOI: `10.1038/s41566-019-0553-9`.

[171]   S. Kumar, R. Singh, Z. Wang, *et al.*, "(Invited) Advances in 2D nanomaterials-assisted plasmonics optical fiber sensors for biomolecules detection," *Results in Optics*, vol. 10, Feb. 2023, ISSN: 26669501. DOI: `10.1016/j.rio.2022.100342`.

[172]   K. T. V. Grattan and T. Sun, "Fiber optic sensor technology: an overview," Tech. Rep., 2000, pp. 40–61. [Online]. Available: `www.elsevier.nlrlocatersna`.

[173]   I. Ashry, Y. Mao, A. Trichili, *et al.*, *A review of using few-mode fibers for optical sensing*, 2020. DOI: `10.1109/ACCESS.2020.3027965`.

[174]   N. Park, J. Lee, J. Park, *et al.*, "Coded optical time domain reflectometry: principle and applications," in *Passive Components and Fiber-based Devices IV*, vol. 6781, SPIE, Nov. 2007, p. 678 129, ISBN: 9780819469441. DOI: `10.1117/12.746977`.

[175]   X. Bao and Y. Wang, "Recent Advancements in Rayleigh Scattering-Based Distributed Fiber Sensors," *Advanced Devices & Instrumentation*, vol. 2021, Jan. 2021. DOI: `10.34133/2021/8696571`.

[176]   G. Hegde, B. Himakar, S. Rao, and Y.-J. Rao, "Measurement Science and Technology You may also like Simultaneous measurement of pressure and temperature in a supersonic ejector using FBG sensors In-fibre Bragg grating sensors," Tech. Rep., 1997, pp. 355–375.

[177]   G. M. H. Flockhart, W. N. MacPherson, J. S. Barton, J. D. C. Jones, L. Zhang, and I. Bennion, "Two-axis bend measurement with Bragg gratings in multicore optical fiber," *Opt. Lett.*, vol. 28, no. 6, pp. 387–389, Mar. 2003. DOI: `10.1364/OL.28.000387`. [Online]. Available: `https://opg.optica.org/ol/abstract.cfm?URI=ol-28-6-387`.

[178]   X. Chen, C. Zhang, D. J. Webb, K. Kalli, and G. D. Peng, "Highly sensitive bend sensor based on bragg grating in eccentric core polymer fiber," *IEEE Photonics Technology Letters*, vol. 22, no. 11, pp. 850–852, 2010, ISSN: 10411135. DOI: `10.1109/LPT.2010.2046482`.

[179]   M. Mazur, D. Wallberg, L. Dallachiesa, *et al.*, "Field Trial of FPGA-Based Real-Time Sensing Transceiver over 524 km of Live Aerial Fiber," Tech. Rep., 2023.

[180]   S. Colburn, Y. Chu, E. Shilzerman, and A. Majumdar, "Optical frontend for a convolutional neural network," *Appl. Opt.*, vol. 58, no. 12, pp. 3179–3186, Apr. 2019. DOI: `10.1364/AO.58.003179`. [Online]. Available: `https://opg.optica.org/ao/abstract.cfm?URI=ao-58-12-3179`.

[181]   F. Léonard, A. S. Backer, E. J. Fuller, C. Teeter, and C. M. Vineyard, "Co-Design of Free-Space Metasurface Optical Neuromorphic Classifiers for High Performance," *ACS Photonics*, vol. 8, no. 7, pp. 2103–2111, Jul. 2021, ISSN: 23304022. DOI: `10.1021/acsphotonics.1c00526`.

[182]   D. Psaltis, D. Brady, X.-G. Gu, and S. Lin, "Holography in artificial neural networks," Tech. Rep., 1990.

[183]   G. Wetzstein, A. Ozcan, S. Gigan, *et al.*, *Inference in artificial intelligence with deep optics and photonics*, Dec. 2020. DOI: `10.1038/s41586-020-2973-6`.

[184]   M. Megens, M. D. Leistikow, A. van Dusschoten, *et al.*, "Shape accuracy of fiber optic sensing for medical devices characterized in bench experiments," *Medical*

Physics, vol. 48, no. 7, pp. 3936–3947, Jul. 2021, ISSN: 24734209. DOI: `10.1002/mp.14881`.

[185] G. Gibson, J. Courtial, M. J. Padgett, *et al.*, "Free-space information transfer using light beams carrying orbital angular momentum," Tech. Rep., 2003.

[186] M. P. Lavery, G. C. Berkhout, J. Courtial, and M. J. Padgett, "Measurement of the light orbital angular momentum spectrum using an optical geometric transformation," *Journal of Optics*, vol. 13, no. 6, 2011, ISSN: 20408986. DOI: `10.1088/2040-8978/13/6/064006`.

[187] M. P. Lavery, "Vortex instability in turbulent free-space propagation," *New Journal of Physics*, vol. 20, no. 4, Apr. 2018, ISSN: 13672630. DOI: `10.1088/1367-2630/aaae9e`.

[188] W. Li, Y. Li, and K. W. Shah, *A materials perspective on radiative cooling structures for buildings*, Sep. 2020. DOI: `10.1016/j.solener.2020.06.095`.

[189] Cailabs, *https://www.cailabs.com/*.

Appendix
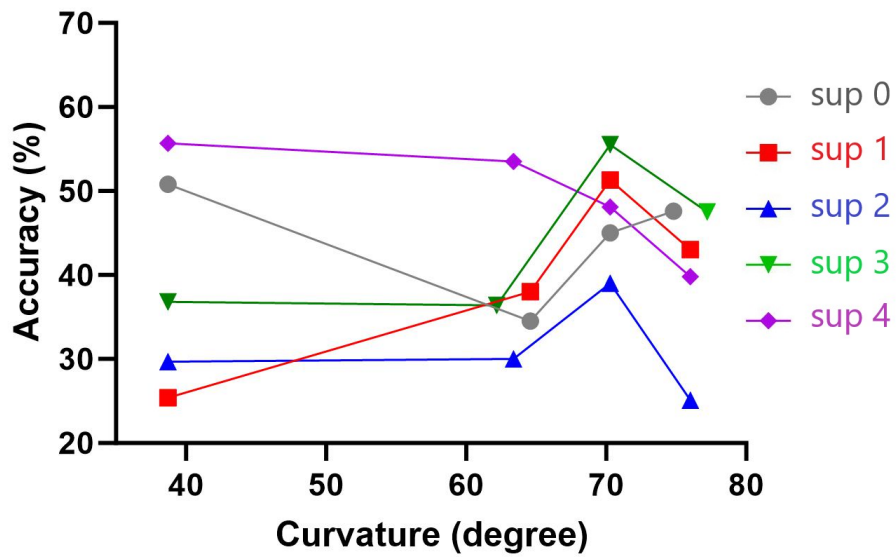
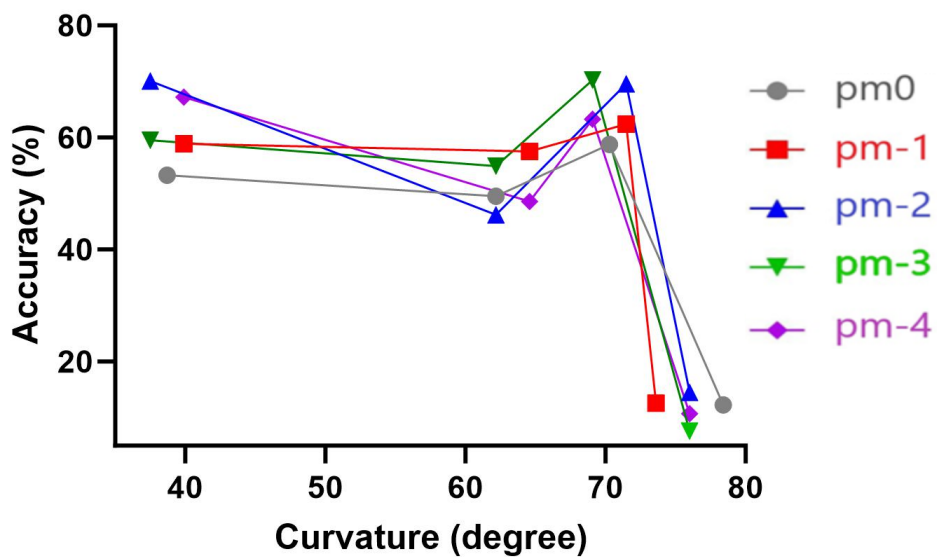Figure 7.1: Results of the experiment analysed with the algorithm "Decision tree" for the 1 m multi-mode fibre superposition.

Figure 7.2: Results of the experiment analysed with the algorithm "Decision tree" for the 1 m multi-mode fibre pure mode.
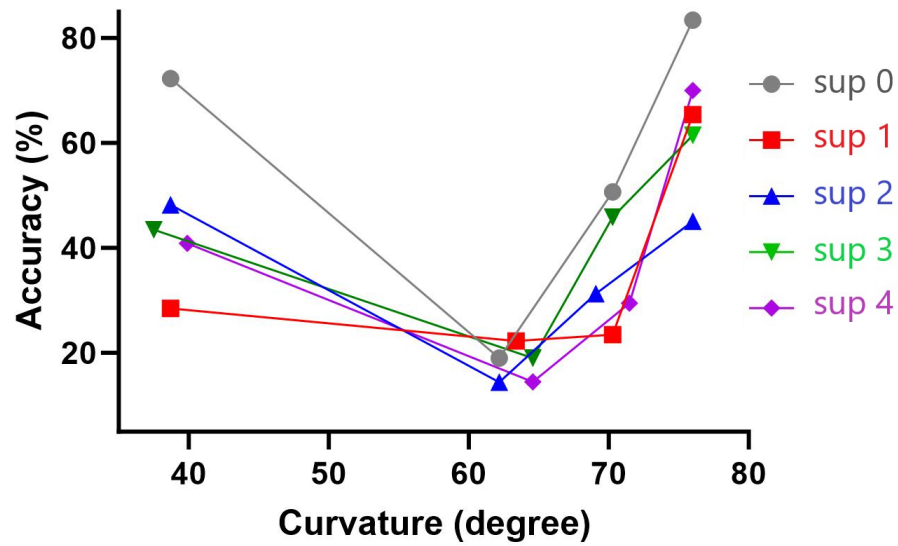
Decision tree few-mode fiber superposition
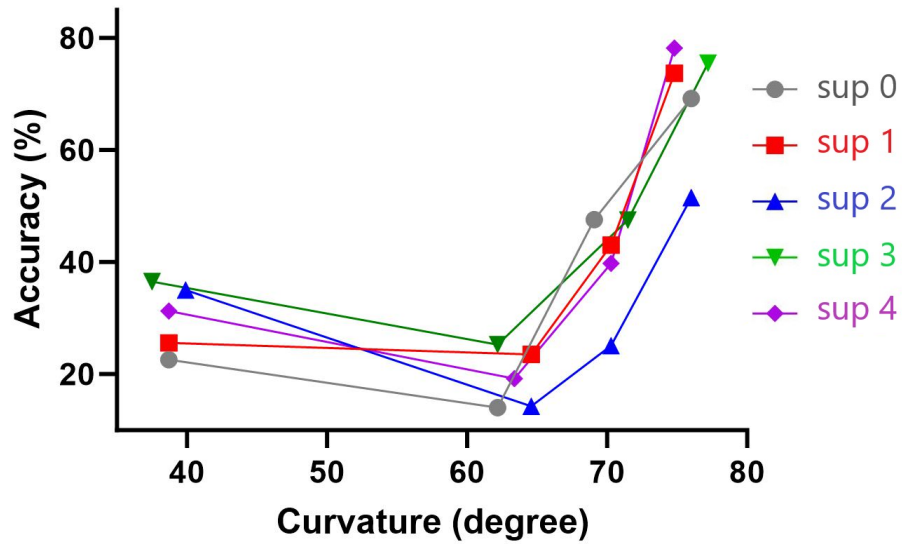
Figure 7.3: Results of the experiment analysed with the algorithm "Decision tree" for the 1 m few-mode fibre superposition.

Decision tree few-mode fiber pure mode
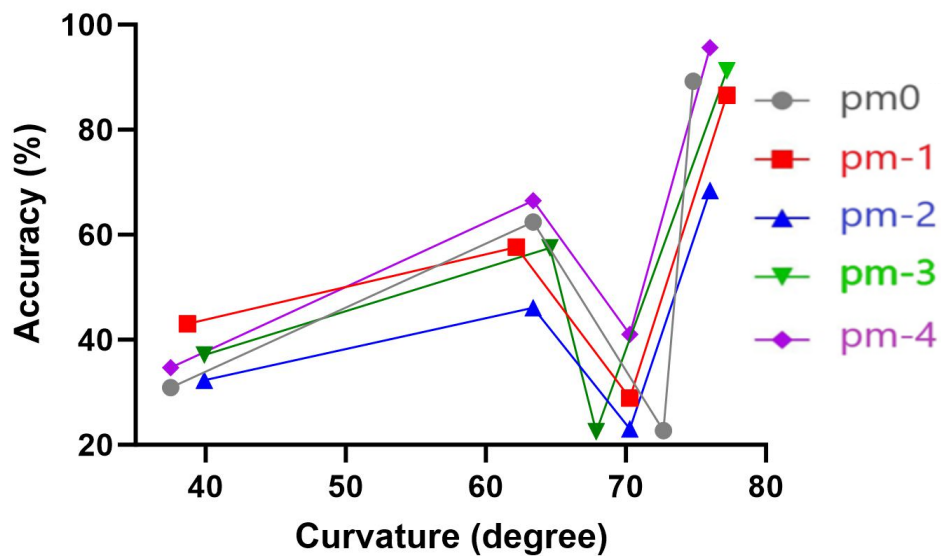
Figure 7.4: Results of the experiment analysed with the algorithm "Decision tree" for the 1 m few-mode fibre pure mode.

Figure 7.5: Results of the experiment analysed with the algorithm "Logistic regression" for the 1 m multi-mode fibre superposition.

Figure 7.6: Results of the experiment analysed with the algorithm "Logistic regression" for the 1 m multi-mode fibre pure mode.

Logistic regresion few-mode fiber superposition

Figure 7.7: Results of the experiment analysed with the algorithm "Logistic regression" for the 1 m few-mode fibre superposition.

Logistic regresion few-mode fiber pure mode
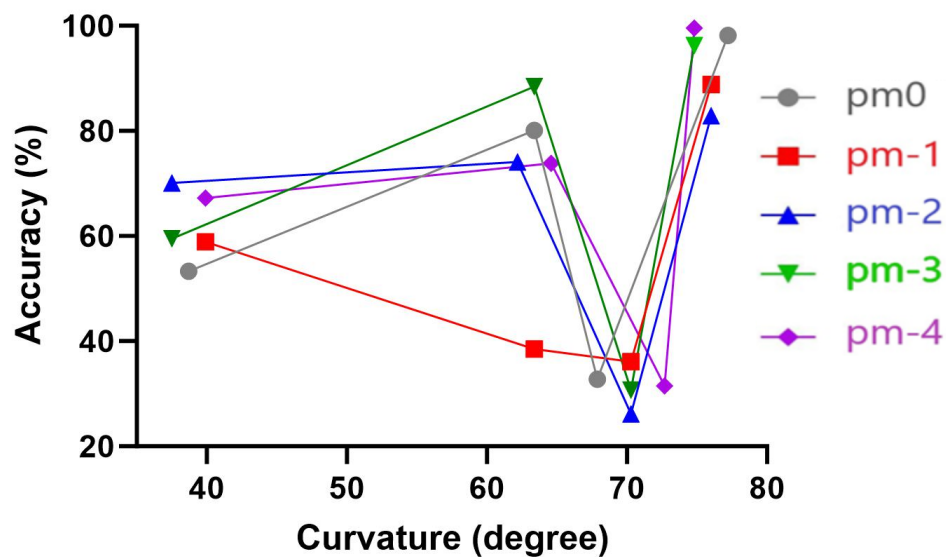
Figure 7.8: Results of the experiment analysed with the algorithm "Logistic regression" for the 1 m few-mode fibre pure mode.

Naive bayes multi-mode fiber superposition
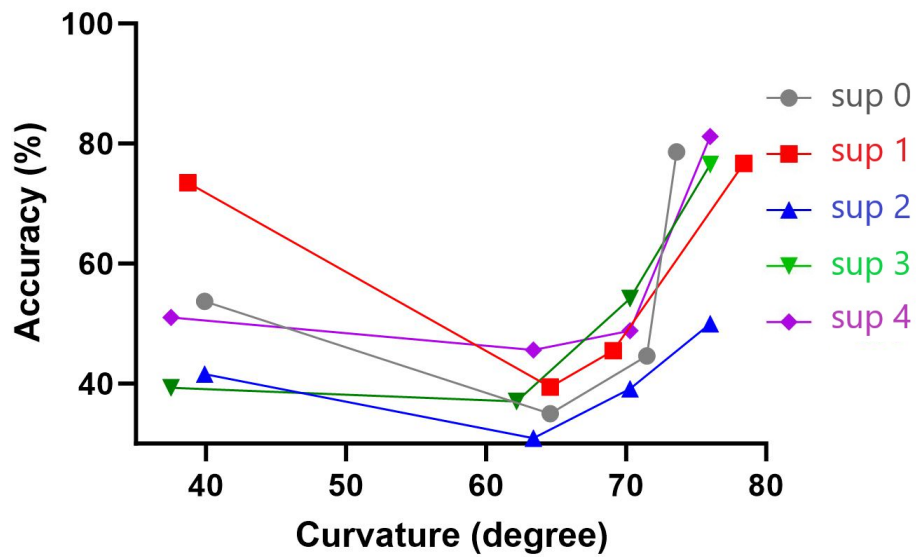
Figure 7.9: Results of the experiment analysed with the algorithm "Naive bayes" for the 1 m multi-mode fibre superposition.
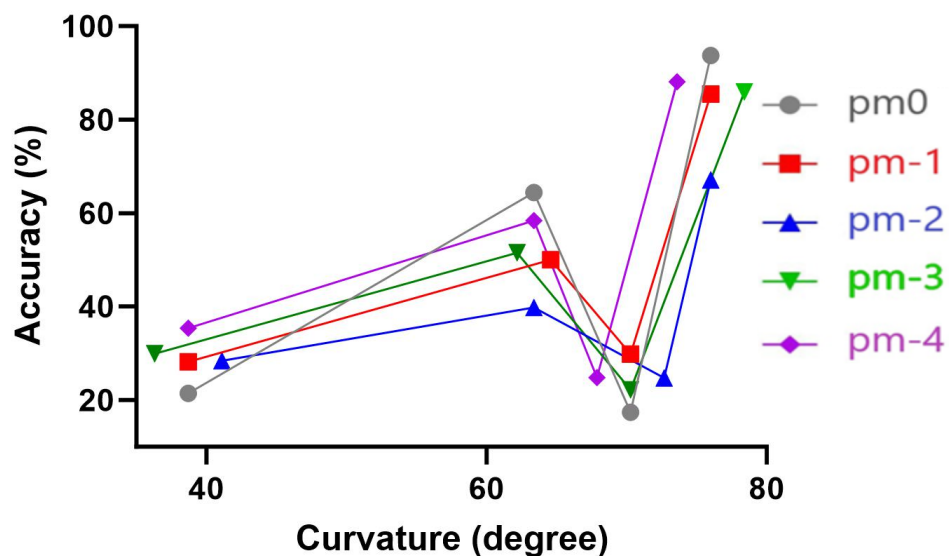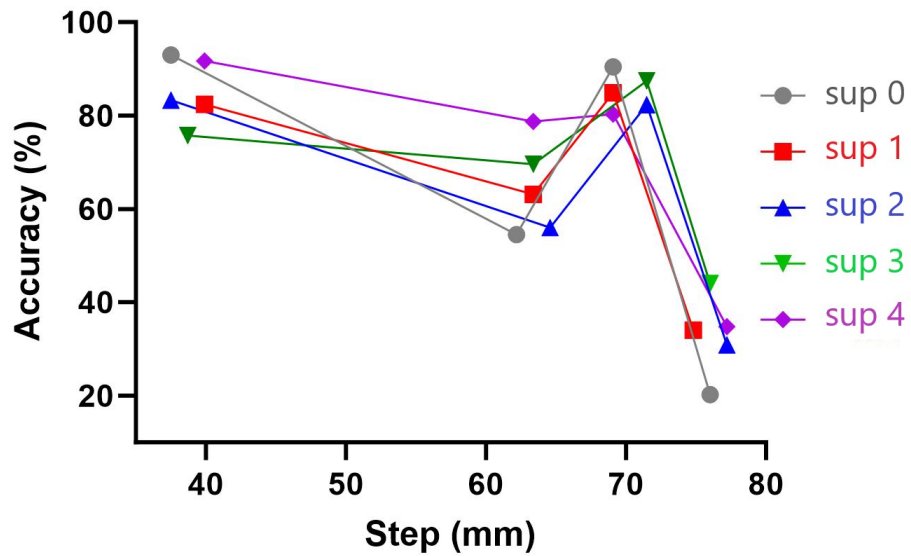
Naive bayes multi-mode fiber pure mode
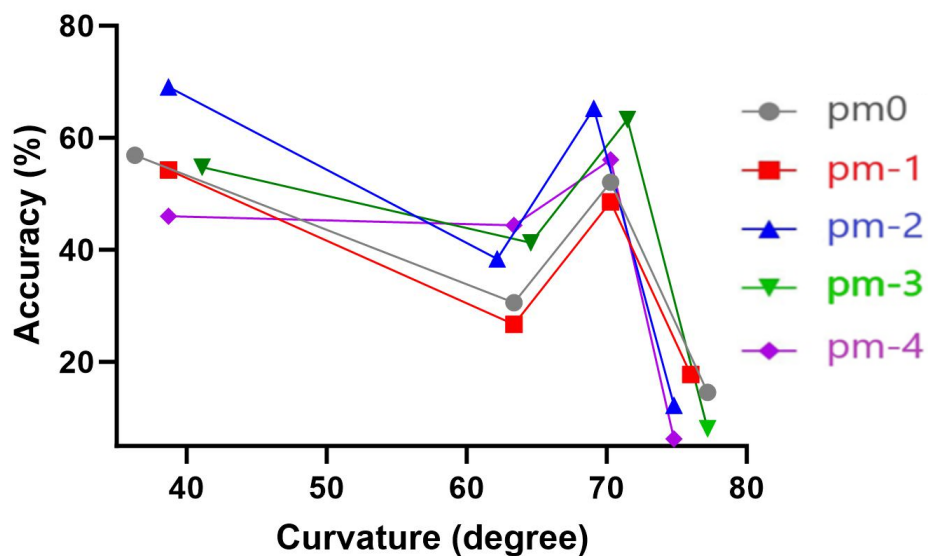
Figure 7.10: Results of the experiment analysed with the algorithm "Naive bayes" for the 1 m multi-mode fibre pure mode.

Naive bayes few-mode fiber superposition
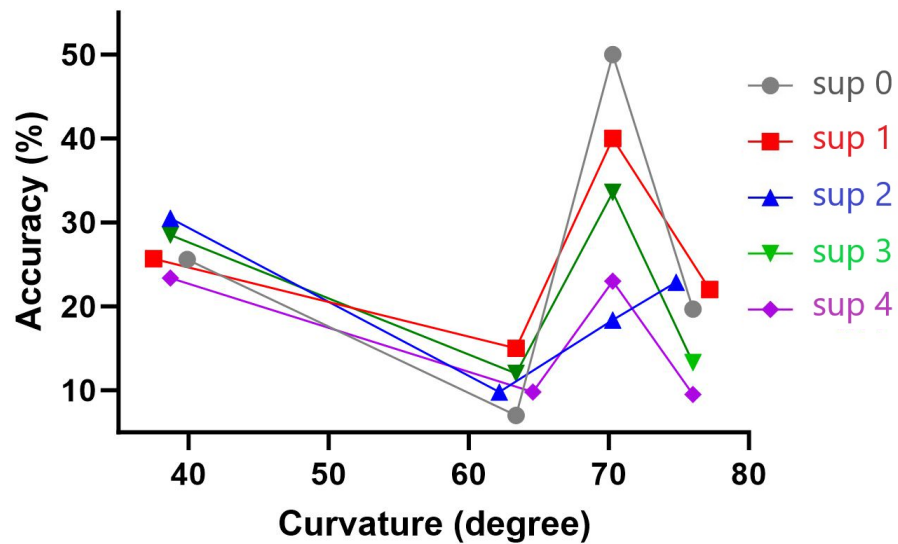
Figure 7.11: Results of the experiment analysed with the algorithm "Naive bayes" for the 1 m few-mode fibre superposition.

Naive bayes few-mode fiber pure mode

Figure 7.12: Results of the experiment analysed with the algorithm "Naive bayes" for the 1 m few-mode fibre pure mode.

Figure 7.13: Results of the experiment analysed with the algorithm "Nearest neighbors" for the 1 m multi-mode fibre superposition.

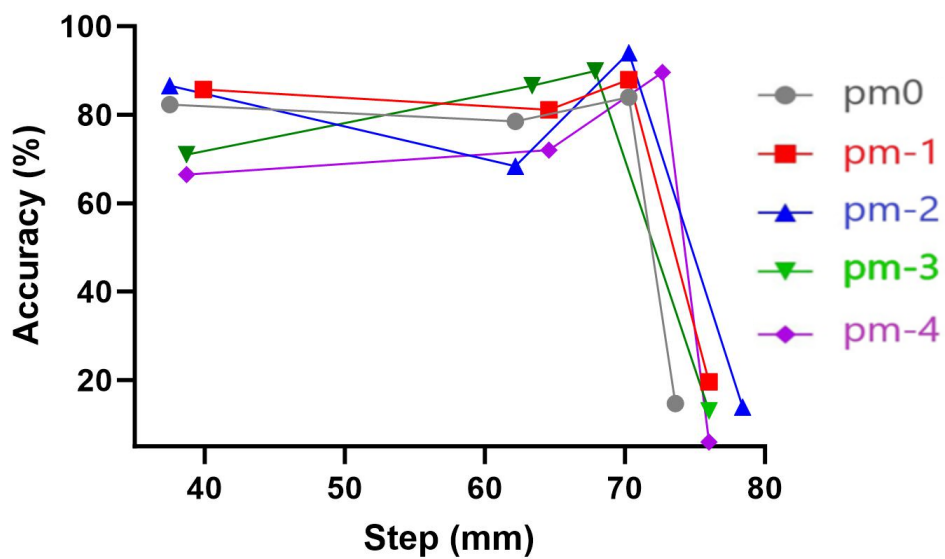Figure 7.14: Results of the experiment analysed with the algorithm "Nearest neighbors" for the 1 m multi-mode fibre pure.
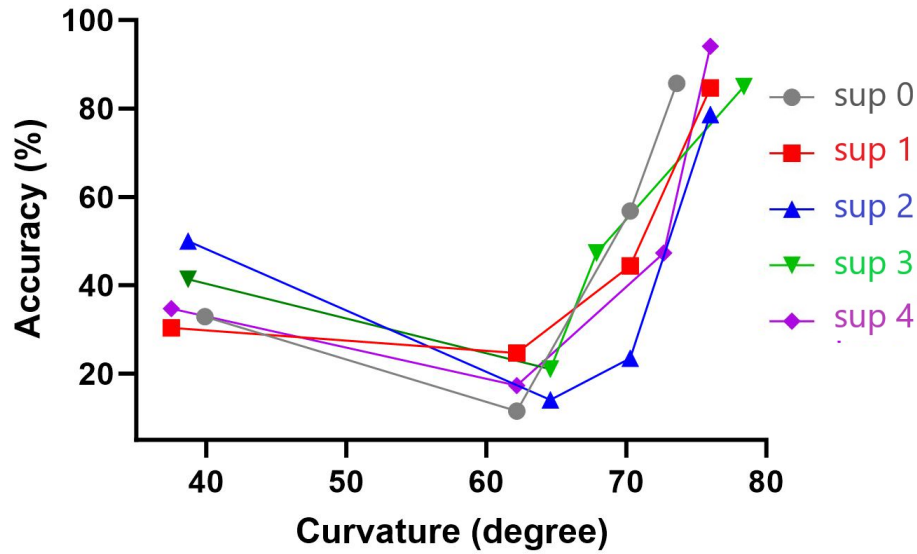
Nearest neighbour few-mode fiber superposition

Figure 7.15: Results of the experiment analysed with the algorithm "Nearest neighbors" for the 1 m few-mode fibre superposition.

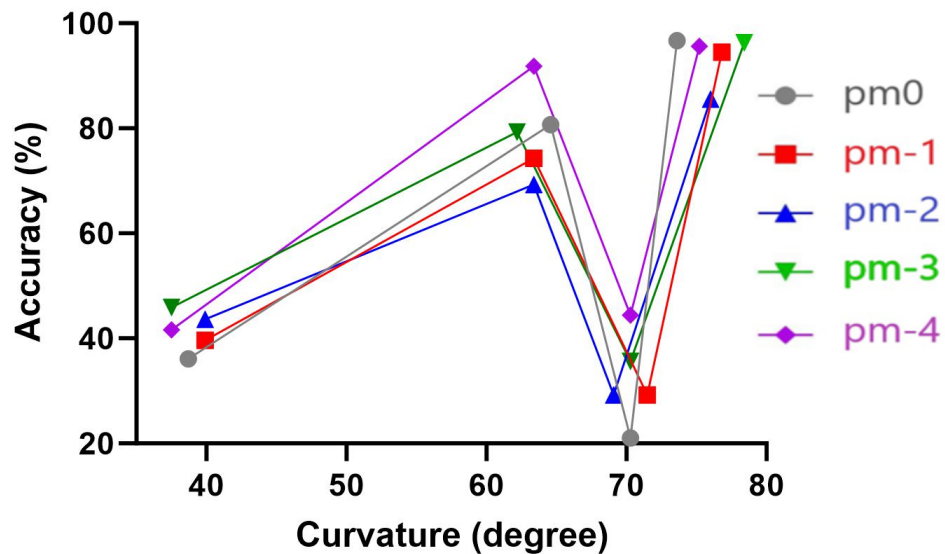**Nearest neighbour few-mode fiber pure mode**

Figure 7.16: Results of the experiment analysed with the algorithm "Nearest neighbors" for the 1 m few-mode fibre pure mode.